Construction of a 390 mK–14 T scanning tunnelling microscope used for investigations of the random Rashba effect at the nanometre scale

Von der Fakultät für Mathematik, Informatik und Naturwissenschaften der RWTH Aachen University zur Erlangung des akademischen Grades eines Doktors der Naturwissenschaften genehmigte Dissertation

vorgelegt von

Diplom-Physiker

Jan Raphael Bindel

aus Iserlohn

Berichter: Univ.-Prof. Dr. Markus Morgenstern
apl. Prof. Dr. Thomas Schäpers

Tag der mündlichen Prüfung: 20. Dezember 2016

Abstract

This thesis describes the design and performance of a newly developed low-temperature ultra-high-vacuum scanning tunnelling microscope (LT-UHV-STM) system operating at $T = 390\,\mathrm{mK}$ and magnetic fields up to 14 T. The system's performance is evaluated and compared with that of existing systems. Its outstanding mechanical stability $\delta_z = 0.7\,\mathrm{pm}$ at a bandwidth of 700 Hz is presented using a method that allows for comparison with other systems. Atomic resolution for stabilisation currents down to $I_{\mathrm{stab}} = 0.5\,\mathrm{pA}$ and for magnetic fields up to $B = 14\,\mathrm{T}$ is achieved. An electron temperature of $T_{\mathrm{el}} = 430\,\mathrm{mK}$ at one electrode and $T_{\mathrm{el}} = 520\,\mathrm{mK}$ at the other electrode of the tunnelling junction is ascertained through evaluation of superconducting tunnelling gaps and Shubnikov-de Haas oscillation, using the system magneto-transport capabilities. The Josephson peak in a superconductor-superconductor junction is used to ascertain a bias voltage noise of the tunnelling junction of $\Delta V_{\mathrm{bias}} = 16\,\mu\mathrm{V}$ at a bandwidth of ~700 Hz. The long holding time $t_{\mathrm{hold}} = 10.5\,\mathrm{days}$ at 400 mK, the virtually infinite holding time at $T = 9\,\mathrm{K}$, the spacious optical access to tip and sample at 25 K inside the UHV-cryostat, and the attached UHV-analysis and preparation chambers with a load lock, constitute a versatile system.
In the second part of this thesis a newly developed technique is used to map the variations of the Rashba spin-orbit coupling in a Cs/p-InSb sample down to the nanometre scale, limited by the magnetic length $l_B \approx 10\,\mathrm{nm}$ at $B = 6\,\mathrm{T}$. This reveals a Rashba parameter of $\overline{\alpha_{\mathrm{R}}}(\boldsymbol{R}) = 1.2\,\mathrm{eV\AA}$, with root mean square variations of $\delta_{\alpha_{\mathrm{R}}} = 0.15\,\mathrm{eV\AA}$. We find a correlation between the Rashba parameter variations and the local potential. Using an analytical and a simple numeric model, this correlation and the Rashba fluctuations are attributed to a locally changing electric field, resulting from the randomly distributed dopants. The spin dephasing length, which is determined by the Rashba fluctuation, is estimated to be $l_{\mathrm{Spin}} = 250\,\mathrm{nm}$. These experimental findings suggest that the performance of the most advanced spin transistors is likely dominated by variations of the Rashba parameter.
Furthermore, the nodal structures of the zeroth and the first Landau level (LL_0 & LL_1) wave functions are spatially resolved within this sample system. The drift states, which probe the potential disorder, develop with increasing energy for LL_0 from a Gaussian-like distribution into a ring structure growing in diameter and for LL_1 from a ring into a growing double-ring structure.

Kurzfassung

In dieser Arbeit werden das Design und die technischen Eigenschaften einer neu entwickelten Tieftemperatur-Ultrahochvakuum-Rastertunnelmikroskopie-Anlage (LT-UHV-STM), die bei $T = 390\,\mathrm{mK}$ und Magnetfeldern bis zu 14 T betrieben werden kann, präsentiert. Das System wird charakterisiert und mit anderen existierenden Systemen verglichen. Es wird die überragende mechanische Stabilität von $\delta_z = 0.7\,\mathrm{pm}$ bei einer Bandbreite von 700 Hz mit einer Methode dargestellt, die eine Vergleichbarkeit mit anderen Systemen ermöglicht. Bei Stabilisierungsströmen von nur $I_{\mathrm{stab}} = 0.5\,\mathrm{pA}$ und bei Magnetfeldern bis zu $B = 14\,\mathrm{T}$ wird atomare Auflösung erreicht. Es wird eine Elektronentemperatur von $T_{\mathrm{el}} = 430\,\mathrm{mK}$ an der einen und $T_{\mathrm{el}} = 520\,\mathrm{mK}$ an der anderen Elektrode des Tunnelkontakts bestimmt. Hierzu werden zum einen supraleitende Bandlücken vermessen und zum anderen die Magentotransportfähigkeiten des Systems genutzt, um Shubnikov-de Hass Oszillationen auszuwerten. Der Josephson-Peak eines Supraleiter-Supraleiter-Übergangs wird genutzt um das Rauschen der Tunnelspannung innerhalb des Tunnelkontakts von $\Delta V_{\mathrm{bias}} = 16\,\mu\mathrm{V}$ bei einer Bandbreite von ~700 Hz zu bestimmen. Vielseitige Nutzungsmöglichkeiten des Systems sind durch eine lange Standzeit $t_{\mathrm{hold}} = 10.5$ Tage bei 400 mK, eine nahezu unendliche Standzeit bei $T = 9\,\mathrm{K}$, dem großzügigen optischen Zugang innerhalb des UHV-Kryostaten zu Probe und Spitze bei 25 K, sowie der angeschlossenen UHV-Analyse- und Präparationskammer mit Schleuse gegeben.
Mit Hilfe dieses Systems werden die Variationen der Rashba Spin-Bahn-Wechselwirkung in einer Cs/p-InSb-Probe nanometergenau kartographiert, wobei die Limitation die magnetische Länge $l_B \approx 10\,\mathrm{nm}$ bei $B = 6\,\mathrm{T}$ ist. Es zeigt sich ein Rashba-Parameter von $\overline{\alpha_{\mathrm{R}}}(\boldsymbol{R}) = 1.2\,\mathrm{eV\AA}$, mit der Wurzel der mittleren quadratischen Abweichung von $\delta_{\alpha_{\mathrm{R}}} = 0.15\,\mathrm{eV\AA}$, wobei wir eine Korrelation zwischen Rashba-Parameter und lokalem Potential beobachten. Mittels eines analytischen Modells werden die Korrelation sowie die Variationen durch Veränderungen im elektrischen Feld, bedingt durch die Zufallsverteilung der Dotierung, erklärt. Für dieses Probensystem wird eine Länge der Spindephasierung, verursacht durch die Rashba-Fluktuationen, von $l_{\mathrm{Spin}} = 250\,\mathrm{nm}$ abgeschätzt.
Das Probensystem wird des Weiteren dafür genutzt, um die Knotenstruktur der Wellenfunktion des nullten und des ersten Landau-Niveaus (LL_0 & LL_1) räum-

lich aufzulösen. Die Driftzustände, die der Potentialunordnung folgen, entwickeln sich mit steigender Energie für LL_0 von einer gaußförmigen Verteilung in eine Ringstruktur (kein Knoten) und für LL_1 von einer Ringstruktur in eine wachsende Doppelringstruktur (ein Knoten).

Contents

1. Introduction

Electronics are undeniably an important part of our everyday lives. Conventional electronic devices are based on the transport of electronic charge, at the same time the electron spin remains unused. Devices that use the spin to transport information exhibit several advantages. Less energy is needed to flip the spin of an electron towards the charge transport through a device. Likewise, the time to switch between a spin-up and spin-down state is not limited to the charge transport. Such devices utilising the spin are called spintronics, which has existed as a research field of solid-state physics for about 20 years. It is based on many well investigated physical principles and phenomena, e.g. the quantum Hall effect, superconductivity or transistor electronics [1, 2]. The spintronics device MRAM, as a non-volatile memory, is already in application. Other functional devices are the spin field-effect transistors [3, 4], spin filters [5] and quantum bits. The possibility of entangling spin states makes spintronics also a promising approach for the realisation of quantum computing. It has proved difficult to create feasible devices that allow a controlled spin manipulation and this challenge is a topic of present research [6, 7, 8, 9, 10, 11]. Many promising approaches for the realisation of spin field-effect transistors are using the so-called Rashba effect to tune the spin-orbit interaction. An electron spin propagating perpendicularly to an electric field exhibits, proportional to the strength of the spin-orbit interaction, an effective magnetic field. The magnetic field is perpendicular to the electron momentum $\boldsymbol{k}$ and the electric field. The electron spin precesses around the effective field, if originally not pointing in the effective field direction. Hence, in two-dimensional electron systems (2DES), the strength of the electric field can tune the spin-orbit interaction and thus, the spin precession rate. This approach appears to be practical for a controlled spin manipulation [3, 12, 13]. Unfortunately, it has not yet been possible to produce commercial spin-transistor devices, as they are restricted to low temperatures, have bad signal to noise ratios and only show one to two oscillations of spin precession. The $\boldsymbol{k}$-dependency of the Rashba effect leads to liability of the spin precession on scattering processes, thus many approaches focus on achieving ballistic transport [10]. By this, spin relaxation due to scattering mechanisms such as the D'yakonov' Perel (DP) and the Elliott-Yafet (EY) mechanism can be avoided [14, 15]. The mechanism that limits the functionality of those ballistic devices is unclear. An alternative

and more recent approach is an uncoupling of the spin precession from the varying electron propagation direction in order to suppress the DP-type spin relaxation, e.g. by one-dimensional devices [11] or forming a spin-helix [4, 8]. These devices would, however, still suffer from a fluctuating Rashba field, which would cause spin dephasing without any scattering processes [16]. In the second part of this thesis (Part II), the main focus will be on an experimental technique to probe the spatial variations in the Rashba field using scanning tunnelling microscopy (STM). 2DES structures are typically semiconductor heterostructures, burying the 2DES. To make the 2DES accessible via STM a system is used that exhibits a 2DES at its surface. Therefore, Cs is adsorbed on InSb(110), resulting in a surface 2DES. In a vanguard experiment, the Rashba parameter is determined down to the nm length scale [17].
Many effects in solid-state physics manifest in distinct patterns of the electron wave functions Ψ making it interesting to probe Ψ or $|\Psi|^2$ directly. STM can map the electronic density of states (DOS) in a 2DES or on the surface of a 3D bulk and hence $|\Psi|^2$. The corresponding $|\Psi|^2$ has been probed, e.g. in metals [18], semiconductors [19] and graphene [20]. A prominent fundamental example of $|\Psi|^2$ is the orbital motion of electrons in a strong perpendicular magnetic field. The electron motion, classically described by cyclotron orbits, leads quantum mechanically to an energy quantisation into Landau levels (LL). As yet it has not been possible to probe the nodal structure of the corresponding wave functions in real space. This work presents observations that exceed the evolution of drift states [21, 22] and clearly resolve this nodal structure (Chapter 7).
Experimental access to these fundamental principles of condensed matter physics has proved to be challenging. STM is a powerful tool for investigations down to the subatomic length scale. Besides topography, scanning tunnelling spectroscopy enables the study of the band structures or the resolution of electron interaction effects. High energy resolution is required, for instance, for LL and spin splitting ($\Delta E \approx 10\,\mathrm{meV}$), superconducting gaps ($\Delta E \lesssim 2\,\mathrm{meV}$), or Josephson tunnelling peak widths ($\Delta E \lesssim 100\,\mu\mathrm{eV}$). In addition to the need for high mechanical stability and long-time measurements, there is also a necessity for experiments to be performed at low temperatures. This, along with additional special requirements for experiments on the quantum Hall effect, e.g. high magnetic field and clean sample surfaces, necessitates the development of new systems. The first part of this thesis introduces such a home-built system. For the sake of comparison it describes the state of the art for low-temperature, ultra-high-vacuum scanning tunnelling microscope systems (LT-UHV-STM). It is shown that the built-up system operates at temperatures below 400 mK with an energy resolution of $\Delta E \approx 50\,\mu\mathrm{eV}$, extraordinary stability ($\delta_z < 1\,\mathrm{pm}$),

holding time ($t_{\text{hold}} > 10\,\text{days}$) and optical access. This system has not only enabled investigations on the spatially varying Rashba parameter but also opened up the possibility for future experiments on topological insulators, Majorana fermions [9] and Wigner crystals [23].

This thesis is separated into two parts. The first part (Part I) covers the development of the LT-UHV-STM system while the second part (Part II) covers the investigation of Cs/p-InSb regarding the variation of the Rashba effect and observations of the nodal structure of LL wave functions. Chapter 2 provides a brief introduction into scanning tunnelling microscopy and an overview of the existing LT-UHV-STM systems. In Chapter 3 the design of the home-built system is introduced, and in Chapter 4 the performance of the developed system is presented.
Chapter 5 gives a theoretical introduction into Rashba spin-orbit coupling and introduces the influence of a magnetic field and potential disorder. In Chapter 6 recent experimental studies on spintronics and spin-orbit interaction are reviewed, followed by investigation on the local variations of the spin-orbit coupling in Chapter 7 and the observations on the nodal structure LL wave functions in Chapter 7.5.

Part I.

Combined UHV-STM/AFM system operating at 390 mK and 14 T

2. Scanning tunnelling microscopy at low temperature

For nano devices and spintronics it is necessary to have control over small structures and small-scale devices down to the atomic length scale. Versatile technologies for subatomic investigation and manipulation are provided by scanning probe microscopy (SPM) techniques such as scanning tunnelling microscopy (STM), invented by Binnig and Rohrer [24], and atomic force microscopy (AFM) [25]. It is necessary to operate at low temperatures to achieve high energy resolutions, which can be limited by the thermal energy $E_\mathrm{T} = k_\mathrm{B}T$. Furthermore, the existence and observation of many effects, e.g. superconductivity, quantum Hall effect, Kondo effect, Wigner crystallisation etc., is restricted to low temperatures. Atoms and molecules with small binding energy can be adsorbed, and stable imaging is being facilitated. Beyond this, low temperatures are advantageous for preserving clean and controlled experimental conditions. Ultra high vacuum (UHV) systems achieve pressures down to $p = 10^{-11}$ mbar. Assuming that all residual particles are adsorbed when bouncing at a sample surface, attainment of a full monolayer coverage would take place after 10^5 s at room temperature. By going towards lower temperatures (LT), the residual particles are pumped by cold surfaces and the pressure in the system can be reduced by several orders of magnitude, helping to maintain a clean surface for a longer period of time.

In the first part of this thesis, the design and characterisation of a LT-UHV-SPM system is introduced, with the main usage as a scanning tunnelling microscope. The experimental investigations are covered by the second part of this thesis and mainly done using this technique. This section will cover a brief introduction into scanning tunnelling microscopy. Furthermore, an overview of existing LT-UHV-STM systems is given to allow a classification of the presented system.

2.1. STM and STS

An STM is realised by scanning an electrically conducting and atomically sharp tip across a conductive sample surface, giving the possibility to probe physical properties with subatomic resolution (see [26, 27]). When tip and sample are brought to a distance d of a few Å and a bias voltage is applied between tip and sample, a current can be measured. This current is based on the quantum mechanical tunnelling effect. For sample voltages V much smaller than the mean barrier height $\Phi_{\text{eff}} \approx (\Phi_\text{t} + \Phi_\text{s})/2$, with Φ_t and Φ_s the work function of the tip and sample, respectively (Figure 2.1(a)), the tunnelling current in the Wentzel-Kramers-Brillouin approximation is given by

$$I = \int_0^{eV} \rho_\text{t}(r,E)\rho_\text{s}(r,\pm eV \mp E)T(E,eV,r)\text{d}E, \tag{2.1}$$

with $\rho_i(r,E)$ the density of state of tip ($i = t$) and sample ($i = s$) at energy E and position r, and e the electron charge. T describes the transmission probability $T(E,eV) \approx e^{-\kappa d}$, with the decay constant

$$\kappa = \sqrt{\frac{2m_\text{e}}{\hbar^2}\left(\Phi_{\text{eff}} - \frac{|eV|}{2}\right)}, \tag{2.2}$$

with m_e the electron mass and $\hbar$ the reduced Planck constant [28]. The tunnelling probability increases exponentially with a reduction of the tunnelling barrier width d. This results in a highly distance-dependent tunnelling current

$$I \propto Ve^{-\kappa d}. \tag{2.3}$$

This one-dimensional model has been extended by Bardeen [29], and Tersoff and Hamann [30, 31] for 3D elastic tunnelling assuming s-type tunnelling orbitals of the tip. In this model the tunnelling current at low bias V between tip and sample can be written as

$$I \propto \rho_\text{s}(E_{\text{F,t}})\rho_\text{t}(E_{\text{F,s}},\boldsymbol{r}) \cdot Ve^{-\kappa(R)d}. \tag{2.4}$$

Here, $E_{\text{F,i}}$ denotes the Fermi level and the exponent $\kappa(R)$ is the decay constant of the s-orbital of the tip.
Most STMs use metallic tips, such as PtIr or tungsten. The tunnelling orbitals of such STM tips are mostly p and d orbitals. Chen [32, 33, 34] sought a better description of such tip states by calculating the changes in the transmission coefficient for different types of tunnelling orbitals, and was able to derive a general sum rule. In the derivation of the transmission coefficient the wave

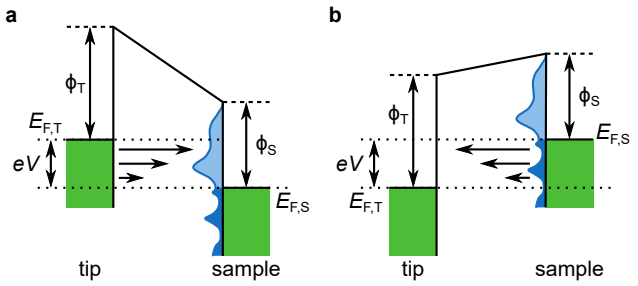

Figure 2.1.: Schematics of tunnelling between STM tip and sample – (a) Tunnelling from the tip into unoccupied sample-states (light blue) for a positive sample bias. Lengths of horizontal arrows indicate tunnelling probability. (b) Tunnelling process from occupied sample-states (dark blue) into the tip. Adapted from [28].

functions Ψ_s have to be replaced by the derivative of the wave functions. For p_i-orbitals ($i = x, y, z$) Ψ_s is replaced by $\frac{\partial \Psi_s}{\partial i}$, for most $d_{i,j}$-orbitals by $\frac{\partial^2 \Psi_s}{\partial i \partial j}$ and similarly for higher orbitals. The sharper p_x and d_{z^2} orbitals, which typically dominate the tunnelling current, lead to better lateral resolution, resulting in subatomic resolutions in STM measurements.
Access to the local density of states in an STM experiment is given by measuring the differential conductivity. A differentiation of Equation (2.1) gives

$$\begin{aligned} \left.\frac{\mathrm{d}I}{\mathrm{d}V}\right|_V \quad &\propto \quad \rho_\mathrm{s}(E_\mathrm{F}+eV)\cdot\rho_\mathrm{t}(E_\mathrm{F})\cdot T(eV,V,d) \\ &+ \quad \int_0^{eV} \rho_\mathrm{s}(E_\mathrm{F}+E)\cdot\rho_\mathrm{t}(E_\mathrm{F}+E-eV)\cdot\frac{\mathrm{d}}{\mathrm{d}V}T(E,V,d)\mathrm{d}E \\ &+ \quad \int_0^{eV} \rho_\mathrm{s}(E_\mathrm{F}+E)\cdot\frac{\mathrm{d}}{\mathrm{d}V}\rho_\mathrm{t}(E_\mathrm{F}+E-eV)\cdot T(E,V,d)\mathrm{d}E. \end{aligned} \tag{2.5}$$

The first term gives the density of states of the sample $\rho_\mathrm{s}(E_\mathrm{F}+eV)$. For small bias voltages compared to the work function, the second term becomes negligible due to small variations of the transmission coefficients. The third term is sensitive to variations of the density of states of the tip. For metallic tips, ρ_t is often assumed to be sufficiently constant and this term can also be neglected. Nevertheless, the contribution of the tip is the same for all ρ_s and can be characterised by measuring the differential conductance with the same tip and varying ρ_s. Likewise, features of a sample that appear identically with different microtips are most likely to be related to $\rho_s(E_\mathrm{F}+eV)$. Thus, the change in the differential conductivity at a given bias voltage V gives information about the change in ρ_s, resulting in

$$\frac{\mathrm{d}I}{\mathrm{d}V}(V) \propto \rho_\mathrm{s}(E_\mathrm{F}+eV) \tag{2.6}$$

for small bias voltage and $\rho_t = \text{const}$. The differential conductivity is accessible in STM experiments by stabilising the tip-sample distance at a constant current I_{stab} and bias voltage V_{stab} and then measuring the current for different sample biases. Deriving the voltage-dependent current signal gives the local density of states (LDOS) at that position.
An established method for using scanning tunnelling spectroscopy (STS) to directly map the differential conductivity is the Lock-In technique. To this end, the bias voltage is modulated with a frequency f_{mod} and a small modulation amplitude V_{mod}. Integrating over a sampling time t gives the differential conductivity $\mathrm{d}I/\mathrm{d}V$ or the LDOS, respectively. Larger modulation amplitudes of the sample bias lead to an averaging over a larger energy range of the LDOS and thus can limit the energy resolution. When using this method at various sample positions, whole maps of the LDOS can be acquired. This method is rather time consuming, limited by the integration period and lateral resolution. Such measurements of $\mathrm{d}I/\mathrm{d}V$ maps with 100×100 px can take several hours to days and thus place high demands on the STM-system regarding the lateral stability, drift between sample and tip, and maximal holding time at a fixed temperature.
Equation (2.1) describes the tunnelling process for zero temperature. For $T \neq 0$ a Fermi distribution of the electron occupation

$$f(E) = [\exp(E/k_B T) + 1]^{-1} \tag{2.7}$$

has to be considered [35, 27], adding a factor $[f_s(E+eV) - f_t(E)]$ to Equation (2.1) resulting in the tunnelling current broadened by the Fermi distribution [36]

$$\tilde{I}(V) = \int_{-\infty}^{+\infty} [f_s(E+eV) - f_t(E)]\, \rho_t(r,E)\rho_s(r, \pm eV \mp E)T(E, eV, r)\mathrm{d}E. \tag{2.8}$$

Additionally, V_{mod} in an STS experiment can reduce the energy resolution further. Measuring the differential conductance at finite temperatures with the Lock-In technique gives

$$\frac{\mathrm{d}I}{\mathrm{d}V}(V) \propto \int_{-\pi/2}^{\pi/2} \sin\alpha \cdot \tilde{I}\left(V + V_{mod} \cdot \sin\alpha\right) \mathrm{d}\alpha. \tag{2.9}$$

The achievable energy resolution in such an STS experiment can be approximated by [35]

$$\Delta E \approx \sqrt{(3.3 k_B T)^2 + (2.5 e V_{mod})^2}. \tag{2.10}$$

To achieve a high energy resolution the experiment has to be performed at low temperatures and small modulation amplitudes. Smaller modulations lead to

smaller signals and therefore increase the demands on the mechanical stability. A voltage noise on top of the signal can be treated as an additional modulation bias which contributes to the energy resolution. Any potential fluctuation at the Lock-In frequency between tip and sample leads to a reduction of the energy resolution (see Section 4.3).

2.2. STS of superconductors

A common technique for determining the energy resolution of a low-temperature STM-system is to exploit the density of states of superconductors [37, 27]. Considering a tunnelling junction consisting of an isotropic *s*-type superconductor and a normal metal (SN-junction, Figure 2.2(a)), the density of states ρ_{sc} for $T = 0$ from the Bardeen-Cooper-Schrieffer theory (BCS) is given by

$$\rho_{sc}(E) = \begin{cases} \rho_0 \cdot \frac{|E|}{\sqrt{E^2-\Delta^2}} & |E| \geq \Delta \\ 0 & |E| < \Delta, \end{cases} \tag{2.11}$$

with Δ being half the width of the superconducting gap, ρ_0 the density of states of the material in a non-superconducting state at E_F and E the distance from E_F. The first tunnelling experiments, resembling this density of state, were performed with an SN-junction separated with a thin oxide layer already in the early sixties [38, 39]. For finite temperatures, still below the critical temperature T_c, the singularity at $E = \pm\Delta$ and the slopes are smeared out. This leads to a gradual closing of the gap with increasing temperature and can be observed in STS experiments [40]. Here the SN-junction consists of a superconducting Nb tip and a Au surface (see Figure 2.2(b)). The observable gap may differ from the bulk values of the material for tips and thin layers, due to the proximity effect [41].
Substituting the normal conducting electrode for another superconductor builds an SS-junction. New types of tunnelling processes, namely multiple Andreev reflections [42, 43] and Josephson supercurrent [44], become possible. For small tunnelling currents, i.e. large sample tip distances, the conventional electron tunnelling described above occurs. Due to the superconducting gaps Δ_1 & Δ_2 of both electrodes, in STS a gap of the width $\Delta_1 + \Delta_2$ is observed. Only if the applied bias voltage V is greater than $(\Delta_1 + \Delta_2)/2$, electrons tunnel from occupied states of one electrode to unoccupied states of the other. By bringing the tip and sample closer together, so that the coupling of both superconductors is enhanced, multiple Andreev reflections are observable [45, 46] (cf. Figure 2.3(a)-(c)). The ratio of the two gaps Δ_1/Δ_2 determines which processes are allowed. In this thesis only the case $1 > \Delta_1/\Delta_2 > 0.5$ is important. Those quasi-

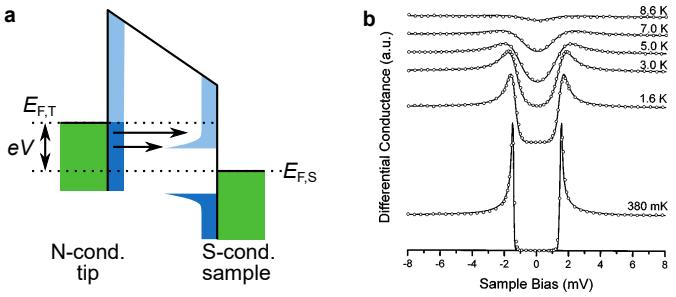

Figure 2.2.: Tunnelling between superconductor and normal conductor. – (a) Schematics of tunnelling from normal conducting tip into a superconducting sample. Dark blue: occupied states. Light blue: unoccupied states. Arrows indicate possible tunnelling. (b) Differential conductance measurement obtained by STS using a Nb tip and a Au surface taken at various temperatures. Spectra are shifted vertically for clarity. The superconducting gap is resolved at low temperatures and closes towards higher temperatures [40].

particle tunnelling events lead to peaks in STS spectra inside the gap $\Delta_1 + \Delta_2$ at $E = \Delta_1$, Δ_2 & $(\Delta_1 + \Delta_2)/3$, and for a finite DOS at $E > \Delta_1, \Delta_2$ [46]. When the Fermi energies of the two superconducting currents are aligned, strong coupling can enable Cooper pair tunnelling, and a Josephson peak appears in the spectroscopy. Usually, this analysis is performed for planar junctions, but Ivanchenko et al. [47] show that it applies down to lateral sizes of nanometre as present in the tip-sample junction. In the case of STM, for which the tip is used as an electrode, the nature of the supercurrent does not change [47]. This supercurrent has been observed in STS [48, 49] and can be locally probed in STS evolving a new field of Josephson scanning tunnelling microscopy (JSTM) [50]. For pure JSTM the Josephson coupling energy

$$E_J = \frac{\Phi_0 I_C}{2\pi} \tag{2.12}$$

has to be larger than E_T, with Φ_0 the magnetic flux quantum and I_C the critical current of the superconductor. A further influence on the Josephson current has the tunnelling capacitance charging energy $E_C = 2e^2/C$, which can exceed E_J for small tip-sample capacitances C. These perturbations lead to a fixed phase difference between the two superconductors [47]. The tunnelling Cooper pairs are bosonic quasi-particles which are condensed to a single energy. This feature is used in this thesis to estimate the bias noise in the tunnelling junction. A detailed analysis of the Josephson current in such nanoscale Josephson junctions would be too elaborate [47, 51] and will not be discussed in this thesis.

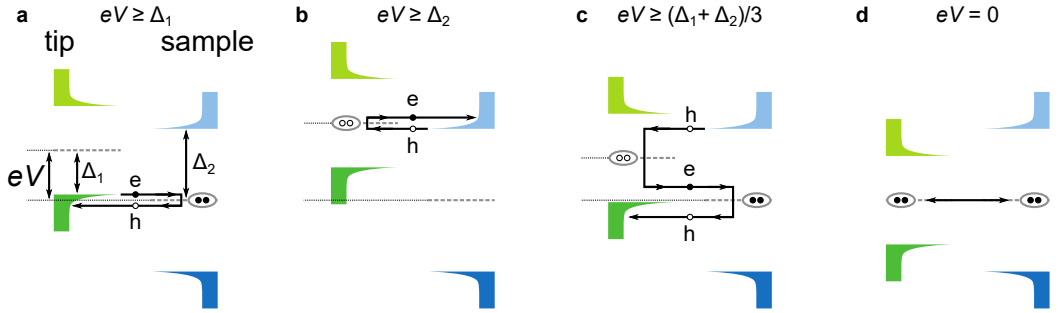

Figure 2.3.: Schematics of tunnelling processes in an asymmetric SS tunnelling junction – Multiple Andreev reflections and Josephson tunnelling processes in an SS junction for $1 > \Delta_1/\Delta_2 > 0.5$ (a) Electron tunnelling from left to the right superconductor and reflected to the left, creating a Cooper pair on the right. (b) Opposite direction of (a). Hole tunnels from right to left, annihilating a Cooper pair and reflecting an electron to the right. (c) Double reflection process as combination of the Cooper pair annihilating and creating process in (a) & (b). Adapted from [46] . (d) Josephson tunnelling. When the Fermi energies are aligned and the superconductor wave functions overlap, Cooper pairs tunnelling occurs.

2.3. Existing LT-UHV-STM systems

There are currently a number of ultra-low-temperature systems in existence, including many that are commercially available. The high performance demands in low-temperature physics and scanning probe microscopy result in many unique home-built systems, specialised to the individual needs. This section provides a benchmark of the performance by presenting an overview of existing systems with similar performances, as the system presented in this thesis, and their limitations. It illustrates the LT-UHV-STM systems that exhibit the most outstanding performances. The key aspects of the performances of the STM systems are the achievable base temperature T with the corresponding holding time t_{hold} and more crucially the actual electron temperature. For investigation of reactive sample surfaces and sample preparation, the UHV compatibility, optical access and sample transfer can be important. To benefit from a key advantage of STM, a high stability in the distance of tip and sample δ_z is pursued, while long time measurements, such as $\mathrm{d}I/\mathrm{d}V$ maps, benefit from of a small drift $V_{d_{xyz}}$ between tip and sample. Furthermore, superconducting solenoids are commonly implemented, unfolding a large research field.
While conventional L^{4}He-bath cryostats are limited to $T = 4\,\mathrm{K}$, several techniques to cool down scanning probe microscopes to the sub-kelvin regime have been established. Latest temperature records reaching down to $T = 10\,\mathrm{mK}$ [52, 53, 54, 37, 55, 56, 57, 58] are achieved by dilution refrigerators (DR). Of these

groups, only Assig et al. [37] reported an electron temperature below 100 mK ($T_{\mathrm{el}} = 38$ mK). This DR exhibits a magnet allowing the application of magnet fields up to $B = 14$ T perpendicular to the sample and a 0.5 T in-plane magnetic field. Since tip and sample are arranged in stages, this system does not provide an optical access to the tip and sample chamber. One of the leading DR-STM systems is located at the NIST [53]. It depicts a versatile SPM system as it is fully UHV compatible, exhibiting a 15 T magnet, five contacts each on sample and tip stage, and an xy-coarse movement of ± 1.5 mm. A limited optical access to the sample stage is achieved parallel to the tip through a small hole in the tip holder and the 3 m distant top flange which is also used for sample and tip exchange.
The DR is cooled using the mixing heat of ^{3}He and ^{4}He. Operation is possible in a single shot mode (t_{hold} only a few hours [55]), where all the ^{3}He is pumped out of a mixing chamber and still, or in persistent mode, where the segregated ^{3}He is reintroduced to the mixing chamber for a closed cycle operation. To control the pumping speed at the still and in the persistent operation mode, mechanical pumps are needed for the cooling process. This naturally leads to mechanical vibration. Even with the extensive effort in using several damping stages and anechoic rooms, these vibrations seem to limit the achievable z-stability in STM measurements. Reported stabilities are down to 4 pm at a bandwidth Bw = 285 Hz [37]. Roychowdhury et al. report for their double tip STM a stability of $\delta_z = 1.75$ pm ($T_{\mathrm{el}} = 184$ mK, $B = 13.5$ T, no UHV, no optical access). Unfortunately, this value is not significant, since it was extracted in a scanning operation without detailed information about bandwidth and scanning parameters [57]. An exceptional $\delta_z = 0.2$ pm has been reported by Galvis et al. [58], but it also lacks information about bandwidth or parameters this measurement has been performed with, and uses the magnet as an additional damping stage ($T_{\mathrm{el}} =$ n.a., $B_z = 5$ T, $B_{xy} = 1.5$ T, no UHV, no optical access). Pelliccione et al. [59] ($T_{\mathrm{el}} = 45$ mK) and den Haan et al. [60] started to combine DRs with the cryogen-free technology of pulse tube refrigerators for SPM systems that put up with highly enhanced mechanical vibrations.
The latest approach to sub-kelvin cooling is the Joule-Thompson cryostat designed by Wulfhekel [61] ($T_{\mathrm{el}} = 1.15$ K, $B = 3$ T, fully UHV, optical access). The base temperature initially using ^{4}He was $T = 930$ mK and $T = 800$ mK after adding ^{3}He to the mixture [62]. The lateral drift $v_{d_{xy}}$ of tip and sample in this system is smaller than 20 pm/h, similar to the vertical drift $v_{d_z} < 20$ pm/h extracted from $I(z)$-spectroscopy. While scanning, the z-stability is $\delta_z = 0.5$ pm and 5 pm along the fast and the slow scanning direction respectively.
The traditional approach to reach sub-kelvin temperatures, which is also used in the system described in this thesis, is a ^{3}He-cryostat [63, 64, 36, 65]. Using

the higher vapour pressure of ^{3}He towards ^{4}He makes it possible to reach temperatures of about $T = 300\,\mathrm{mK}$ (see Section 3.3). The advantage here is that the vapour pressure reduction of ^{3}He can be achieved using sorption pumps and without any active mechanical pumps while the system is at base temperature. Here, the amount of ^{3}He limits t_{hold}, the time available at the lowest temperature. The system of Wiebe et al. can operate for $t_{\mathrm{hold}} = 30\,\mathrm{h}$ at $T = 315\,\mathrm{mK}$ ($T_{\mathrm{el}} = 315\,\mathrm{mK}$, $\delta_z > 5\,\mathrm{pm}$ determined while scanning, $B = 14\,\mathrm{T}$, full UHV, optical access outside the cryostat) [36]. Recently Kamlapure et al. reported on a new ^{3}He-system [65], with which they could achieve $\delta_z > 2\,\mathrm{pm}$ ($T_{\mathrm{el}} = 500\,\mathrm{mK}$, $B = 9\,\mathrm{T}$, no UHV, no optical access). Most recently the Wiesendanger group reported on their new ^{3}He-UHV system [66]. Although it is an AFM system the performance requirements are similar. Operating at $T = 350\,\mathrm{mK}$ is possible for $t_{\mathrm{hold}} = 12\,\mathrm{h}$ and their z-stability is limited to $\delta_z = 2.8\,\mathrm{pm}$ (determined while scanning, $B = 10\,\mathrm{T}$, full UHV, optical access outside the cryostat).

Table 2.1.: List of previously reported sub-Kelvin STM systems with outstanding performances - Distinguished are four different cooling mechanisms: vapour pressure reduction of ^{3}He via sorption pump (^{3}He), dilution refrigerator (DR), cryogen free pulse tube (PT) and Joule-Thompson (JT). Presented values are taken or extracted from the data of the cited reports.

Location	Year	Type	T	T_{el}	δ_z	Magnet[1]	UHV[2]	Opt. acs.
Berkley [63]	1999	^{3}He	240 mK	n.a.	0.5 pm (scan)	7 T	no	no
Geneva [64]	2000	^{3}He	275 mK	n.a.	n.a.	14 T	yes	outside
Hamburg [36]	2004	^{3}He	315 mK	315 mK	5 pm (scan)	14 T	yes	outside
Tokyo [52]	2007	DR	30 mK	< 350 mK	n.a.	16 T[3]	no	no
NIST[4] [53]	2010	DR	10 mK	n.a.	2 to 4 pm @ 100 Hz	15 T	yes	limited
Madrid [54]	2011	DR	100 mK	n.a.	5 pm (n.a.)	8 T	no	no
KIT, Karlsruhe [61]	2011	JT	800 mK	1.15 K	5 pm	3 T	yes	yes
TIFR, Mumbai [65]	2013	^{3}He	350 mK	≈ 350 mK	≈ 2 pm @ 200 Hz	9 T	no	no
Stanford[5] [59]	2013	PT	15 mK	45 mK	2.1 nm @ 1 kHz	9 T, 3 T	no	no
MPI, Stuttgart [37]	2013	DR	15 mK	38 mK	4 pm @ 285 Hz	14 T, 0.5 T	no	no
Princeton [55]	2013	DR	20 mK	250 mK	< 2 pm (scan)[6]	14 T	yes	outside
MPI, Stuttgart [56]	2013	DR	30 mK	140 mK	< 15 pm (scan)	14 T	no	n.a.
Maryland[7] [57]	2014	DR	30 mK	184 mK	1.75 pm (scan)	13.5 T	no	no
Leiden [60]	2014	PT	n.a.	n.a.	$1\,\mathrm{pm}/\sqrt{\mathrm{Hz}}$	none	no	no
Madrid [58]	2015	DR	100 mK	n.a.	0.2 pm (0.3 T, scan)	5 T, 1.5 T	no	no
Hamburg[8] [66]	2016	^{3}He	350 mK	n.a.	2.8 pm (scan)	10 T	yes	outside

[1] For 3-axis vector magnets the two corresponding maximal fields are given.
[2] Referring to the whole system without cryogenic pump operating, i.e. at 300 K.
[3] Implemented during my time at the University of Tokyo.
[4] 5 contacts at sample an tip stage each. $1.5 \times 1.5\,\mathrm{mm}^2$ coarse positioning.
[5] T_{el} determined by Coulomb blockade thermometry.
[6] z-stability stated to be comparable to [53].
[7] dual tip STM.
[8] AFM, most recent ^{3}He-UHV-SPM system.

3. Design of the low-temperature UHV-system

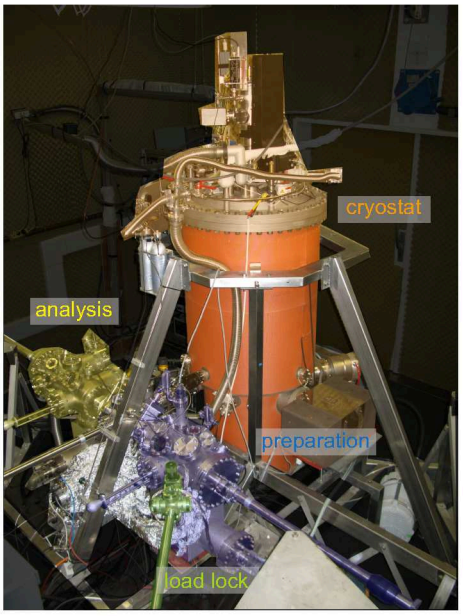

Figure 3.1.: 390 mK UHV-system in an anechoic room – Three-chamber UHV-LT-system, consisting of a preparation chamber (blue) with a load lock (green), analysis chamber (yellow) and a UHV-cryostat (orange).

The SPM system described in this work is a three-chamber UHV-system designed by Stefan Becker [67]. The three main sections are the preparation chamber, the analysis chamber and the cryostat. All chambers are connected via an in-situ transfer system. The samples are locked into the system through a load lock connected to the first main section, the preparation chamber. It is designed for sample annealing using a resistance heater and electron beam heater for temperatures up to $T = 3700\,\mathrm{K}$[1], sputtering or plasma ion bombardment. From here, samples can be transferred into the analysis chamber or straight to the cryostat. The analysis chamber is designed for preliminary sample investigations such as low energy electron diffraction (LEED) and exhibits a port for

[1] Limited by the melting point of tungsten.

a room temperature STM. Furthermore, it is aided by six ports, of which, for this work (Section 4.3.3), one port is occupied by a home-built Pb evaporator. A more detailed description can be found in [67]. The UHV cryostat, equipped with a 14 T superconducting magnet, is used for the main investigations in this thesis and is described in more detail in the following sections.

3.1. Design of the cryostat

The original intention was that the whole cryostat, consisting of a UHV hull, LN_2-insert, ^{4}He-insert and ^{3}He-insert would be constructed by *CryoVac GmbH & Co. KG*. However, the ^{3}He-insert, the core part of the cryostat, had to be redesigned to adjust the system to the requirements. All components of the cryostat meet the requirements for acquiring a UHV at room temperature. The hull is embedded with heating mats and the cryostat base is resting on a heating plate for an all-over bake-out procedure. The system can be heated up to $T = 120\,^\circ$C, while the magnet has to be kept below $T = 85\,^\circ$C. In the bake-out procedure this can be realised by air-cooling via the ^{4}He filling line. This ensures a base pressure of $p(T = 300\,\mathrm{K}) = 2 \cdot 10^{-10}$ mbar in the cryostat.
The cooling-system is separated into three inserts (Figure 3.2). The outer shielding is realised by an LN_2-tank with a filling volume of $V_{LN_2} = 120\,$l. The LN_2-tank is filled with Cu wool to inhibit bubbling of LN_2. Inside the LN_2-insert is the ^{4}He-insert. The top consists of a ^{4}He-tank with $V_{^4He} = 102\,$l. The exhaust lines of the ^{4}He-tank are connected to a shield (not shown) lying in between the LN_2 and ^{4}He-tank to enhance the ^{4}He hold time. Directly below lies the 1K-pot with $V_{1K} = 5\,$l. It can be filled with ^{4}He via a direct line from the tank above and is connected to a pumping line to cool the liquid by vapour pressure reduction. Attached to the bottom of the 1K-tank is the magnet tank, filled with ^{4}He and containing a single axis 14 T-NbTi/Cu solenoid magnet. The shielding of the LN_2 & ^{4}He-tanks is elongated around the 1K-pot and the magnet tank. To enable access to the inner part of the cryostat the shielding can be opened externally at the height of the sample transfer, which is also the height of the preparation and analysis chamber. The centre of the system incorporates the ^{3}He-insert, with the microscope head connected to its bottom. Using an electrically driven z-manipulator, the insert can be positioned vertically relative to the rest of the cryostat. This allows the microscope head to be moved between positions for sample transfer, sample preparation and cooling of the microscope head (see Section 3.3).

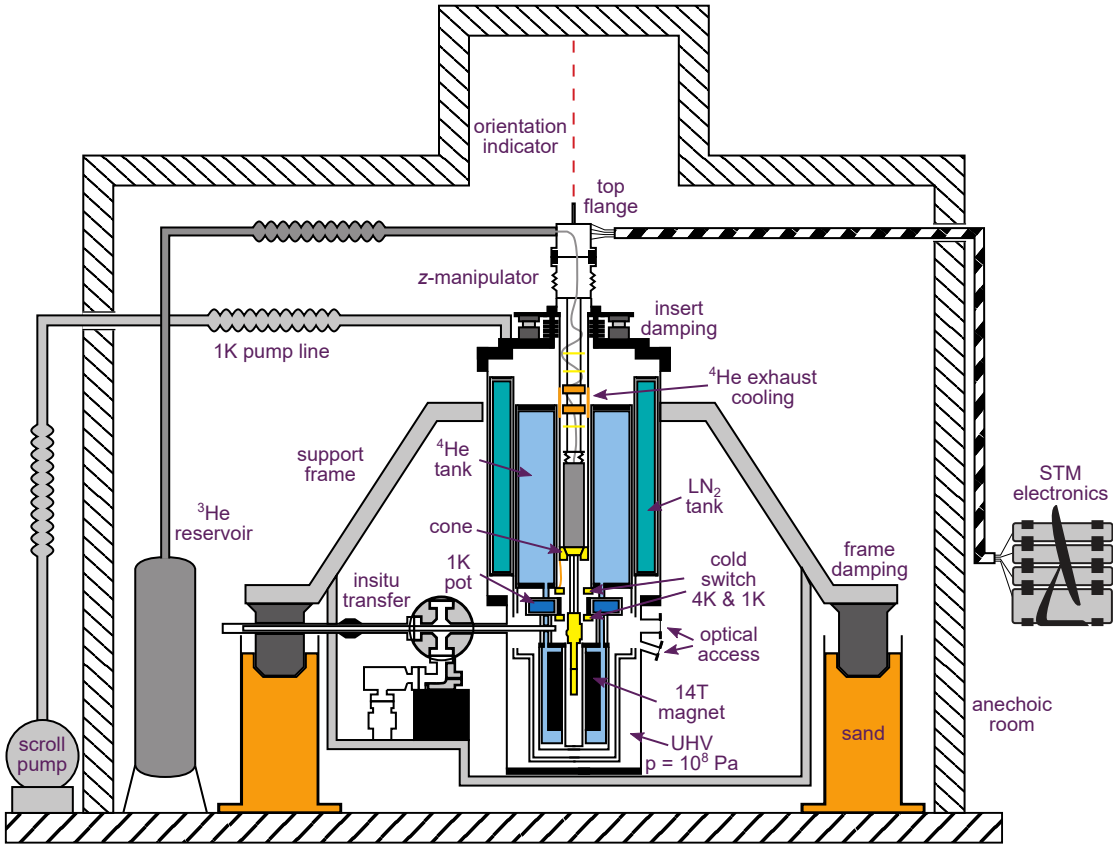

Figure 3.2.: Schematic cut through the UHV-LT system in an anechoic room – System placed inside an anechoic room and resting on air-damping feet. The ^{3}He-insert contains an additional air-damping stage for mechanical isolation from the system.

3.2. Design of the ^{3}He-insert

The ^{3}He-insert is home-built with the support of *CryoVac*. The original design exhibits the necessity of an insert rotation and z-movement, leading to strong demands on position adjustment. Experiments with a similar system at the University of Hamburg have shown that this approach was unfeasible and had a high risk of failure. The main challenge in the design is achieving switchable thermal contact between 1K-pot and ^{3}He-pot, low heat transfer between top flange and sorption pump as well as sorption pump and ^{3}He-pot, and mechanically stable connection of the ^{3}He-pot (cf. Figure 3.3).

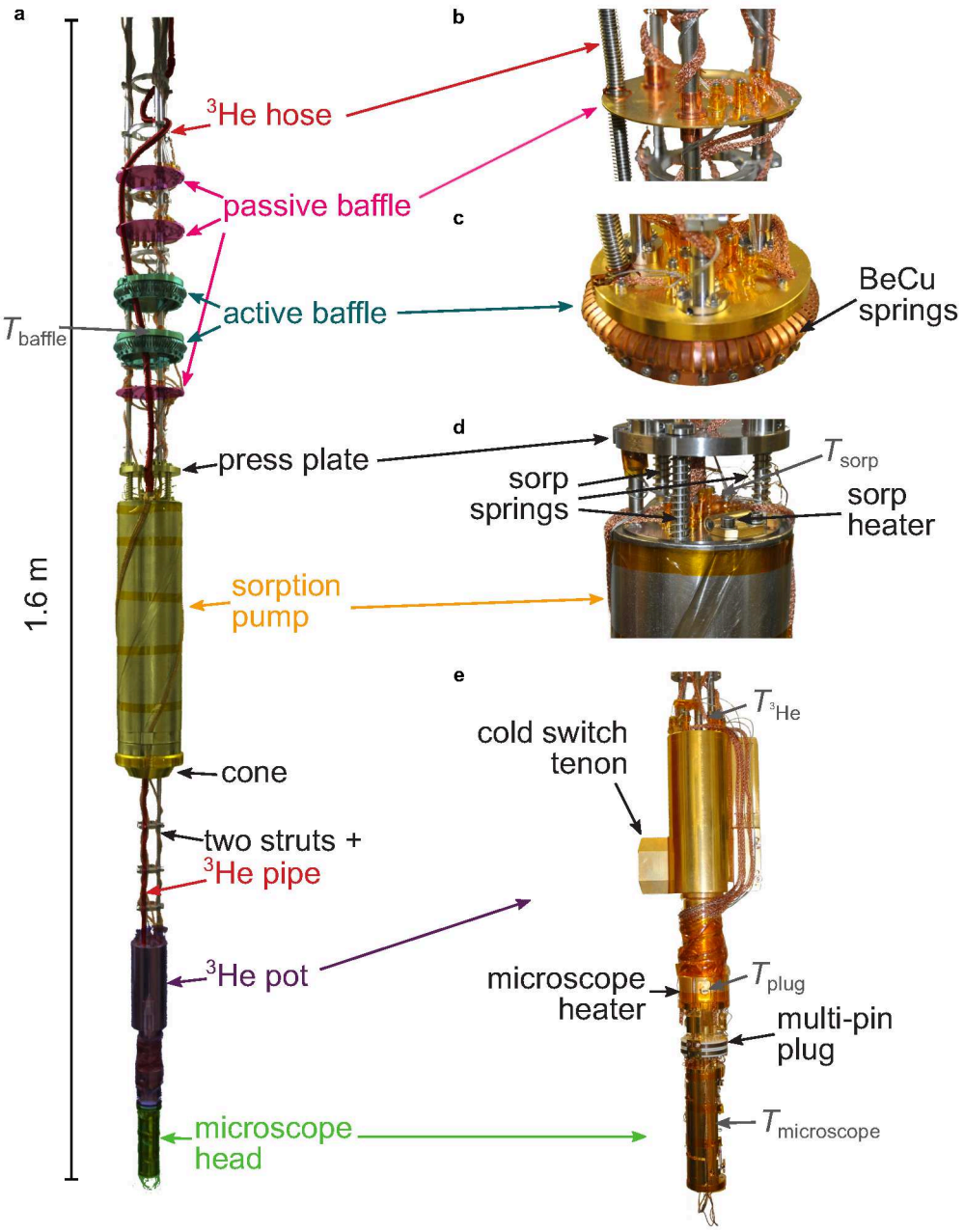

Figure 3.3.: Home-built ^{3}He-insert – (a) ^{3}He-insert with main sections emphasised by colouring and shown enlarged in (b) to (e). The positions of temperature sensors are marked with grey T's. Designed with support from *CryoVac* and in cooperation with Mike Pezzotta.

3.2.1. Thermal conductivity along the insert

The shielding from radiation heat input from room temperature of the top flange to the sorption pump is realised by a stratification of three passive and two active baffles. The passive baffles are gold coated, copper radiation shields (Figure 3.3(b)). The active baffles (Figure 3.3(c)) have BeCu-springs, radially aligned at the outside, which brings the baffles in contact with a copper pipe connected via a copper strand with the ^{4}He-exhaust lines. This allows a vertical movement of the insert and fixes the baffle temperature between $T_{\text{baffle}} = 40\,\text{K} - 70\,\text{K}$, depending on the amount of ^{4}He-exhaust. Twisting the wires to these baffles also guarantees a temperature reduction of the wires at this position. The wiring is wound tightly around the sorption pump (Figure 3.3(d)) for a good thermal contact, and to prevent radio-noise by movement of the wiring. The connection of the sorption pump cone and the ^{3}He-pot (Figure 3.3(e)) is made by a tripod of stainless steel pipes (struts) with a wall thickness of $d = 0.1\,\text{mm}$, as a compromise of mechanical stability and low thermal conductivity. These pipes will be cooled down to $T = 390\,\text{mK}$ and are close to the magnet. Thus, it had been taken care of that the pipes show no ferromagnetism after the soldering and welding process. At the same time, many hard, thermally isolating, non-ferromagnetic metals cannot be used, since they exhibit superconductivity at low temperatures. For instance, commercially available Ti rods have highly varying impurity compounds and an undetermined critical temperature, often with $T_C > 500\,\text{mK}$ [68, 69]. The ^{3}He-pot is made of oxygen free copper for enhanced thermal conductivity at low temperatures. To ensure the cooling of the wiring to $T = 390\,\text{mK}$, the wires are twisted to the top of the ^{3}He-pot and wound around the base, on the way to the microscope head. The microscope is screwed to a multi-pin plug, which allows a replacement of the microscope head.

3.2.2. Switchable thermal connectors

In order to achieve a cooling of the ^{3}He-pot down to $T = 390\,\text{mK}$ several thermal contacts must be adjustable. A typical method of making a switchable thermal contact is to bring two co-radial cones into contact. Fabrication of the two cone counterparts in one process allows a large contact area and thus a good thermal contact by bringing the two surfaces together. A lateral fixation of the two pieces is also achieved. This method is used to cool the sorption pump. The contact pressure is adjusted by the springs on top of the sorption pump. Moving the insert further downwards, after the cones are brought into contact, leads to a compression of the springs, which have an initial tension of 2 cm.

This leads to a contact force of $|\boldsymbol{F}_{\text{sorp}}| \approx 90\,\text{N}$[2]. The vertical position of the microscope head stays fixed for all indentation depths. The counter-cone is connected with a copper strand to the ^{4}He-tank, providing a thermal contact and at the same time suppressing the transmission of mechanical vibrations. In the former design, a similar approach was used for the thermal contact of the ^{3}He-pot. Since this method confines the movement in the direction the contacts are made (z), the cones were segmented and a rotation was necessary. Another complication with this approach is the direction in which the contact force is applied. To enhance the thermal conductivity, the contact pressure of the cones has to be increased. This would lead at the same time to more force applied to the thin-walled struts. Thus, a different thermal contacting is used instead (cf. Figure 3.4). The ^{3}He-pot has a tenon at the side of the body. This tenon can be moved vertically into a guiding rail (mortise) with a high pressure piston coming from the side (cold switch). Driven by ^{4}He-gas, the tenon can be fixed inside the mortise. Pressurising the pistons up to $p = 40\,\text{bar}$ ($|\boldsymbol{F}_{\text{switch}}| = 1.6\,\text{kN}$) enables the adjustment of the contact pressure/thermal contact between ^{3}He-pot and mortise/pistons. By this, no force is applied on the struts. Additionally, lateral forces applied to the ^{3}He-pot or microscope body are absorbed by this connection. The system features two of these cold switches. One is screwed to the 1K-pot (cold switch 1K) to cool down the ^{3}He-pot to the temperature of the 1K-pot. Here a good thermal conductivity is important for fast heat transfer of the condensing ^{3}He to the 1K-pot. A second cold switch is mounted to the bottom of the ^{4}He-tank. When the insert is raised to the transfer position, the sample in the microscope is in the transfer plane and the tenon is inside the mortise of the 4K-switch. Closing the switch fixes the temperature of the microscope to $T = 25\,\text{K}$ when the shielding is opened for e.g. optical access, sample transfer and evaporation directly into the microscope. At the same time, a possible lateral force applied to the microscope, while sample and tip exchange, is absorbed by the switch, guarding the struts and ^{3}He-pipe.
With the movement of the insert along the z-direction, the tenons have to be manoeuvred into the cold switches and the cones of the sorption pump have to match. The distance of the tenon and pivot point (insert damping stage) of the insert is about 1.5 m, so that a deviation of 1° would translate the tenon 3 cm laterally. To monitor the lateral movement of the insert and to be able to adjust the alignment externally, a laser is mounted to the top of the insert pointing in the opposite direction of the insert. All lateral movements of the insert are visualised by changes in the position of the laser spot.

[2] Three springs with $k = 0.67\,\text{N/mm}$ and $m_{\text{sorp}} \approx 4.5\,\text{kg}$.

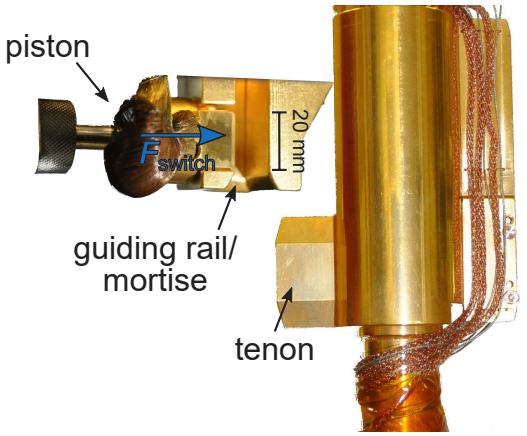

Figure 3.4.: Cold switches for switchable thermal contact of the ^{3}He-pot – Cold switch mounted to the 1K-pot used for ^{3}He condensing. The tenon of the ^{3}He-pot can be inserted in the mortise by moving the insert vertically. The piston is moveable with ^{4}He-gas pressure (up to 40 bar) towards the tenon and can pinch it in the mortise with $|\boldsymbol{F}_{\text{switch}}| = 1.6\,\text{kN}$. A similar switch is mounted to the bottom of the ^{4}He-tank for sample transfer. Designed in cooperation with Mike Pezzotta and *CryoVac*.

3.3. Cooling procedure

The repeatable cooling cycle of this ^{3}He-refrigerator can be subdivided into four states (cf. Figure 3.5). In the initial state all ^{3}He is in the gas phase and most of the gas in the ^{3}He-reservoir is located at room temperature with $p_{^3\text{He}} = 800\,\text{mbar}$. In case of a leakage, this underpressure compared to the atmosphere would lead to contamination instead of a loss of ^{3}He. The cold switches are open and the sorption pump is not cooled. In this position, the sorption pump heats up slowly and is only cooled by the active baffles (^{4}He-exhaust) lying above the pump. The direct line to the 1K-pot is opened, so that it is completely filled with L^{4}He.
To start the condensing (Figure 3.5(b)), the tenon is moved to the height of the 1K cold switch and the switch is closed. Closing the direct line and pumping the ^{4}He in the 1K-pot reduces the vapour pressure and cools down the 1K-pot as well as the ^{3}He-pot. The vapour pressure of ^{3}He at $T = 1.5\,\text{K}$ is $p_{^3\text{He}} = 68\,\text{mbar}$ [70] so that most of the ^{3}He is liquefied inside the ^{3}He-pot. The amount and speed of ^{3}He liquefied could be increased by storing the ^{3}He at high pressure in the reservoir, at the cost of a higher risk of ^{3}He loss and stronger demands on the fragile ^{3}He pipes. The contact pressure of the cold switch can be enhanced, leading to a better heat transfer and a positive influence on the condensing time. After two to three days most of the ^{3}He is liquefied ($V_{^3\text{He},1\,\text{bar}} = 100\,\text{l}$).

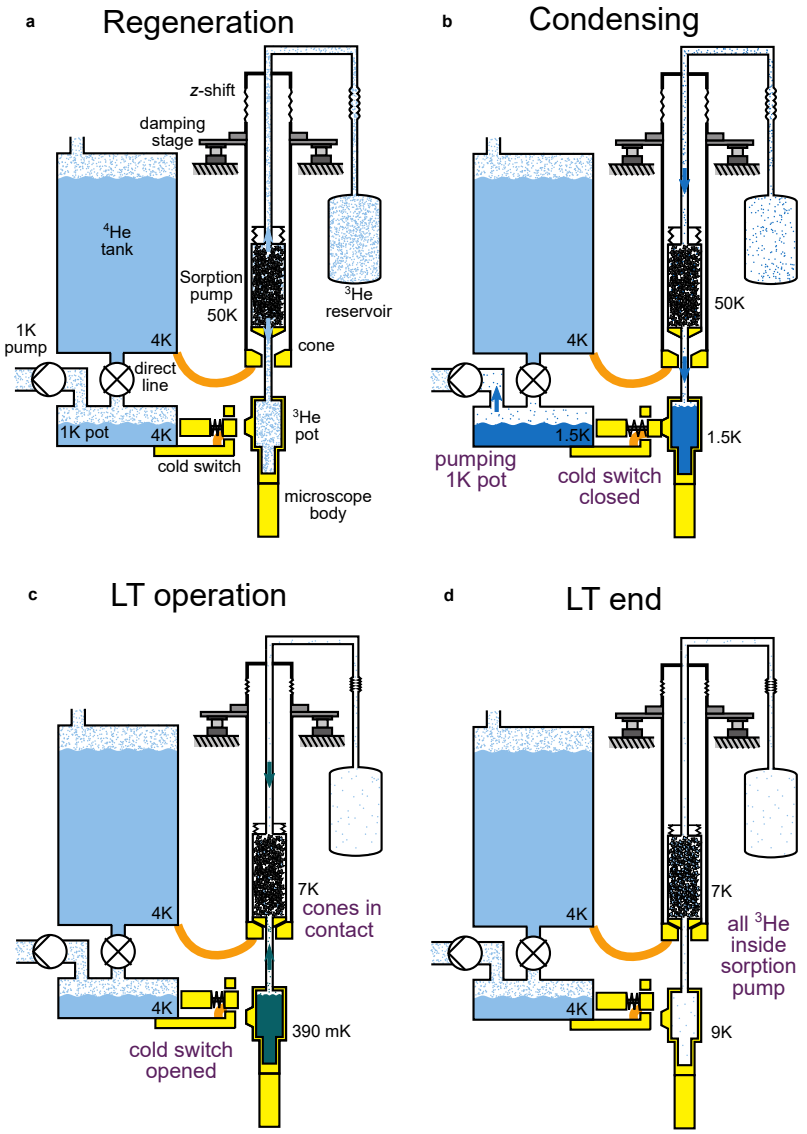

Figure 3.5.: Cooling procedure for operating at T = 390 mK – (a) Initial or regeneration state: sorption cones separated. Cold switch opened. $T_{\mathrm{sorp}} > 55\,\mathrm{K}$. ^{3}He is gaseous. (b) Condensing state: 1K-cold switch closed. 1K-pot cooled to $T_{1\mathrm{K}} = 1.5\,\mathrm{K}$ by vapour pressure reduction. ^{3}He starts to condense. (c) Low-temperature operation: 1K-cold switch opened. Sorption cones in contact $T_{\mathrm{sorp}} = 7\,\mathrm{K}$. ^{3}He starts to be adsorbed in the sorption pump ($T_{^3\mathrm{He}} = 390\,\mathrm{mK}$). (d) Final state: all ^{3}He adsorbed. Microscope temperature rises immediately to $T_{\mathrm{microscope}} = 9\,\mathrm{K}$. Heating of the sorption pump would start the cycle at (a) again.

To cool down the ^{3}He further, the cold switch is opened and the insert moved downwards so that the sorption pump is cooled by the counter cone (Fig-

ure 3.5(c) - low-temperature (LT) operation). In this position the microscope, located at the centre of the magnet, is in the measurement position. When the charcoal inside the sorption pump is cooled below $T_{\mathrm{sorp}} = 18\,\mathrm{K}$ it starts to adsorb the ^{3}He sufficiently. The vapour pressure reduction leads to cooling of the L^{3}He. Due to the higher vapour pressure of ^{3}He compared to ^{4}He, the liquid can be cooled down further to $T_{^3\mathrm{He}} = 390\,\mathrm{mK}$. The pump at the 1K-pot is not needed in this state and the sorption pump is operating without any moveable parts, leaving no mechanical vibrations of the cooling process.
It takes more than ten days for all the ^{3}He to be pumped into the sorption pump (Figure 3.5(d)). Due to the low heat capacity of copper at low temperatures, the temperatures of the ^{3}He-pot and microscope head increase instantaneously when the L^{3}He is empty. The equilibrium temperature is about $T = 9\,\mathrm{K}$. The sorption pump must be heated to start the regeneration. Retracting the pump from the cone leads to a temperature increase of the sorption pump and leads to a release of the ^{3}He-gas. This process can be accelerated by the heaters mounted on the top of the sorption pump. Best condensing performance is achieved when not all ^{3}He goes back to the reservoir and therefore condensing is started while regenerating the sorption pump. Above $T_{\mathrm{sorp}} = 55\,\mathrm{K}$ most ^{3}He is desorbed.

3.4. Decoupling from mechanical vibration

To maintain and exploit the high lateral and vertical resolution, one of the main advantages of the STM, a lot of care must be taken to avoid the input of mechanical vibrations. The system is placed in an anechoic room with no mechanical pumps running during the measurement operation (cf. Figure 3.2). The UHV-chambers and the cryostat rest on a carefully designed, sand-filled support frame, decoupled from the floor by air damping feet, resting in sand [67]. Residual mechanical connections to the walls are the ^{4}He-exhaust line, 1K-pump line and the electrical wiring. Those connectors are corrugated hoses and are fixed at the walls of the anechoic room to minimise vibrational input into the system. The ^{3}He-insert possesses another decoupling stage from the system. The insert, together with the counter-cone of the sorption pump is resting on three air damping feet. The remaining mechanical connections to the cryostat are the edge-welded bellow at the top of the cryostat and the copper strand connection of counter-cone and ^{4}He-tank. Further connections are the flexible wiring of the experimental setup and a corrugated hose to the ^{3}He-reservoir.

3.5. The SPM head

The microscope head attached to the ^{3}He-insert is a home-built combined AFM/STM (Figure 3.6(a)), which I developed in the framework of my diploma thesis [71]. It is designed for UHV applications at $T = 300\,\mathrm{mK}$ and high magnetic fields ($B = 14\,\mathrm{T}$). The body, made of phosphorous bronze, serves as electrical shielding and exhibits a good thermal conductance at low temperature and high mechanical stability. The microscope is equipped with a multi-pin plug, allowing the microscope head to be easily exchanged. A special feature of this microscope is the versatility of the experimental techniques that can be performed. The xy-stage features a piezo motor allowing a lateral displacement of $2 \times 2\,\mathrm{mm}^2$ for a positioning of SPM tip relative to the sample. While for STM two electrical contacts (bias voltage and tunnelling current) are needed, one on the sample stage and one at the tip, this microscope exhibits a total of seven. Five at the xy-stage and two at the scanner stage. The uniform design of the sample and tip holder (cf. Figure 3.6(b)) allows an interchange of the stage usage for tip and sample. With the STM tip located at the scanner stage, the five contacts at the xy allow transport measurements and STM measurements on transport samples (see Section 4.2.3 & Section 4.3.2).

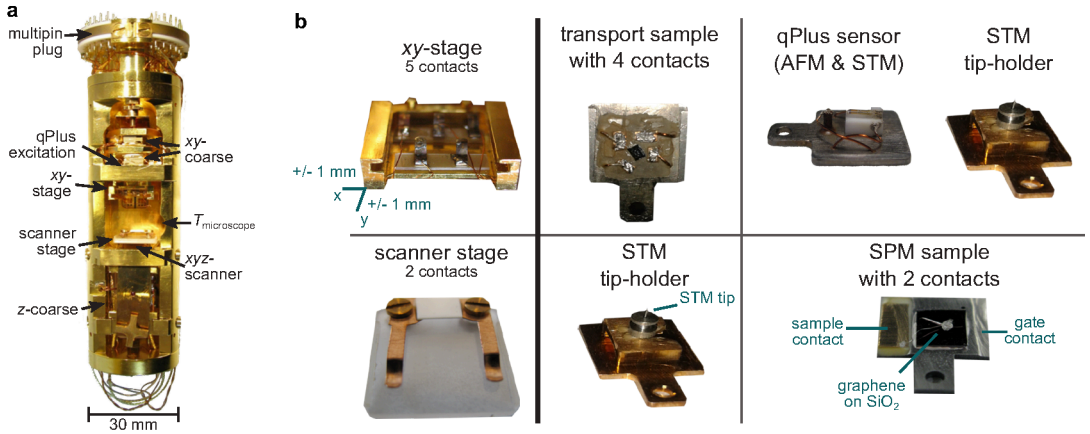

Figure 3.6.: Home-built combined STM/AFM – (a) Image of the microscope head. The top part consists of an xy-coarse move stage. The bottom part is the z-approach and the xyz-scanner tube. The position of the temperature sensor used for determination of the experimental temperature is marked with $T_{\mathrm{microscope}}$. (b) Possible operation modes of the microscope head. Upper row: xy-stage (left) and possible loads for this stage. Lower row: scanner stage (left) and possible loads for this stage. [71].

As shown in Section 4.2.2, the contacts of the xy-stage can be used for a qPlus

sensor or an STM tip. This leaves two contacts for the sample on the scanner stage for SPM experiments, with an additional contact, for instance, a gate contact. This microscope head is used for the characterisation of the system performance as well as the experimental results discussed in the second part of this thesis (Section II).

4. Characterisation of the ^{3}He-system

4.1. Cryostat performance

4.1.1. Holding time and temperature

Using the cooling operation described in Section 3.3, the system can be cooled down to $T = 376\,\mathrm{mK}$. A condensing time of 36 hours turns out to be suitable, leading to a holding time of seven days at $T = 400\,\mathrm{mK} \pm 20\,\mathrm{mK}$. To optimise the condensing cycle, it is beneficial to avoid allowing too much ^{3}He to warm up to room temperature. The warming of the sorption pump and condensing speed of the 1K-stage therefore need to be balanced out, keeping the ^{3}He below 150 mbar. It was ascertained that a suitable technique for doing so is to initially heat the sorption pump to 20 K to start the regeneration process and leave it to warm up from there. To estimate the maximal holding time at low temperatures, all ^{3}He has to be liquefied. For this, condensing is performed over three days, slowly heating the sorption pump to $T_{\mathrm{sorp}} = 51\,\mathrm{K}$ and cooling the ^{3}He-pot to $T = 1.52\,\mathrm{K}$ (Figure 4.1(a)). Releasing the cold switch leads to a slight increase in temperature of the microscope (high heat capacity of liquid ^{3}He) and a noticeable drop of the 1K-pot temperature due to loss of heat load. Within one hour the sorption pump is cooled below 15 K and after two hours the microscope temperature reaches 400 mK. This longer condensing period led to a total holding time of $t_{\mathrm{hold}} = 10.5\,\mathrm{days}$. An indicator for the remaining holding time is the temperature change at 3.5 days before the end of the holding time. Here the temperature increases to $T = 420\,\mathrm{mK}$ and shows temperature fluctuations with reproducible behaviour for every cooling cycle. This can be explained by the shape of the ^{3}He-pot. The bottom of the ^{3}He-pot, with a smaller diameter, accounts for one third of the total volume of the ^{3}He-pot. This smaller diameter leads to a smaller surface of the liquid ^{3}He. As soon as the pot is emptied to that level, the pumping speed of ^{3}He is reduced and T increases to $T = 420\,\mathrm{mK}$. The subsequent development of the microscope temperature can be correlated to the interior design of the ^{3}He-pot, which is not discussed in this work. The reproducible behaviour provides the opportunity to schedule long-term experi-

ments at low temperatures regarding the remaining holding time. In the earlier period of the temperature cycle, the temperature is lower and much more stable, typically $\overline{T} = 390\,\mathrm{mK} \pm 0.5\,\mathrm{mK}$.

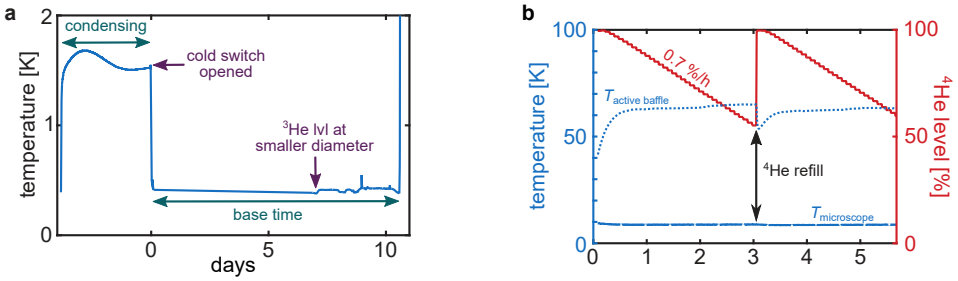

Figure 4.1.: Cryostat base temperatures and holding time – (a) Temperature of the microscope in a 390 mK cooling cycle (Section 3.3). First section: condensing combined with sorption pump heating. ^{3}He-pot linked to 1K-pot. Opening of the 1K-switch leads to a small temperature increase. Second section: LT operation, sorption cone in thermal contact with ^{4}He-bath. Third section: all ^{3}He inside the sorption pump. Immediate rise of microscope temperature. (b) Equilibrium state when all ^{3}He is inside the sorption pump, with a refilling of the ^{4}He-tank at day three (black double arrow). Showing the temperatures of the microscope and the active baffle, as well as the ^{4}He-bath filling level.

After the ^{3}He is pumped completely into the sorption pump, which is kept at 7 K, the microscope warms up to an equilibrium temperature of $\overline{T} = 8.7\,\mathrm{K} \pm 0.1\,\mathrm{K}$ (Figure 4.1(b)). This temperature also stays constant when the ^{4}He-bath is refilled. The refilling of L^{4}He leads to a large amount of ^{4}He-exhaust, causing the active baffles to cool down. This affects the high temperature bracing of the microscope wiring. Nevertheless, it only results in a minor temperature change of the microscope, keeping the system stable for time periods that are even longer than the refilling cycle of the ^{4}He-bath. With $t_{\mathrm{hold}} = 10.5\,\mathrm{days}$ at $T = 400\,\mathrm{mK}$ and infinite holding time at 9 K, the refilling cycles of L^{4}He and LN_2 turn out to be the limiting time scale for the duration of SPM experiments. The Helium level depicted in Figure 4.1(b) is the filling of the upper ^{4}He-bath. This means that it indicates the amount of ^{4}He above the superconducting magnet and a ^{4}He-level of 0 % renders the time when the system has to be refilled, leading to a maximum filling cycle of six days. The LN_2-consumption behaves similarly.

4.1.2. Optical access

When the microscope head is lifted to the transfer position (^{3}He-tenon at the 4K-cold switch), opening the large shields of the L^{4}He and LN_2-baths provides optical access to the tip and sample. Figure 4.2(a) shows an example of the view into the STM, with all ports aligned to the centre of the microscope body[1]. Two CF100 view ports and one CF60 view port allow optically controlled sample and tip exchange, as well as tip approach and positioning (Figure 4.2(b)). A long-distance microscope[2] is used to improve the optical access. Using the CF60 view port enables the view onto the xy-stage and through the CF100 view port, the view can be adjusted to the scanner stage. With this setup, structures down to 5 µm can be resolved. The evaporator port is aligned to a sample stage (not shown) that is attached to the L^{4}He-shield and in line with the xy-stage of the microscope head. An evaporation onto a cold sample surface can either be performed on the evaporation stage being $d = 180$ mm away from the evaporator or directly onto the sample located inside the microscope ($d = 270$ mm)[3]. Being thermally connected to the ^{4}He-bath, the microscope temperature can be kept at $T = 25$ K while the shielding is fully opened.

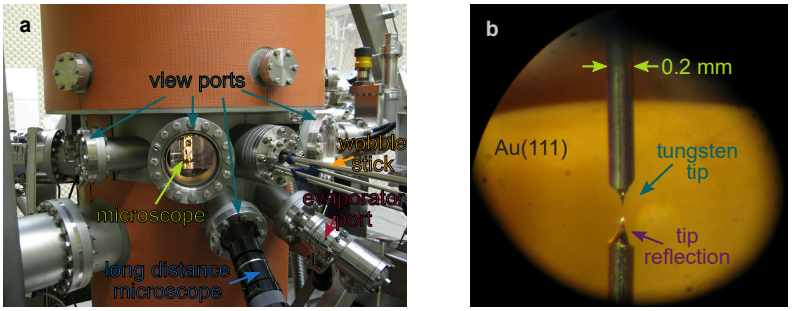

Figure 4.2.: Access to the microscope head – (a) Image of cryostat showing the view ports and manipulator. Microscope in transfer position (tenon is connected to 4K-cold switch). LN_2 and L^{4}He-shields opened for optical access. $T \approx 25$ K. (b) View through central view port in (a), where the STM head is visible, using the long-distance microscope. Image shows a tungsten tip coarse approached to a Au(111). Distance between tip and tip reflection ≈ 50 µm

[1] With the exception of the view port on the left, which is aligned towards the sample transfer leading to the preparation and analysis chamber of the UHV-system.

[2] Infinity Model K2/SC, with CF-1/B objective.

[3] The distances are valid for an existing Cs evaporator mounted onto a z-shift that can be extended up to the LN_2-tank. A different evaporator design might achieve even shorter evaporator-sample distances.

4.2. Imaging performance

A key advantage of SPM is the subatomic resolution in lateral direction and height. Significant effort is required to improve those key figures. The system, located inside an anechoic room, is elevated on an air damping stage to ensure a separation from acoustic noise and vibrations in the environment. At low temperatures the system itself can produce new sources of vibration. For instance, the boiling of LN_2, He-gas resonances and mechanical pumps for a reduction of vapour pressure of cryogenic liquids, such as L^{4}He, L^{3}He in dilution refrigerators and Joule-Thompson cryostats. Cryogen-free solutions based on, e.g. pulse tube, show vibrations of such high amplitude that it only recently became possible to obtain a stable STM topography image with atomic resolution [60].
This system, which I developed, avoids the use of mechanical pumps in the low-temperature state while operating STM experiments. The ^{4}He-bath is mechanically decoupled from the insert. The sorption pump, at the ^{3}He-insert, operates by adsorbing ^{3}He on charcoal surfaces, resulting in no mechanical vibrations or periodic movements of the cryogenic gas. With the microscope body at the end of the insert, and both tip and sample connected to the same body, this setup is mechanically very stable.

4.2.1. STM

xy-resolution and stability

The lateral resolution depends on the investigated sample surface. A clean and flat sample surface, preferably with large interatomic distances, has to be created in order to achieve atomic resolution. Cleaved semiconductor surfaces as InAs(110) or some metal surfaces, e.g. Au(111) and Ir(111), enable relatively easily achievable atomic resolution under UHV conditions. An atomic resolution can be hampered by adsorbates, contaminations, or a mismatch of tip and sample orbitals. Figure 4.3(a) shows the atomic structure of an InAs(110) surface, which was cleaved in-situ. A technique to enhance the atomic contrast is a reduction of the tip-sample distance. This can be done by increasing the tunnelling current. On the other hand, this also increases the electric field between tip and sample. The stronger tip-sample interaction can result in a tip-induced band bending or a displacement of adatoms. This can make it necessary to go to larger tip-sample distances, i.e. lower tunnelling currents. Atomic resolution with $I = 0.5\,\mathrm{pA}$ is still possible with this setup (cf. Figure 4.3(b)). The atomic rows of InAs (same area as in Figure 4.3(a)) are clearly resolved. At this low current, an additional feature arises from residual 50 Hz noise. The SPM controller could be identified as the origin of that interference. To remove this signal, the

power control communication wiring between the Nanonis scanner high voltage controller and Nanonis SPM controller have to be disconnected.

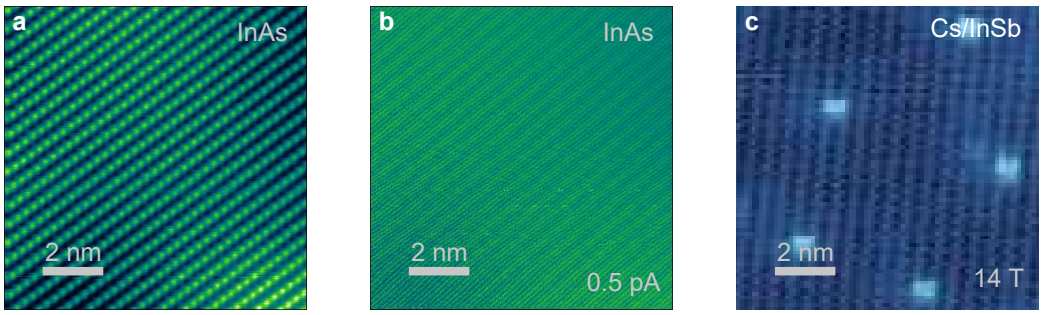

Figure 4.3.: Spatial resolution of the STM, unfiltered topography images with atomic resolution – (a) Typical scanning parameters on InAs(110). ($V = 500\,\mathrm{mV}$, $I = 1.5\,\mathrm{pA}$, time per line $t_{\mathrm{line}} = 1\,\mathrm{s}$, $10 \times 10\,\mathrm{nm}^2$, $400 \times 400\,\mathrm{px}$, $B = 0\,\mathrm{T}$, $T = 410\,\mathrm{mK}$) (b) Ultra-low current stabilisation ($I = 0.5\,\mathrm{pA}$). Atomic rows are still resolved. Line substructure is residual 50 Hz-noise. $V = 500\,\mathrm{mV}$, $I = 0.5\,\mathrm{pA}$, $t_{\mathrm{line}} = 1\,\mathrm{s}$, $10 \times 10\,\mathrm{nm}^2$, $400 \times 400\,\mathrm{px}$, $B = 0\,\mathrm{T}$, $T = 390\,\mathrm{mK}$) (c) High magnetic field topography image ($B = 14\,\mathrm{T}$) of a Cs/InSb sample. Bright dots are Cs atoms. Vertical lines: atomic rows with resolved atoms. Sections ($10 \times 10\,\mathrm{nm}^2$) of a typical overview image. ($V = 300\,\mathrm{mV}$, $I = 30\,\mathrm{pA}$, $t_{\mathrm{line}} = 1\,\mathrm{s}$, $50 \times 25\,\mathrm{nm}^2$, $400 \times 200\,\mathrm{px}$, $B = 14\,\mathrm{T}$, $T = 9.2\,\mathrm{K}$)

Investigation on Cs adsorbed on InSb will be shown in the second part of this thesis. This system is an example in which a low current is obligatory for a stable imaging of the surface. Together with high magnetic fields up to $B = 14\,\mathrm{T}$ it can become challenging to obtain a good lateral resolution. Low magnetic fields can further improve the imaging quality shown above. A further stabilisation of the tunnelling current can be observed for magnetic fields up to about $\pm 0.5\,\mathrm{T}$. Eddy currents induced in the microscope body are damping residual mechanical vibrations and enhance the stability. At high fields, as $B = 14\,\mathrm{T}$, the microscope body is fixed by the magnetic field and the damping stage between cryostat and microscope is bypassed. All vibrations inside the cryostat, e.g. LN_2 boiling and ^{4}He exhaust, are passed to the microscope. With these conditions, a high resolution can still be achieved, as shown in Figure 4.3(c), depicting a zoom of a typical overview image of a Cs/InSb surface. The stability of spectroscopy during magnetic field changes and at high magnetic fields are shown in the second part of this thesis (Section 7.3).

z-stability

Various different techniques are used to show the performance of the systems' STM imaging capabilities. The specification of a z-noise δ_z is the key parameter.

As for every type of noise, the question of the bandwidth at which it occurs is often either neglected or dealt with within the argumentation of typical scanning parameters [58, 57]. Choosing artificially slow scanning parameters can result in very low δ_z values, since the feedback loop in STM acts as a low-pass filter. Measuring an atomic corrugation with typical scanning parameters and reading noise on that corrugation as δ_z can be argued to be an adequate benchmark for performance that is achievable in operation, but is hardly suitable for an inter-system comparison.
Here, two more general approaches in determining δ_z are presented, with and without active feedback loop. With active feedback loop the z-signal is measured at a laterally fixed position. Feedback parameters are chosen as in a typical experiment with a line-time of $t_{\text{line}} = 0.5\,\text{s}$. 2×400^2 measurements are taken with a rate of 800 points per second (forward image shown in Figure 4.4). In addition to the presence of white noise, individual frequencies are also prominent. The histogram of the whole image yields a Gaussian with a σ-width of $\delta_z = 780\,\text{fm}$. As a result of a subsequent improvement of the STM controller, which is a source of electrical noise, a z-stability of $\delta_z < 600\,\text{fm}$ can be expected.

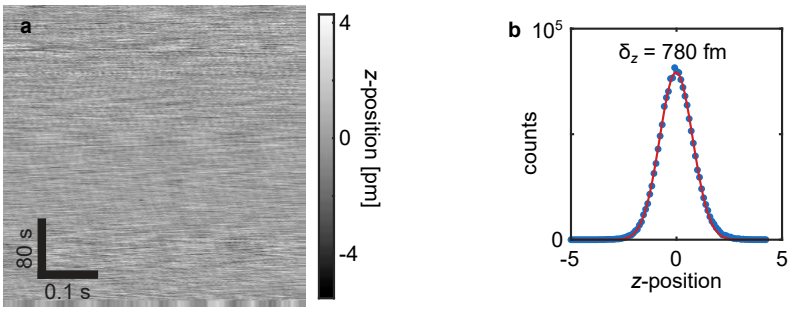

Figure 4.4.: z-noise of the system with active feedback loop – (a) Relative tip-sample distance change z acquired over time at a laterally fixed position ($400 \times 400\,\text{px}$, $0.5\,\text{s/line}$, $V = 500\,\text{mV}$, $I = 150\,\text{pA}$, $T = 400\,\text{mK}$, $B = 0\,\text{T}$, Feedback: $P = 300\,\text{fm}$, $\tau = 15\,\mu\text{s}$). (b) Histogram of the z-noise (blue dots) and Gaussian fit (red line), yield $\delta_z = 780\,\text{fm}$.

For the second determination of δ_z, the feedback loop is turned off while measuring the tunnelling current I (Figure 4.5(a)). The tunnelling current, as having an exponential z dependence, is sensitive to any mechanical vibration and electrical interference. The bandwidth of this method is given by a low pass filter implemented between amplifier and Lock-In[4] ($f_{\text{Bw}} = 700\,\text{Hz}$). The amplifier[5] exhibits a bandwidth of $f_{\text{Bw,Femto}} = 1\,\text{kHz}$ and the STM controller records

[4] Stanford SR-810.
[5] Femto DLPCA-200, Gain: $10^9\,\text{V/A}$.

with $f_{\mathrm{Bw,nanonis}} = 5\,\mathrm{kHz}$. The signal is measured for $t = 0.5\,\mathrm{s}$ at a laterally fixed position. From the $I(z)$-curve (inset Figure 4.5(a)) the current noise can be converted to the relative tip-sample displacement leading to $\delta_z = 1\,\mathrm{pm}$. In the Fourier transform of the current signal (Figure 4.5(c)) several frequencies stand out. Peaks at $f = 50\,\mathrm{Hz}$ & $620\,\mathrm{Hz}$ belong to the STM controller, creating electrical noise. Subtracting those frequencies from the signal, the mechanical stability is $\delta_z = 0.7\,\mathrm{pm}$. The dominating mechanical perturbation of the system is produced by the ^{4}He exhaust lines. The corresponding double peak structure around $f = 70\,\mathrm{Hz}$ shifts depending on the ^{4}He filling level by about 5 Hz and the intensity can be changed by adjusting the flow through the two main ^{4}He exhaust lines.

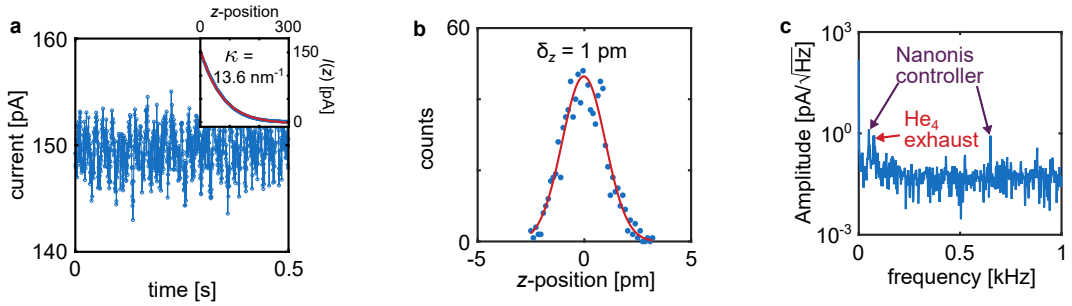

Figure 4.5.: z-noise determined by changes in the tunnelling current I without feedback loop – (a) Tunnelling current I obtained at a fixed lateral tip position (1000 points per 0.5 s, $V = 500\,\mathrm{mV}$, $I = 150\,\mathrm{pA}$, $T = 400\,\mathrm{mK}$, $B = 0\,\mathrm{T}$). Inset: $I(z)$-curve obtained at same position (blue) with fit $I = I_{\mathrm{max}} \exp(-\kappa z) + I_0$ (red line - $I_{\mathrm{max}} = 159\,\mathrm{pA}$, $\kappa = -1.36/\mathrm{Å}$, $I_0 = -3.7\,\mathrm{pA}$). (b) Histogram of the z-noise (blue dots) and Gaussian fit (red line), yield $\delta_z = 1\,\mathrm{pm}$. (c) Frequency spectrum of current signal in (a). Peaks at $f = 50\,\mathrm{Hz}$ and $f = 620\,\mathrm{Hz}$ are electrical noise produced by the STM controller. Double peak structure around $f = 70\,\mathrm{Hz}$ are mechanical vibrations of the ^{4}He-exhaust of the main tank.

Sample-tip drift

To determine the lateral drift $v_{d_{xy}}$ and the vertical drift v_{d_z} of the relative tip and sample position, a pristine InSb(110) surface (see Section 7.1.1 for experimental preparation) was scanned consecutively over a period of 18 hours at the same location in the up and down directions, with each image taking about 1 hour. To exclude the effect of the temporarily decaying thermal drift after cooling down, the series was started 4 days after cooling down the ^{3}He to 400 mK. To avoid the effects of piezo creep after setting a new scanning, the scanning area was scanned 6 hours prior to the evaluated data. Figure 4.6(a) shows a topography

image at the beginning (top part) and at the end (bottom part) of the 18 hour-long series. In the vertical direction, an atomic step and lines of In-atoms from the InSb(110) surface are visible. The two solid lines indicate the position of the step edge for the earlier (green, top) and later (purple, bottom) image. The resulting long term drift appears to be $v_{d_{xy,\mathrm{long}}} = 0.09\text{Å}/\mathrm{h}$. The images of the same scanning direction obtained in this time period show an additional drift behaviour. The drift seems to change its main direction from left to right periodically and is mostly cancelling itself out. On the long time scale of 18 hours, only a net movement $v_{d_{xy,\mathrm{long}}}$ to the right direction remains (cf. Figure 4.6). The short-term drift, taken from two consecutive images of the same scanning direction, is $v_{d_{xy,\mathrm{short}}} = 0.3\text{Å}/\mathrm{h}$. The drift in the z-direction is recorded in the same way, resulting in $v_{d_{z,\mathrm{long}}} = 0.05\text{Å}/\mathrm{h}$ and $v_{d_{z,\mathrm{short}}} = 0.15\text{Å}/\mathrm{h}$, as can be seen in the two line scans shown in Figure 4.6(b). This long-term stability enables experiments above atomically small areas for several hours, without feedback loop or repositioning. It is possible to perform long-term STS fields that span days, without interrupting the experiment to track sample features. Details of the drift and creep behaviour are highly dependent on scanning parameters including speed, area, direction, relative position [72], and only typical values are presented here.

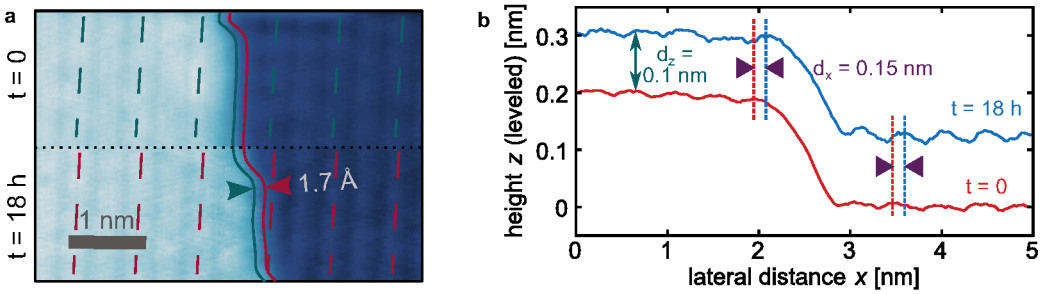

Figure 4.6.: Long term drift $d_{xyz,\mathrm{long}}$ in STM at low temperature – (a) Sections of two STM images ($3.5 \times 5\,\mathrm{nm}^2$) on pristine InSb(110). Recorded at $t = 0$ (top) and at $t = 18\,\mathrm{h}$ (bottom). Teal solid (dashed) line: guide to the eye step edge contour (atomic rows) of the upper frame. Red solid (dashed) line: guide to the eye along the step edge contour (atomic rows) of the lower frame. Arrows indicate the lateral drift after 18 hours. (b) Line scans in x-direction of the same scan coordinates taken 18 hours apart. Lateral shift of the atomic rows by drift indicated by vertical dashed lines and purple arrows. z-drift indicated by vertical arrows (teal). ($V = 300\,\mathrm{mV}$, $I = 30\,\mathrm{pA}$, $t_{\mathrm{line}} = 5\,\mathrm{s}$, $10 \times 10\,\mathrm{nm}^2$, $400 \times 400\,\mathrm{px}$, $B = 0\,\mathrm{T}$, $T = 434\,\mathrm{mK} - 390\,\mathrm{mK}$).

4.2.2. qPlus - STM and AFM combined

With the sample located at the scanner stage, the xy-stage provides five contacts for a sensor. Up to two contacts for the tuning fork electrodes (Figure 4.7(c), VT4 & VT5) and one contact for the tunnelling current (I_t) are needed to read out a qPlus sensor. Besides the common method of contacting the STM tip using a gold wire attached to one prong, we use a second approach that involves sputtering an additional platinum electrode on the top prong [73]. This technique prevents the detrimental influence of the gold wire on the oscillation of the tuning fork. The two spare electrodes on the xy-stage can be used for an excitation of the qPlus sensor. However, the best excitation results are obtained by using piezos located below the xy-coarse piezos (see Figure 3.6(a)). Figure 4.7(a) shows a resonance curve obtained under ambient conditions for a qPlus sensor with a Pt electrode exhibiting a quality factor of $Q = 1800$, and a resonance frequency of $f_0 = 21.8\,\mathrm{kHz}$. Changing the conditions to UHV and low temperatures ($T = 420\,\mathrm{mK}$) drives the Q up to 25000, enhancing the capabilities of the sensor [74, 75, 76]. The amplifier[6] used for the AFM signal is located at the top flange of the insert, at room temperature, and 2 m away from the origin of the oscillation signal. The signal to noise ratio of the resonance curve obtained at low temperatures is promising for future experiments using Δf as a feedback signal.

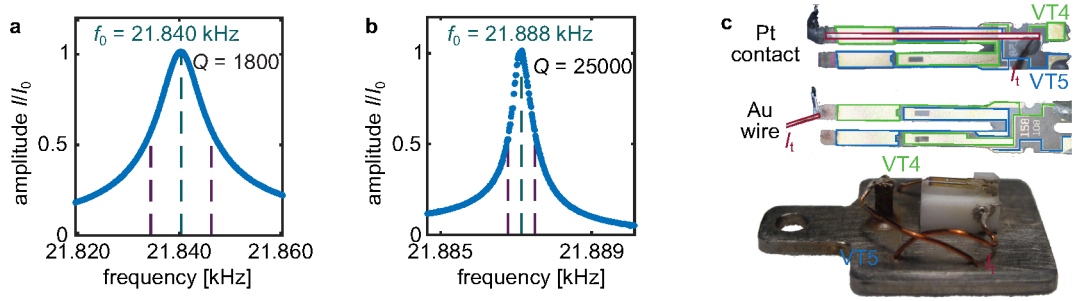

Figure 4.7.: Two versions of qPlus sensor – (a) Resonance curve of a qPlus sensor with vapour-deposited I_t-contact at ambient conditions ($V_{ex} = 148\,\mathrm{mV_{rms}}$, $Q = 1800$). (b) Same qPlus sensor as in (a) but measured in UHV at $T = 420\,\mathrm{mK}$ ($V_{ex} = 100\,\mathrm{mV_{rms}}$, $Q = 25000$). (c) Bottom: qPlus sensor mounted on a sample holder with a gold wire for contacting the tunnelling tip. Contact for the tunnelling current I_t and the tuning fork contacts VT4 & VT5 are marked. Top: two different ways of contacting the tunnelling tip attached to the front of the qPlus sensor. Vapour deposited Platinum contact (red) and gold wire at the front (red). The two electrodes (VT4 and VT5) of the tuning fork are indicated in green and blue. [73]

[6] Femto DLPCA-200.

So far, qPLus topography imaging in this system has only been conducted under ambient conditions. The stiff cantilever and the reduced Q-factor due to air damping and high temperature are difficult conditions for imaging in dynamic mode with a qPlus sensor [77, 78]. Figure 4.8(a) & (b) show a subsequent measurement of the same sample, first using the frequency shift Δf as feedback and then in (b) the tunnelling current I_t. A z-resolution of 1 nm is already possibly in AFM mode. Having access to both signals allows, among other things, a navigation on a non-conducting sample in AFM-mode to find an electrically conductive island on the nm scale (Figure 4.8(c)). Going towards low temperatures and UHV allows the reduction of the oscillation amplitude and the sample-tip distance. This would lead to improved resolution in AFM mode, as well as a higher tunnelling current signal, enabling mapping of the tunnelling current using the AFM feedback and vice versa.

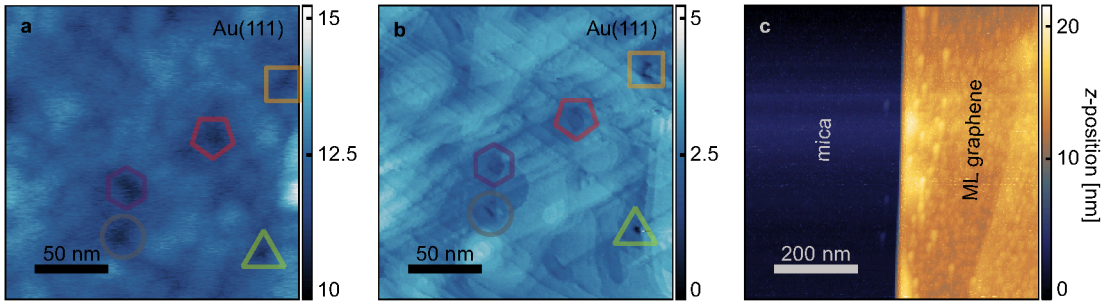

Figure 4.8.: Topography images obtained with a qPlus sensor under ambient conditions – (a) Au(111) surface scanned in AFM-mode using a phase locked loop for constant frequency mode ($\Delta f = -0.7\,\mathrm{Hz}$, $V_{\mathrm{bias}} = 0.5\,\mathrm{V}$, $A_{\mathrm{qPlus}} \approx 5\,\mathrm{nm}$, $200 \times 200\,\mathrm{nm}^2$, $256 \times 256\,\mathrm{px}$, $1\,\mathrm{s/line}$). (b) Same area as in (a) subsequently obtained in STM-mode, coloured markers show same positions in (a) and (b). Tip is about 10 nm closer to the sample relative to the AFM-mode ($I = 0.5\,\mathrm{nA}$, $V_{\mathrm{bias}} = 1\,\mathrm{V}$, $200 \times 200\,\mathrm{nm}^2$, $256 \times 256\,\mathrm{px}$, $1\,\mathrm{s/line}$). (c) Step edge of a non-conducting mica sample surface and an electrically contacted multi-layer graphene sheet (layer thickness: $d_{\mathrm{layer}} = 12\,\mathrm{nm}$, $\Delta f = -0.35\,\mathrm{Hz}$, $V_{\mathrm{bias}} = 0.88\,\mathrm{V}$, $A_{\mathrm{qPlus}} \approx 1.4\,\mathrm{nm}$, $700 \times 700\,\mathrm{nm}^2$, $256 \times 256\,\mathrm{px}$, $5\,\mathrm{s/line}$). [73]

4.2.3. Transport

In addition to performing STM and AFM measurements, the electrical contact arrangement at the scanner and xy-stage exhibits a configuration where magneto-transport, as well as simultaneous STM and transport experiments are possible. With the tip located at the scanner stage, up to five contacts (VT1 to VT5) are available for the sample. The feasibility of such investigations is

shown for a graphene/boron nitride (G/BN) stack[7]. The exfoliated graphene and boron nitride is deposited onto a SiO_2/Si-surface ($d_{SiO_2} = 300\,\text{nm}$), using a dry transfer method [79] (cf. Figure 4.9(a)). A mesh of gold pads, subsequently evaporated onto the sample, for contacting the graphene and allowing an easier orientation on the sample. With the xy-stage and optical access to tip and sample inside the microscope during approach, it is possible to position the tip relative to the sample. Using a long-distance microscope enables a relative position accuracy down to a few µm (Figure 4.9(b)). The tip and tip-reflection, together with the gold pads and trenches, are used to guide an approach to contact pad 'L'.

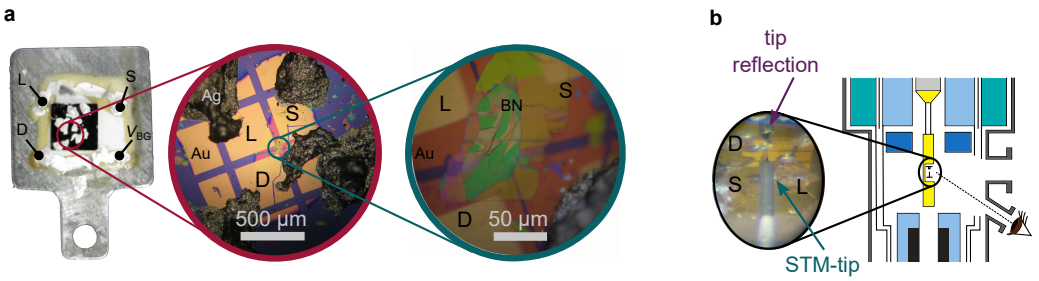

Figure 4.9.: Optical images of a graphene/BN stack sample – (a) Set of optical magnifications of the G/BN. Left to right: sample (black) glued with epoxy on Mo-sample holder. Red ring: enlargement of electrically contacted area. Gold pads (yellow and pink) are contacted with conductive silver. 'L' marks the pad used for tunnelling current (landing), 'S' is the source contact and 'D' the drain contact. Teal ring: second enlargement, the BN layer, lying below the gold contacts, appears green and yellow. At the centre cross, on top of the BN, the graphene flake is located (not visible at this contrast). (b) View towards the sample while positioning the tip on the landing area, using a long-distance microscope. Gold pads and conductive silver can be used to navigate on the sample in order to find the graphene flake. Optical access, as sketched, while the sample is inside the microscope in UHV and at $T \lesssim 25\,\text{K}$.

Figure 4.10(a) shows a sketch of the G/BN stack. A constant source-drain voltage V_{SD} is applied to the graphene flake and the longitudinal resistivity is recorded at various magnetic fields. The electrons in the graphene form a 2DES [80]. With a magnetic field, the quantum Hall effect can be observed [81]. The required Landau level formation is visible in Figure 4.10(b) due to the proportionality of the conductivity to the density of extended states at the Fermi level. Areas where $\mathrm{d}I/\mathrm{d}V$ drops to zero indicate the appearance of quantum Hall phases. Besides the integer filling factors, a plateau in $\mathrm{d}I/\mathrm{d}V_{BG}$ presumably belonging to the fractional filling factor $\nu = -1/3$ is also visible. This fractional

[7] Measurements and sample by Tjorven Johnsen.

quantum Hall effect requires very clean samples, strong electron-electron interaction and strong magnetic fields [82]. The fact that the system allows us to approach an STM-tip to such a nanodevice enables local probing experiments of the complex quantum Hall phases.

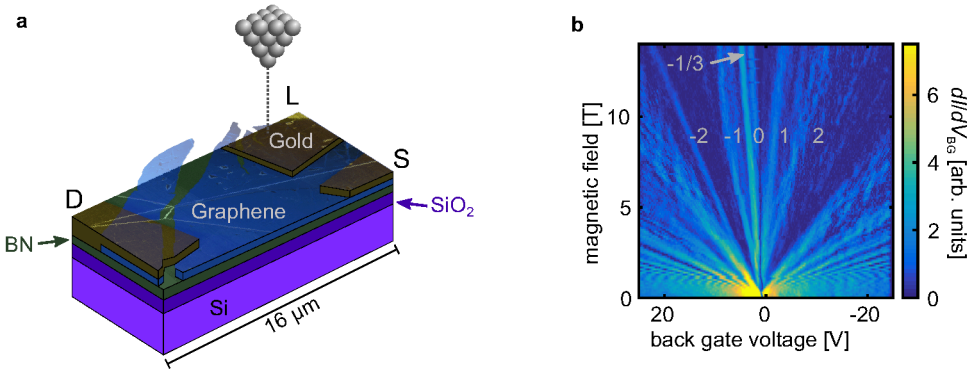

Figure 4.10.: Quantum Hall effect in transport – (a) Sketch of the sample stacking with optical microscope image showing the graphene flake on a BN multilayer, transferred to a SiO_2/Si surface. Subsequent deposition of gold pads. The Si sample is connected with the back gate voltage. Positioning of an STM on the landing area is indicated. (b) Two-point transport measurement of the resistance at various magnetic fields. The z-contrast is the change in conductivity differentiated with respect to the back gate voltage, for improved contrast. Besides the marked integer filling factors, a possible fractional filling factor area is also observable, marked as $\nu = -1/3$ at $V_{BG} = -3.5\,V$, $B = 14\,T$ ($V_{SD} = 100\,\mu V$, $f = 654\,Hz$, $T < 1.6\,K$).

4.3. Electron temperature and energy resolution

A main advantage of performing experimental studies at low temperatures is the higher energy resolution compared to ambient conditions. The energy resolution of electron states in STS experiments is limited by the thermal energy E_T (Equation (2.10)). This means that at room temperature no structures sharper than 80 meV can be resolved. Going down to $T = 400\,mK$ enables energy resolutions down to 0.1 meV. The temperature relevant for the experiment is not necessarily identical with the measured temperature. One reason for this is the spatial separation of the temperature sensor from the position at which the tunnelling event takes place. It is not suitable to put a sensor directly to the STM tip and the sample. Towards low temperatures, also the temperature T_{el} of the electrons taking part in the tunnelling process can differ from the lattice temperature T. In addition to this, voltage noise in the tunnelling path leads to a

smearing of features and an apparently enhanced electron temperature. The performance indicator for a low-temperature experimental setup is therefore the characteristic value T_{el}.

4.3.1. SN-Bandgap

The determination of the energy resolution of the spectroscopy is carried out using a superconducting Nb tip (xy-stage) on a normal conducting W(110) surface (scanner stage). Bulk Nb exhibits a critical temperature of $T_c = 9.2\,\mathrm{K}$ [83] and thus a gap of $\Delta_{\mathrm{Nb,bulk}} = 1.5\,\mathrm{meV}$ [84]. It was surprising that in first trials, operating at $T = 390\,\mathrm{mK}$, this superconducting gap was not observed in STS. Possible reasons for this are an elevated temperature at one or both sides of the junction or electronic noise. The noise that was probed at the insert connectors at the top flange was below $\Delta V_{\mathrm{bias}} = 1\,\mathrm{meV}$. Persistent temperature gradients between the temperature sensor at the microscope body and the tip/sample system of 9 K would either be a result of an insufficient thermal coupling of the wires or of a massive thermal input. Both would result in a reduced holding time at 400 mK, which was not observed. Since both factors are excluded, a noise input, not detectable at the top flange, is the suggested explanation. A high-frequency noise on different wires, e.g. temperature sensors, walker piezos and scanner electrodes, can incorporate this noise into the system and can crosstalk to the tunnelling wires inside the cryostat. The wires of the tunnelling current and bias voltage have a resistance of 150 Ω and a capacity of 400 pF. This is a low-pass filter of about $f_c = 3\,\mathrm{MHz}$. On the one hand, it reduces the noise that can enter from outside into the system. On the other hand, parts of the high-frequency spectrum present at the tunnelling process might not be observable 2 m away at the top flange. Taking this consideration into account, several adjustments were performed. All wiring entering the cryostat is low-pass filtered directly at the top flange with a cutoff frequency of 100 kHz. The walker piezos for approaching tip and sample need a higher cutoff frequency of 3 MHz to preserve the edge steepness necessary in slip-stick operation. Since those piezos are not used during the experiment, a switch is implemented at the top flange to connect the piezo electrodes directly to the grounding potential of the cryostat. All other wiring not needed during the experiment is connected to the ground potential of the cryostat. A resistance below 100 mΩ ensures a sufficient suppression of high-frequency noise.
After those changes at $T = 385\,\mathrm{mK}$, a superconducting gap of the niobium tip, with $\Delta_{\mathrm{Nb,tip}} \approx 0.2\,\mathrm{meV}$, is detectable (Figure 4.11(a)). The observed gap is much smaller than that for bulk niobium. This deviation has been reported previously [40] and can be attributed to the proximity effect, which leads to

different superconducting gaps depending on composition and structure of the tip apex [40, 41]. Since the gap does not open completely at $T = 385\,\mathrm{mK}$, but is clearly present, we can exploit it for a determination of T_{el}.
The sorption pump is heated to increase the sample temperature. This reduces the pumping performance of the sorption pump, the pressure inside the ^{3}He-pot rises and as result the temperature of the microscope rises. The advantage of this indirect heating is that the additional head load takes place at a ^{4}He cooling stage, with marginal influences on the holding time of the ^{3}He cooling. However, the total heat input is higher, due to the larger heat capacity, and the consumption of ^{4}He is enhanced significantly. Furthermore, this indirect heating exhibits a much longer time constant and a slower control of a final temperature.

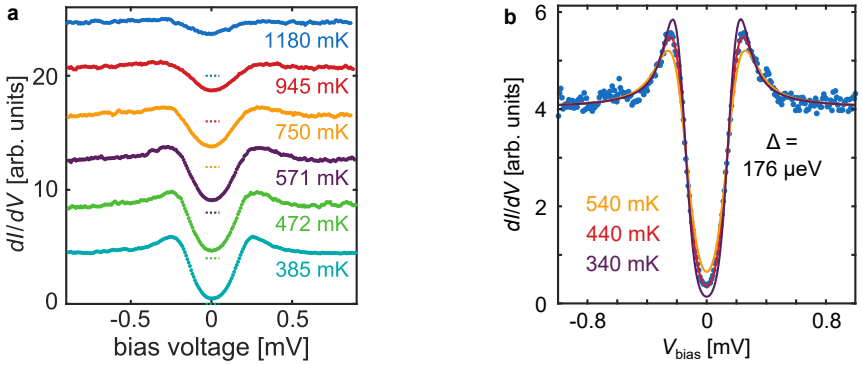

Figure 4.11.: Local STS of superconductor gaps on Nb/W(110) – Spectroscopy data obtained with a niobium tip on a W(110) surface at $B = 0\,\mathrm{T}$. (a) Superconducting gap of niobium with a width of $\Delta = 0.17\,\mathrm{meV}$ at various temperatures. Spectra shifted vertically for clarity. Dashed lines depict zero conductivity. Temperature of the microscope indicated. ($V_{\mathrm{stab}} = 3\,\mathrm{mV}$, $I_{\mathrm{stab}} = 100\,\mathrm{pA}$, $V_{\mathrm{mod}} = 35\,\mu\mathrm{V}$, $f = 643.7\,\mathrm{Hz}$) (b) Fit (red) using Equations (2.9) & (2.11) for data obtained at $T = 393\,\mathrm{mK}$. Fit results: $T_{\mathrm{el}} = 440\,\mathrm{mK} \pm 9\,\mathrm{mK}$, $\Delta = 170\,\mu\mathrm{eV} \pm 2\,\mu\mathrm{eV}$. The yellow (purple) line shows the fitted data with 100 mK increased (reduced) electron temperature.

As expected, the gap shrinks towards higher temperatures. Small changes in temperature highly influence the shape of the gap and the coherence peaks smear out. T_{el} is extracted using Equations (2.9) & (2.11) to fit the data shown in Figure 4.11(b). Free fit parameters are the superconducting gap Δ, T_{el}, as well as the scaling of the $\mathrm{d}I/\mathrm{d}V$. The electron temperature $T_{\mathrm{el}} = 440\,\mathrm{mK} \pm 9\,\mathrm{mK}$ ($\Delta = 0.17\,\mathrm{meV}$) at the xy-stage (where the superconducting tip is located) is slightly elevated compared to the microscope body temperature of $T = 393\,\mathrm{mK}$ (cf. Figure 4.11(b)). The $\pm 100\,\mathrm{mK}$ deviations (yellow and red line) show the high sensitivity of this small gap regarding the temperature. The deviation of

T_{el} from T can be due to residual voltage noise within the tunnelling path or a remaining difference between T at the temperature measurement position and the temperature of the tunnelling junction. An upper estimation of former noise is shown using a superconductor-superconductor tunnelling in Section 4.3.3.

4.3.2. SdH-Oscillations

Additional electrodes at the xy-stage allow magneto-transport experiments. Thus, T_{el} of the xy-stage can also be determined by the temperature dependent changes of the Shubnikov-de Haas oscillations (SdH) [85]. Figure 4.12(a) shows magnetic field sweeps of the longitudinal resistance in 2DES of a GaAs/AlGaAs heterostructure. At $B = 2.2\,\mathrm{T}$ splitting of the different spin directions starts to be resolvable and the evolving minimum corresponds to filling factor $\nu = 5$. Towards higher T, the minimum is smeared out and the valley exhibits a higher resistance. At sufficiently high temperatures the electron can be thermally excited to other edge channels. The longitudinal resistance is then given by

$$\rho_{xx}(T) = \rho_0 e^{\Delta E/2k_B T}, \tag{4.1}$$

with ΔE the energy gap towards an edge channel. For temperatures lower than $T = 4\,\mathrm{K}$, the thermal activation energy becomes small and variable range hopping can be more dominant, giving

$$\rho_{xx}(T) \propto e^{\sqrt{T_0/T}}, \tag{4.2}$$

where the temperature T_0 is inversely proportional to the localisation length of the system [85, 86, 87]. In a double logarithmic plot of $\rho_{xx}(1/T)$ this will give an approximate linear dependency (cf. Figure 4.12(b)).
This linear behaviour is well reflected by the data $T > 500\,\mathrm{mK}$. Extending a linear fit for those data towards lower temperatures reveals a deviation towards higher temperatures T_{el} for $T = 393\,\mathrm{mK}$. Discrepancies of a linear slope in a double logarithmic plot and Equation (4.2) would give a bending of the curve towards lower resistances, which is not observed in this experiment. Thus, the resistances obtained at $T = 393\,\mathrm{mK}$ would amount to $T_{el} = 430\,\mathrm{mK}$. This difference cannot only be explained by the energy resolution of this experiment. At $\nu = 5$ the AC voltage drop in the sample is $V_{AC}(2.2\,\mathrm{T}) = 20\,\mu\mathrm{V}$. This bias modulation together with an experimental temperature of $T = 393\,\mathrm{mK}$ would yield an effective electron temperature of $T_{el} = \sqrt{T^2 + (2.5/3.3 \cdot e/k_B V_{AC})^2} = 431\,\mathrm{mK}$. Thus, no temperature elevation between the xy-stage and the microscope body can be found in the transport measurement and the achievable energy resolution is $\Delta E = 0.12\,\mathrm{meV}$.

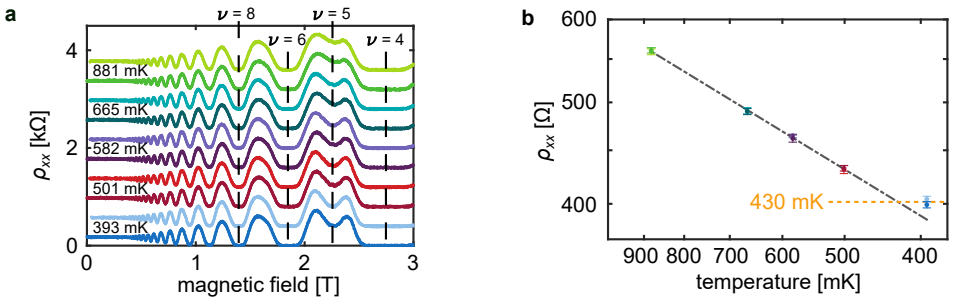

Figure 4.12.: Shubnikov-de Haas oscillations in a GaAs/AlGaAs 2DES – (a) Trace (darker colours) and retrace (lighter colours) of magnetic sweeps for the longitudinal resistance ρ_{xx} of a GaAs/AlGaAs Hall-bar, taken at various temperatures. Offset of 200 Ω between sweeps for clarity. Filling factors ν are indicated. (b) Inverse temperature dependence of valley resistance located at $\nu = 5$ in (a) in a double logarithmic plot. Dashed dotted line: linear regression for resistances belonging to $\nu = 5$, obtained at $T > 500$ mK. Dotted line: mean value of resistance at $\nu = 5$ for $T = 393$ mK. Crossing gives $T_{\mathrm{el}} = 430$ mK. ($V_{\mathrm{SD,DC}} = 10$ mV, $V_{\mathrm{SD,AC}} = 500$ µV, $B = 0\,\mathrm{T} - 3\,\mathrm{T}$)

4.3.3. SS-transition

An investigation of superconductor-superconductor tunnelling (SS) is used to estimate the energy resolution without the broadening effect of the electron temperature. Several multilayers of lead are evaporated on a clean W(110) surface under UHV conditions, which is subsequently transferred in-situ into the microscope, where it is cooled down to $T = 400$ mK. Pb as bulk exhibits a gap $\Delta_{\mathrm{Pb,bulk}} = 1.4$ meV and a critical temperature of $T_c = 9.16$ K. For thin layers and small islands, the gap width can change [88, 89], which does not affect the determination of the energy resolution. Using the Nb tip (same tip as in Section 4.3.1) initially a wide single gap can be observed (Figure 4.13(a)). By the width and structure of the gap an SS transition can be ruled out, so that an SN-transition is present. Due to the wider gap compared to previous measurements on a non-superconducting sample surface, this SN junction is presumably normally conducting at the tip and superconducting at the sample (deposited lead). This provides the possibility to evaluate T_{el} with the superconductor located at the scanner stage. The observed gap ($\Delta = 1.3$ K) exhibits approximately the gap of bulk Pb and shrinks towards higher temperatures. The smearing of the coherence peaks is already noticeable for a slight heating up to $T = 650$ mK. The gap itself does not even close at $T = 2$ K due to the fact that the gap is much larger than the achievable resolution. Fitting of the single gap, as in Section 4.3.1, gives $T_{\mathrm{el}} = 520\,\mathrm{mK} \pm 20\,\mathrm{mK}$ (Figure 4.13(b)). T_{el} for the scanner stage is elevated in comparison to the microscope body temperature of $T = 393$ mK

and higher than at the xy-stage. Using the same fit parameters but varying the electron temperature (yellow and purple lines) shows the temperature dependence of the gap shape. Those deviations, only resolvable in the two zooms of Figure 4.13(b), are smaller than for the small gap of Nb on W(110). The deviation of the scanner and xy-stage cannot be clarified definitively, but can be either real due to thermal coupling or an artefact caused by the smaller temperature dependence of the wider gap.

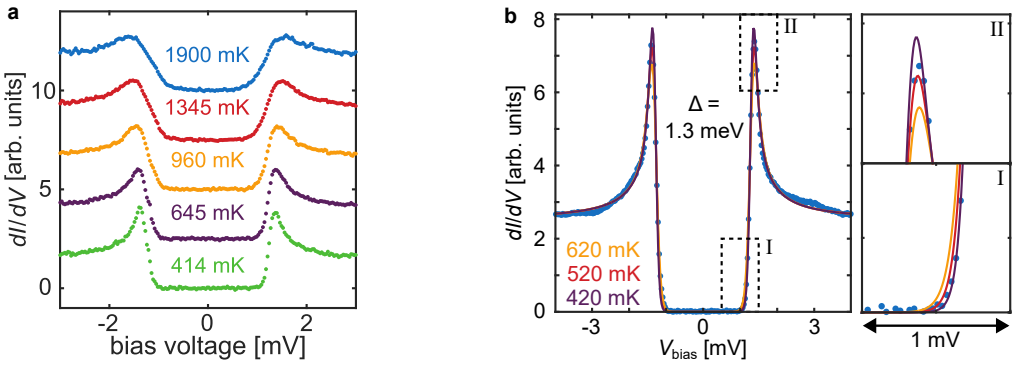

Figure 4.13.: Local STS of superconductor gaps on Pb/W(110) – Spectroscopy data obtained at $B = 0\,\mathrm{T}$. (a) Superconducting gap of lead with a width of $\Delta = 1.3\,\mathrm{meV}$ at various temperatures. Spectra shifted vertically for clarity. Temperature of the microscope indicated. ($V_{\mathrm{stab}} = 4\,\mathrm{mV}$, $I_{\mathrm{stab}} = 100\,\mathrm{pA}$, $V_{\mathrm{mod}} = 20\,\mu\mathrm{V}$, $f = 643.7\,\mathrm{Hz}$) (b) Fit (red) using Equations (2.9) & (2.11) for data obtained at $T = 393\,\mathrm{mK}$ ($V_{\mathrm{mod}} = 35\,\mu\mathrm{V}$). Fit results: $T_{\mathrm{el}} = 520\,\mathrm{mK} \pm 20\,\mathrm{mK}$, $\Delta = 1.30\,\mathrm{meV} \pm 0.01\,\mathrm{meV}$. The yellow (purple) line shows the fitted data with 100 mK increased (reduced) electron temperature. (I) & (II) show enlargements of the boundary of the gap and coherence peaks, depicting the minor changes in shape by varying T_{el}

To achieve SS-tunnelling, the STM tip is immersed into the Pb layers and for low tunnelling currents (high tunnelling resistances) a double gap can be observed in STS (cf. Figure 4.14(a)). The outer coherence peaks can be identified by the sum of the two single gaps of tip and sample (both Pb $\Delta_{1,2} \approx 1.3\,\mathrm{meV}$) and the smaller inner peaks, inside the gap, are due to first order Andreev reflections at $\Delta_1 \approx \Delta_2$ [46]. For the two superconductors, only one peak for the Andreev reflections is observable, which can be explained by the nearly identical gaps of tip and sample. An additional peak at $E = (\Delta_1 + \Delta_2)/3$ is not visible, as it is a 2$^{\mathrm{nd}}$ order effect and thus presumably too small to be observed. Reducing the tunnelling barrier, by increasing the stabilisation current to $I_{\mathrm{stab}} = 20\,\mathrm{nA}$, leads to the development of a peak located at the Fermi energy, inside the superconducting gap.

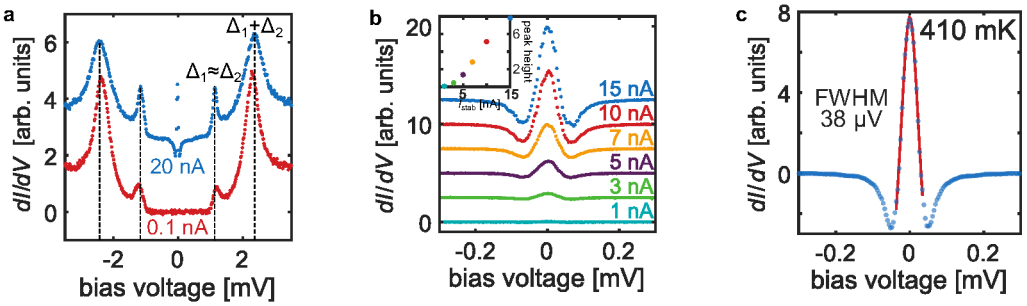

Figure 4.14.: STS of a superconducting tip (Pb) on a superconducting surface (Pb/W(110)) – (a) Tunnelling spectra obtained at two different stabilisation currents. For lower tunnelling resistances the peak from Josephson tunnelling appears at E_F. Two sets of coherence peaks appear (dashed lines as guide to the eye), referring to the sum of tip and sample gap ($\Delta_1 + \Delta_2$) and the Andreev reflection resulting in a peak at $\Delta_1 \approx \Delta_2$. (b) Set of STS of the Josephson peak for different I_{stab}. Inset: the peak height rises superlinearly with the reduction of the tunnelling barrier. (c) Josephson peak obtained for $I_{stab} = 20\,\mathrm{nA}$, width not limited by $3.3k_BT$. Red: Lorentzian fit of the Josephson peak ($V_{stab} = 4\,\mathrm{mV}$, $V_{mod} = 9\,\mu\mathrm{V}$, $f = 643.7\,\mathrm{Hz}$, $T = 410\,\mathrm{mK}$).

This peak is the so-called Josephson peak (JP), caused by direct Cooper pair tunnelling. This assignment of the peak is corroborated by the observation of the Andreev reflections in an SS-junction. Fitting a Lorentzian curve to the sharp JP (see Figure 4.14(c)) shows a FWHM of $38\,\mu\mathrm{V}$, narrower than $3k_BT$ at $T = 391\,\mathrm{mK}$. The voltage dependence of the Josephson current and thus the peak width can also be limited by the Josephson coupling energy (Equation (2.12)) or by the charging energy E_C. Thus, only an upper boundary of the voltage noise can be deduced from the width of the JP, which is of σ-width $\Delta V_{bias} = 16\,\mu\mathrm{V}$. The bandwidth, scaling with E_C, is given by the capacitance and the resistance of the tunnelling junction [50]. The observability of the JP allows us to estimate the charging energy to $E_C \lesssim E_T$. With $T = 400\,\mathrm{mK}$ and a tunnelling barrier of $R = 0.2\,\mathrm{M\Omega}$, the maximal bandwidth of the bias noise detection results in $f_{Bw} = 1/2\pi RC \gtrsim 100\,\mathrm{MHz}$. Thus, the bandwidth of the noise determination is not limited by the Josephson tunnelling process, but the setup bandwidth of 700 Hz.

Part II.

Quantum Hall Measurements on Cs/p-InSb(110)

5. The local Rashba effect

The manifold of spintronic devices that have been proposed are based on the tuning of spin-orbit coupling, in particular using the so-called Rashba spin-orbit coupling. In spintronic devices the Rashba effect is used to manipulate the spin orientation, which has been demonstrated experimentally [90, 6, 91]. Possible devices are the Datta-Das spin transistor [3], the realisation of which is the subject of present research [90, 6, 10, 11]. A different approach for a spin transistor is given by balancing the Rashba and the Dresselhaus effect to form a so-called spin-helix [92, 93, 4, 8]. Further possible applications based on the Rashba effect are spin filters [5] or quantum computing using the Majorana states in nanowires [9, 7].
Systems in which the spin degeneracy is lifted, are systems with broken inversion or time-reversal symmetry. The latter can be realised by applying a magnetic field, resulting in Zeeman splitting

$$E_{\text{Zeeman}} = g\mu_{\text{B}}B \tag{5.1}$$

with $\mu_{\text{B}} = e\hbar/(2m_{\text{e}})$ the Bohr magneton, electron mass m_{e}, Landé-factor g and the magnetic field B. In the bulk zinc blende structure no inversion centre exists. Spin degeneracy is broken by bulk inversion asymmetry, the so-called Dresselhaus effect [94, 95]. In two-dimensional structures and one-dimensional structures, a structure inversion asymmetry (SIA) leads to the so-called Rashba spin splitting [96, 97].

5.1. Rashba effect

An electron that is propagating with the velocity $\boldsymbol{v}$ perpendicular to an electric field E experiences a magnetic field $\boldsymbol{B}_{\text{eff}} = 1/c\,\boldsymbol{v} \times \boldsymbol{E}$. Every electron will experience a resulting magnetic field, which depends on its direction of motion and strength of $\boldsymbol{E}$. The Hamilton operator describing the spin-orbit coupling in atomic physics can be derived from the Dirac equation by a non-relativistic

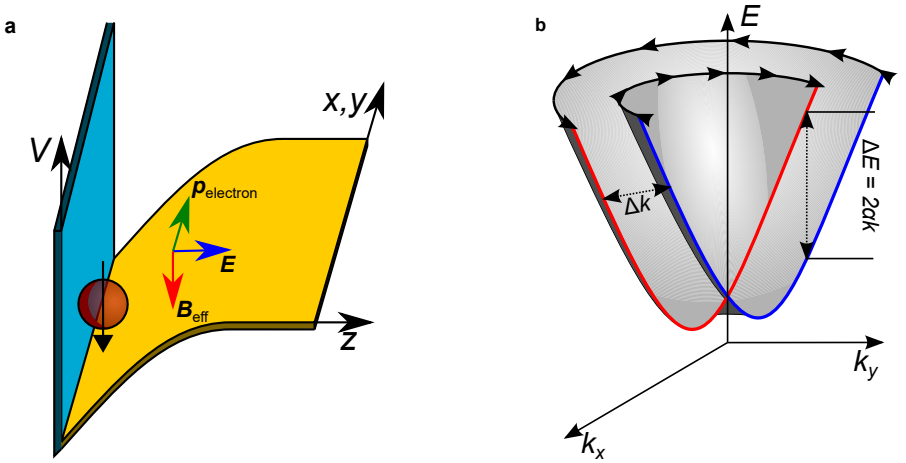

Figure 5.1.: (a) Structure inversion asymmetry: 2DES at surfaces or interfaces often exhibit an electric field $\boldsymbol{E}$ perpendicular to the electron (red sphere) motion v, resulting in an effective magnetic field $\boldsymbol{B}_{\text{eff}}$. (b) A cut through the split parabola of the 2DES dispersion relation which exhibits a Rashba effect. The $\boldsymbol{k}$ dependent spin direction leads to differing directions of rotation of the spin (black arrows) for the inner and outer branch. The two parabolas (red & blue) exhibit opposing spin directions.

approximation. The full Hamiltonian [98] of the Pauli equation is given by

$$\mathcal{H} = \frac{p^2}{2m_0} + V \quad + \underbrace{\frac{e\hbar}{2m_0}\boldsymbol{\sigma}\cdot\boldsymbol{B}}_{\mathcal{H}_{\text{Zeeman}}} - \underbrace{\frac{e\hbar\,\boldsymbol{\sigma}\cdot\boldsymbol{p}\times\boldsymbol{E}}{4m_0^2c^2}}_{\mathcal{H}_{\text{SO}}} - \underbrace{\frac{e\hbar^2}{8m_0^2c^2}\nabla\cdot\boldsymbol{E}}_{\mathcal{H}_{\text{Darwin}}} \tag{5.2}$$

$$- \quad \frac{p^4}{8m_0^3c^2} - \frac{e\hbar p^2}{4m_0^3c^2}\boldsymbol{\sigma}\cdot\boldsymbol{B} - \frac{(e\hbar B)^2}{8m_0^3c^2}, \tag{5.3}$$

with the momentum operator $\boldsymbol{p}$, the electrostatic potential V and the Pauli spin matrices $\boldsymbol{\sigma}$. The last three terms are higher order corrections of the kinetic and Zeeman term.
By using a constant electric field E_z in z-direction, the spin-orbit Hamiltonian $\mathcal{H}_{\text{SO}}$ can be simplified to

$$\mathcal{H}_{\text{SO}} = \frac{\alpha_{\text{R}}}{\hbar}\boldsymbol{\sigma}\cdot\boldsymbol{p}\times e_z, \tag{5.4}$$

with α_{R} Rashba parameter, which represents the strength of the spin-orbit coupling. Semiconductor systems show SIA at interfaces and surfaces. Figure 5.1(a) shows a 2DES which is formed at the surface by bending the conduction band downwards. Here an electric field points into the surface and is perpendicular to the 2DES. In a crystalline solid, we can write the Hamiltonian with the wave vector $\boldsymbol{k} = \boldsymbol{p}/\hbar$. The Hamiltonian with kinetic, electrostatic and the spin-orbit

contribution, reads

$$\mathcal{H} = \frac{\hbar^2 \boldsymbol{k}^2}{2m} + eV + \alpha_{\mathrm{R}} \left(k_y \sigma_x - k_x \sigma_y \right), \tag{5.5}$$

with an effective electron mass m^*. The mixing of k_y, σ_x and k_x, σ_y, respectively, leads to a lifting of the spin degeneracy. For a hole system, this situation changes and the spin splitting is no longer linear in k [98], such systems are out of the scope of this work. The resulting eigenvalues for electron systems and small k are given by

$$E = \frac{\hbar^2 \boldsymbol{k}^2}{2m^*} \pm \alpha_{\mathrm{R}} |k| + eV, \tag{5.6}$$

and represent the energy levels of the two spin directions, while the spin direction is in-plane. The dispersion relation (5.6) is plotted in Figure 5.1(b). Two spin branches are formed, originating from the parabola of a 2DES without spin-orbit coupling. The spin direction of each branch is locked perpendicularly to the momentum and the spin of the inner branch is inverted with respect to the spin direction of the outer branch. As a result of the electron momentum, the spin changes its orientation with $\boldsymbol{k}$. At $k = 0$ the two spin directions are degenerate, reflecting that those electrons see no effective magnetic field [98, 99].

5.2. Rashba effect in magnetic field

By applying a perpendicular magnetic field B to a 2DES, the electron motion is quantised in Landau levels (LL). Classically the electrons are forced on a circular path and precess with the cyclotron frequency $\omega_c = eB/m^*$ around its centre. The LL wave function is often described in literature using the approach of Girvin and Jach [100], excluding any LL mixing and projecting states on the lowest LL. To describe a system exhibiting potential disorder and LL mixing, we use in this work the approach developed by Champel and Florens describing the wave functions using vortices [101, 102]. In the presence of a perpendicular magnetic field and without disorder, the eigenenergies are the same as for the harmonic oscillator, but the components of the kinetic momenta do not commute [98]. In the symmetric gauge the electron motion $\boldsymbol{r} = (x, y)$ in a 2D plane can be described as a cyclotron motion with guiding centre position $\boldsymbol{R} = (X, Y)$ and cyclotron coordinate $\boldsymbol{r} - \boldsymbol{R}$. The wave functions can be written as

$$\Psi_{n,\boldsymbol{R}}(\boldsymbol{r}) = \frac{1}{\sqrt{2\pi l_B^2 n!}} \left(\frac{z - Z}{\sqrt{(2)} l_B} \right)^n \exp\left(-\frac{|z|^2 + |Z|^2 - 2Zz^*}{4l_B^2} \right) \tag{5.7}$$

with $n = 0, 1, 2, ...$ as Landau quantum number, $z = x + i \cdot y$ and $Z = X + i \cdot Y$. l_B denotes the magnetic length given by

$$l_B = \sqrt{\frac{\hbar}{|e|B}}, \tag{5.8}$$

which describes the different quantum cyclotron radii $R_n = \sqrt{2n+1} l_B$ received from the Bohr-Sommerfeld quantisation. Including the electron spin the LL energies are additionally split by the Zeeman energy (Equation (5.1)) and in an effective mass approximation of a single band , i.e. for a parabolic band, the LL eigenenergies (Figure 5.2(a)) are given by

$$E_{n,\sigma} = \hbar\omega_c \left(n + 1/2\right) + \frac{g^*}{2}\sigma\mu_B B, \tag{5.9}$$

with $\sigma = \pm 1$ the spin quantum number [103, 98].

5.2.1. Landau levels with spin-orbit interaction

If a Rashba effect is present in the 2DES, the behaviour changes. Here, the spin splitting has a contribution from the Zeeman and the Rashba effect. While the external magnetic field $\boldsymbol{B}$ is oriented perpendicular to the 2DES, the effective magnetic field from the Rashba effect varies with $\boldsymbol{k}$. The Rashba effect leads to a mixing of the two spin directions parallel to $\boldsymbol{B}$. The spin is therefore not a good quantum number and the system is described by a new set of quantum numbers n and $\lambda = \pm 1$, which describes the two different spin channels, each containing contribution of the n^{th} and $(n-1)^{\text{th}}$ LL, as well as both spin directions. According to the Bychkov-Rashba model [96] the energy levels are described by

$$\varepsilon_{n,\lambda}(\boldsymbol{R}) = \hbar\omega_c \left(n - \frac{\lambda}{2}\sqrt{\left(1 - Z(\boldsymbol{R})\right)^2 + nS(\boldsymbol{R})^2}\right) \tag{5.10}$$

with

$$S(\boldsymbol{R}) = \frac{2\sqrt{2}\alpha_{\text{R}}(\boldsymbol{R})}{\hbar\omega_c l_B} \tag{5.11}$$

as the contribution of the spin-orbit coupling, determined by the strength of the Rashba effect with respect to the external magnetic field and the contribution of the Zeeman splitting

$$Z(\boldsymbol{R}) \quad = \quad \frac{g^*(\boldsymbol{R})m^*(\boldsymbol{R})}{2m_{\text{e}}}. \tag{5.12}$$

For $n = 0$ only the spin channel $\lambda = -1$ exists.
For zero magnetic field, (5.10) transforms into (5.6), the eigenenergies of pure Rashba coupling. For large magnetic fields the Zeeman contribution dominates and we receive the eigenenergies of the LL without a Rasha effect (5.9).

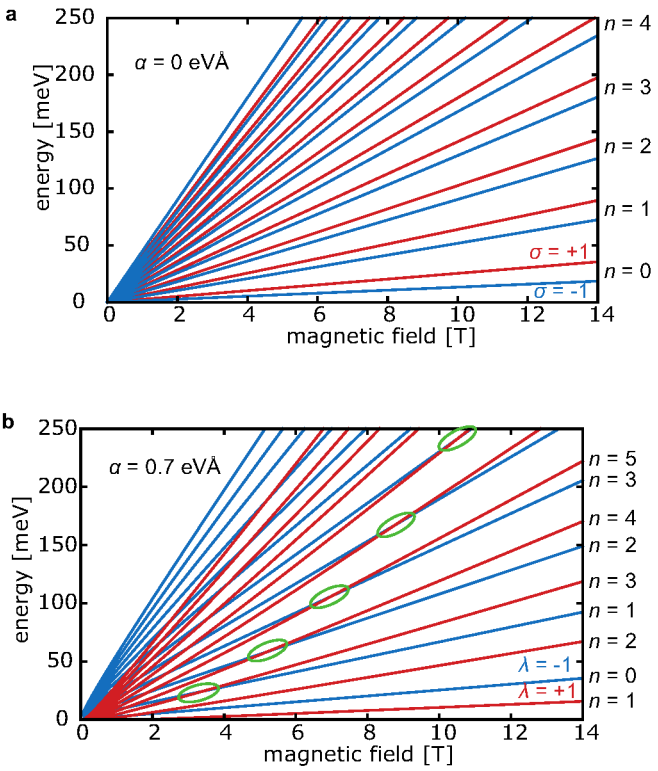

Figure 5.2.: Landau level evolution in a magnetic field – (a) Without and (b) with Rashba effect for $m^* = 0.03 \cdot m_e$, $g^* = -21$ and $n = 0..11$. The different spin channels are coloured red and blue. Crossings of the energy levels are indicated (green ellipses).

Figure 5.2 shows the spin-split LLs for $n = 0, 1..11$. In contradiction with the LL splitting in the absence of the Rashba effect (Figure 5.2(a)), crossings of levels of opposite spin channels appear (green ellipses). Additionally, a non-linearity at low magnetic fields occurs. The splitting of the lowest Landau level LL_0, $\Delta E_{SS} = \varepsilon_{0,-} - \varepsilon_{1,+}$, is shown in Figure 5.3 for different Rashba parameters ($\alpha_R = 0, 1, 1.5\,\text{eVÅ}$). It exhibits a non-linearity for $B < 3\,\text{T}$, which leads to an effective offset of the linear dependency found for larger B. Thus, this offset can be used as an approximation for the determination of α_R. A Taylor expansion of Equation (5.10) for large magnetic fields (small S) results in the expression

$$\Delta E^0_{SS}(B \to 0) = \frac{4\alpha_R^2 m^*}{\hbar^2 \left(2 - \frac{g m^*}{m_e}\right)} \tag{5.13}$$

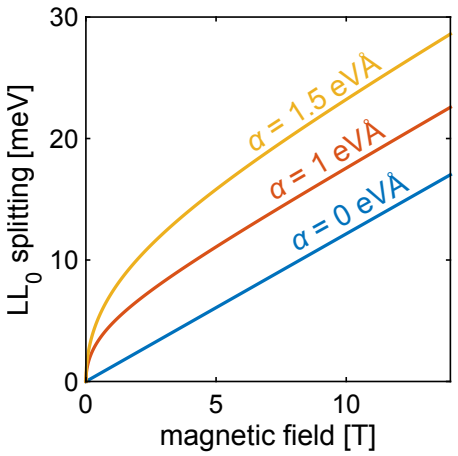

Figure 5.3.: LL_0-splitting for different Rashba parameters – Splitting of the lowest two energy levels from (5.10) shown in Figure 5.2 for different α_R. $m^* = 0.03 \cdot m_e$, $g^* = -21$.

leading to an offset of the linear B dependence towards $B = 0$, which depends quadratically on α_R and transfers into $\Delta E^0_{SS} = 0$ if no Rashba effect is present. For an extraction of α_R knowledge of m^* and g^* is crucial and will be discussed in Section 7.2.
The positions of the crossings of $\varepsilon_{n,\lambda}(B)$, indicated in Figure 5.2 by green ellipses, also depend on α_R, but turn out to be inapplicable for the determination of α_R. While in Figure 5.2 the effective mass is assumed to be constant, it actually changes depending on the distance from the conduction band minimum in the triagonal-well potential approximation. Thus, the LL splitting changes towards higher energies and the crossing positions change. Another reason for discrepancies is the presence of the potential disorder, which had been neglected so far. While the potential itself does not affect the spin splitting, neither Zeeman nor Rashba, a disordered potential has a varying influence on the orbital components of the LL wave functions and, hence, on their energy changing with B, respectively, on $\varepsilon_{n,\lambda}(B)$.

5.2.2. Wave function

Without the Rashba effect, taking the spin into account, the LL wave function of LL_n can be written as the spinor

$$\tilde{\Psi}_n(\boldsymbol{r}) = \begin{pmatrix} \Psi_{n,+1}(\boldsymbol{r}) \\ \Psi_{n,-1}(\boldsymbol{r}) \end{pmatrix} = \sum_\sigma \Psi_{n,\sigma}(\boldsymbol{r}) \otimes |\sigma\rangle \tag{5.14}$$

with the two spin directions $\sigma = \pm 1$, the spatial part of the wave function $\Psi_{n,\sigma}(\boldsymbol{r})$ tensor multiplied with the spin state $|\sigma\rangle$.

As mentioned in the previous section, the presence of the Rashba effect leads to a mixing of the two spin channels. The new spinor contains a spin-dependent LL quantum number $n_\sigma = n - (1+\sigma)/2$, thus

$$n_\sigma = \begin{cases} n-1 & \sigma = +1 \\ n & \sigma = -1. \end{cases} \tag{5.15}$$

The strength of the mixing depends on the ratio between Rashba effect and Zeeman effect, i.e. the angle of the relative contribution of the external magnetic field and the internal magnetic field due to the Rashba effect. The mixing angle is given by

$$\theta_n^\lambda = \arctan\left[\frac{(1-Z) + \lambda\sqrt{(1-Z)^2 + nS^2}}{S\sqrt{n}}\right]. \tag{5.16}$$

With this the wave function reads

$$\tilde{\Psi}_{n,\boldsymbol{R},\lambda}(\boldsymbol{r}) = [\sin(\theta_\lambda^n)\,\Psi_{n-1,\boldsymbol{R}}(\boldsymbol{r}) + \cos(\theta_\lambda^n)\,\Psi_{n,\boldsymbol{R}}(\boldsymbol{r})] \otimes |\sigma\rangle\,, \tag{5.17}$$

with $\lambda = \pm 1$ as new spin quantum number. Here it can be seen that in the new coordinates of n and λ the former spin channels σ, and LL_n & LL_{n-1} are mixing with the angle θ_λ^n which mainly depends on the strength of α_R and the external magnetic field B. This effect of the LL-mixing will be incorporated for smooth potential disorder in Section 5.3.1.

5.3. Rashba effect in disorder potential

5.3.1. LL in disorder potential

An analytic approach to describe the LL splitting in a smooth disorder potential $V(\boldsymbol{R})$, where $l_B|\nabla V(\boldsymbol{R})|/\hbar\omega_c \ll 1$, has been performed by Hernangómez-Pérez et al. [102] considering a mixing of the different orbitals (5.17) and neglecting the scattering between different LL_n. Equation (5.10) is modified by a 2D disorder potential $V_{\mathrm{2D}}(\boldsymbol{R})$ and the energy levels $\epsilon_{n,\lambda}$ described in this first order perturbation theory in $l_B|\nabla V(\boldsymbol{R})|/\hbar\omega_c$ become

$$\epsilon_{n,\lambda}(\boldsymbol{R}) = \hbar\omega_c \left(n - \frac{\lambda}{2}\sqrt{\left(1 - Z + \frac{V_{\mathrm{2D},n}(\boldsymbol{R}) - V_{\mathrm{2D},n-1}(\boldsymbol{R})}{\hbar\omega_c}\right)^2 + nS^2} \right) + \frac{V_{\mathrm{2D},n-1}(\boldsymbol{R}) + V_{\mathrm{2D},n}(\boldsymbol{R})}{2}, \tag{5.18}$$

with

$$V_{\mathrm{2D},n}(\boldsymbol{R}) = \iint V_{\mathrm{2D}}(\boldsymbol{R}+\boldsymbol{r}) \cdot F_n(\boldsymbol{r})\, \mathrm{d}^2\boldsymbol{r}. \tag{5.19}$$

The terms $V_{\mathrm{2D},n}(\boldsymbol{R})$ denote the effective potential which is a convolution of the potential $V_{\mathrm{2D}}(\boldsymbol{R})$ and the kernel $F_n(\boldsymbol{r})$ of the n^{th} LL wave function (Equation (5.7))

$$F_n(\boldsymbol{r}-\boldsymbol{R}) = \exp\left(-\frac{l_B^2}{4}\Delta_{\boldsymbol{R}}\right)|\Psi_{n,\boldsymbol{R}}(\boldsymbol{r})|^2, \tag{5.20}$$

$$= \frac{(-1)^n}{\pi l_B^2} L_n\left[\frac{2(\boldsymbol{r}-\boldsymbol{R})^2}{l_B^2}\right] \exp\left(\frac{-(\boldsymbol{r}-\boldsymbol{R})^2}{l_B^2}\right), \tag{5.21}$$

with $L_n(z)$ as the Laguerre polynomial of degree n, and $\Delta_{\boldsymbol{R}}$ as the Laplacian with respect to $\boldsymbol{R}$. Here, $F_{-1}(\boldsymbol{r}-\boldsymbol{R}) \equiv 0$. This kernel does not directly translate to the wave function probability density and can become negative. It rather corresponds to a Wigner transformation [104, 105]. For a flat potential, $V_{\mathrm{2D}}(\boldsymbol{R}) = \text{const.}$, the effective potentials become identical, $V_{\mathrm{2D},n}(\boldsymbol{R}) = V_{\mathrm{2D},m}(\boldsymbol{R})$ for all n, m. With this, Equation (5.18) transforms to Equation (5.10) with an irrelevant offset potential of $V_{\mathrm{2D},n}(\boldsymbol{R})$. In Equation (5.18), the effective potential appears with two contributions. On the one hand as a sum, which is considering that the n^{th}-wave function exhibits contributions of the classical n^{th} and $(n-1)^{\mathrm{th}}$ LL and thus the energy levels have an offset from the average effective potential. On the other hand, a difference appears in the square root, connected to the Zeeman term. The contributions of the two different spin channels, by

the mixing of the n^{th} and $(n-1)^{\text{th}}$ wave function, lead to an effective change of the Zeeman splitting, since both contributions can add up differently for the two spin channels.

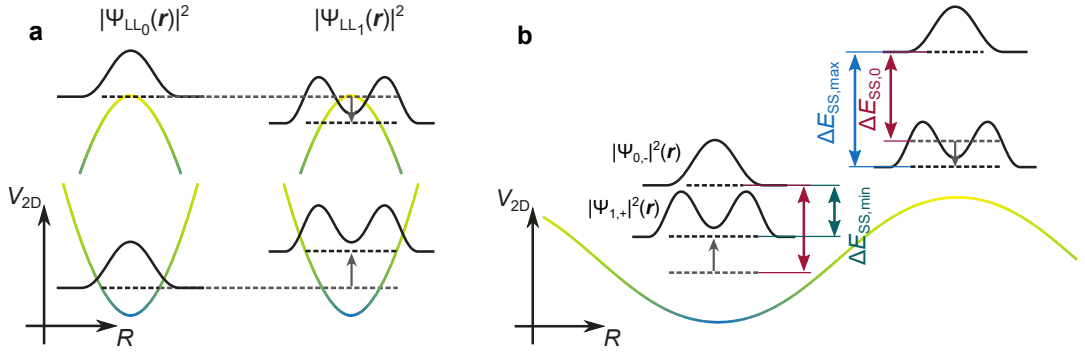

Figure 5.4.: Energy shift of $\varepsilon_{n,\lambda}$ by potential disorder – (a) Relative energy shift of the LL_0 & LL_1 wave functions at a potential minimum (bottom) and maximum (top). Gray arrow indicates change in energy due to larger spatial extension. (b) System with a strong mixing of LL_0 & LL_1: change of spin splitting $\Delta E_{SS,0}$ due to the spatial extent of the corresponding LL wave functions, thus, $E_{SS,min} < E_{SS,max}$.

The aforementioned considerations apply strongly at local extremes of the potential disorder. The spatial extension of the Landau levels increases with n and decreases with magnetic field ($l_B \propto \sqrt{1/B}$) (cf. Figure 5.4(a)). In a potential minimum, higher LLs are shifted towards higher effective potential energies compared to lower LLs. At a potential maximum this situation is inverted. The LLs with higher n are shifted towards lower energies.
In systems exhibiting the Rashba effect, the wave functions related to the lowest level $\varepsilon_{1,+}$ consists of contributions from LL_0 and LL_1, while the next higher, $\varepsilon_{0,-}$, only exhibits LL_0 contributions. Therefore, the lower energy level $\varepsilon_{1,+}$ raises in energy at potential minima, leading to a decrease of ΔE_{SS}. In contrast, at potential maxima $\varepsilon_{1,+}$ is shifted down and ΔE_{SS} is enhanced (Figure 5.4(b)). Perez et al. have shown that for smooth disorder this effect is well described by Equation (5.18) and calculated the $\varepsilon_{n,\lambda}$ in a random 1D potential (Figure 5.5(a)), illustrating the effect of contrary change in splitting at potential minima and maxima. In an STS measurement the observable LDOS at the position $\boldsymbol{r}$ is described, neglecting changes in the transmission coefficient $T(E, eV, z)$ (cf. Equation (2.6)), by

$$\rho^{STS}(\boldsymbol{r}, E, T_{\text{el}}) = -\int \rho_{\text{t}}(\epsilon)\rho_{\text{s}}(\boldsymbol{r}, \epsilon) n'_{\text{F}}(\epsilon) \mathrm{d}\epsilon, \tag{5.22}$$

with the derivative of the Fermi-Dirac distribution given by

$$n'_{\text{F}}(\epsilon) = -\frac{1}{4k_{\text{B}}T_{\text{el}}} \frac{1}{\cosh^2\left[(\epsilon - E_{\text{F}})/2k_{\text{B}}T_{\text{el}}\right]}, \tag{5.23}$$

ρ_t the DOS of the tip and ρ_s the LDOS of the sample. For the presented model the spin resolved LDOS of the projected spin, becomes

$$\rho_\sigma^{STS} = -\frac{1}{4\pi l_B^2} \int \sum_{n=0}^{+\infty} \sum_{\lambda} n'_F\left(\varepsilon_{n,\lambda}(\boldsymbol{R})\right) \times F_{n_\sigma}(\boldsymbol{r}-\boldsymbol{R}) \left[1 - \lambda\sigma \sqrt{1 - \frac{nS^2(\boldsymbol{R})}{\sqrt{(1-Z(\boldsymbol{R}))^2 + nS(\boldsymbol{R})^2}}}\right] \mathrm{d}^2\boldsymbol{R}, \quad (5.24)$$

with n_σ being the reduced n (Equation (5.15)).
Figure 5.5(b) shows the calculated LDOS, as it would be seen in STS for the positions marked in Figure 5.5(a) considering $\boldsymbol{R} \simeq \boldsymbol{r}$ [102]. Besides the differing ΔE_{SS} at potential minimum and maximum, the spin splitting appears to be unobservable around regions of larger gradients. Experimental observations of this effect will be presented in this work. The limits for this approach are regions with a strong curvature, where 2nd-order contributions can become important. In the system investigated in this thesis the mixing angle is $\theta_1^+ = 70\,^\circ$ thus a small contribution of the higher LL ($\cos(\theta_+^1) = 0.35$) is present and the effect on the splitting $\varepsilon_{0,-} - \varepsilon_{1,+}$ is expected to be small.

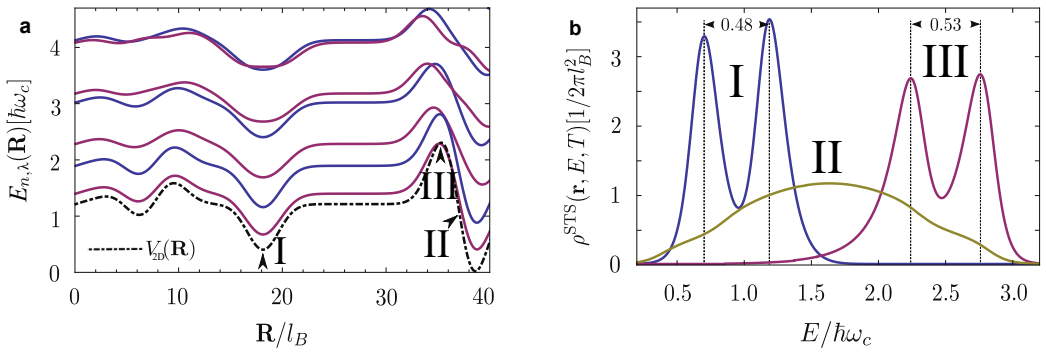

Figure 5.5.: Calculations of LL positions in a 1D disorder potential with constant α_R, g^*, m^* – (a) Energy dispersion of a 1D potential called $V_{2D}(\boldsymbol{R})$ (dashed dotted line) as a function of the vortex position $\boldsymbol{R}$. The solid lines show the LL given by Equation (5.18). They are influenced by the 1D effective potential ($V_{2D,n}$ in Equation (5.18)). I, II, III mark a potential minimum, an area of largest potential gradient and a maximum position, respectively. (b) Simulated LDOS around $\varepsilon_{0,-}$ & $\varepsilon_{1,+}$, using Equation (5.24), at those positions. The spin splitting ΔE_{SS} can only be resolved at potential minima and maxima. As shown in Figure 5.4(b) maxima exhibit splitting enhancement compared to minima ($B = 7\,\mathrm{T}$, $S = 0.88$, $T = 15\,\mathrm{K}$). Both adapted from [102].

5.3.2. Fluctuations of the SO coupling due to random charge distribution

Besides the above-described effects, changes in the spin-orbit coupling also affect the energy splitting. The strength of the spin-orbit coupling α_R, as a direct result of the electric field, varies with changes of the electric field. Glazov et al. [16] analyse the variations of the spin-orbit coupling in a single quantum well due to randomness in doping layers, and consequent changes in the electric fields. Assuming a symmetric system, with a 2DES lying between two doping layers of width w_d and distance R_d from the quantum well (Figure 5.6(a)), there is in average no electric field at the position of the quantum well. Therefore, no average Rashba field is present and $\overline{\alpha_R} = 0$. The SIA is still broken by the random distribution of the dopants, resulting in a locally varying Rashba parameter $\alpha_R(\boldsymbol{R}) \neq 0$.

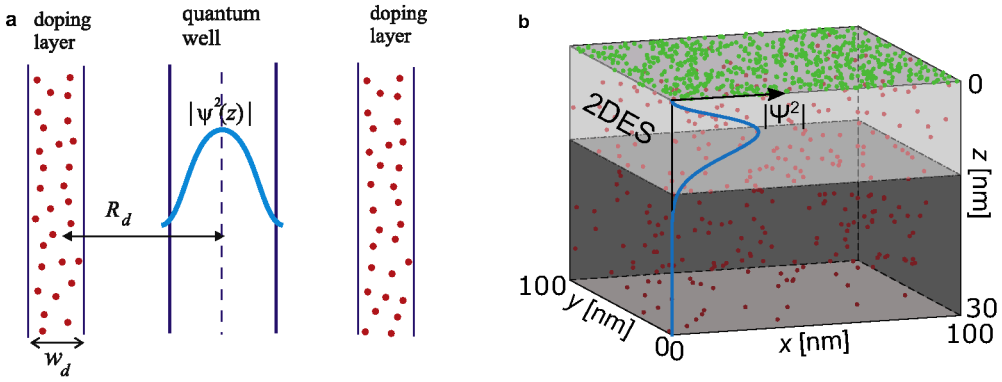

Figure 5.6.: Random electric field in a quantum well and a 2DES by random charge distributions – (a) Quantum well between two distant doping layers. The randomly distributed dopants (red) lead to a varying electric field inside the quantum well. (b) 2DES (yellow) induced in InSb by surface adsorbed Cs (green dots), $n_{Cs} = 6 \cdot 10^{18}\,\mathrm{m}^{-2}$. p-doping of the bulk with Ge (red), $n_{Ge} = 1 \cdot 10^{24}\,\mathrm{m}^{-3}$. The black line indicates the electron probability distribution of the 2DES in z-direction, assuming a constant electric field.

For very thin doping layers $w_d \ll R_d$ the scale of the random fluctuation of the electric field is given by

$$\Delta\mathcal{E}_r = \sqrt{2\pi}\frac{|e|}{\epsilon_0\epsilon_r}\frac{\sqrt{n_{2D}}}{R_d}. \tag{5.25}$$

In an InSb semiconductor with $\epsilon_r = \epsilon_{r,InSb} = 16.8$ [106] as dielectric constant, a distance to the quantum well of $R_d = 10\,\mathrm{nm}$ and a two-dimensional dopant concentration of $n_{2D} = 10^{16}\,\mathrm{m}^2$ (white noise - δ-shaped charges), the fluctuations of the electric field can be expected to be $\Delta\mathcal{E}_r \approx 3 \cdot 10^7\,\frac{\mathrm{V}}{\mathrm{m}}$ which is in

the same order as the average electric field experimentally found for an InSb system exhibiting a 2DES at the surface [107].

As we describe in [17], the 2DES investigated in this thesis is induced by adsorbates acting as n-type dopants on a p-doped bulk semiconductor (Figure 5.6(b)). As this system shows SIA, an average electric field is present and two different doping layers lead to variations in the electric field. The 2D distribution of the Cesium surface charges with mean density $\overline{n_{2D}}$ is described by the 2D coordinates $\boldsymbol{R}$, and the 3D distributed Germanium bulk donors with a mean density $\overline{n_{3D}}$ are described by coordinates $\boldsymbol{R}'$. Both charging types are treated as uncorrelated and are represented as δ-functions. At positions $\boldsymbol{\rho}$ those charges lead to an electric field $E_z(\boldsymbol{\rho})$ perpendicular to the surface

$$E_z(\boldsymbol{\rho}) = \frac{e}{\epsilon_0 \epsilon_{\mathrm{r,InSb}}} \cdot \left[2 \int n_{2D}(\boldsymbol{R}) - \frac{\boldsymbol{\rho} - \boldsymbol{R}}{|\boldsymbol{\rho} - \boldsymbol{R}|^3} \mathrm{d}^2\boldsymbol{R} - \int n_{3D}(\boldsymbol{R}') - \frac{\boldsymbol{\rho} - \boldsymbol{R}'}{|\boldsymbol{\rho} - \boldsymbol{R}'|^3} \mathrm{d}^3\boldsymbol{R}' \right]_z \tag{5.26}$$

The 2 in front of the 2D integral takes into account that for surface dopants one half space is InSb and the other is vacuum. Autocorrelating the electric field after weighing it with the electron probability distribution

$$|\Psi|^2 = \frac{b^3}{2} \cdot z^2 e^{-bz}, \tag{5.27}$$

with $b = 0.4\,\mathrm{nm}^{-1}$ gives the variance of the Rashba parameter resulting from the 2D and 3D charges

$$\left\langle (\delta\alpha_{\mathrm{R,2D}})^2 \right\rangle^{1/2} = \frac{2e^2\xi}{\epsilon_{\mathrm{r,InSb}}} \times b \left(\frac{\pi}{10} \bar{n}_{2D} \right)^{1/2}, \tag{5.28}$$

$$\left\langle (\delta\alpha_{\mathrm{R,3D}})^2 \right\rangle^{1/2} = \frac{e^2\xi}{\epsilon_{\mathrm{r,InSb}}} \times \left(\frac{\pi}{2} \bar{n}_{3D} b \right)^{1/2}. \tag{5.29}$$

Using $\xi = 526\text{Å}^2$ [98] as coupling constant between electric field and Rashba parameter in InSb, as well as $\bar{n}_{2D} = 6 \times 10^{16}\,\mathrm{m}^{-2}$ and $\bar{n}_{3D} = 10^{24}\,\mathrm{m}^{-3}$, the expected fluctuations of the Rashba parameter are $\delta\alpha_{\mathrm{R,2D}} \approx \delta\alpha_{\mathrm{R,3D}} \approx 0.25\,\mathrm{eVÅ}$ due to the surface and bulk doping. Besides the amplitude, the length scale on which those variations occur is interesting for applications such as spin transport. By evaluating the two correlation functions of the Rashba parameter

$$\langle \delta\alpha_{\mathrm{R,2D}}(\boldsymbol{0}) \delta\alpha_{\mathrm{R,2D}}(\boldsymbol{R}) \rangle = \left\langle (\delta\alpha_{\mathrm{R,2D}})^2 \right\rangle F_{2D}(R), \tag{5.30}$$

$$\langle \delta\alpha_{\mathrm{R,3D}}(\boldsymbol{0}) \delta\alpha_{\mathrm{R,3D}}(\boldsymbol{R}) \rangle = \left\langle (\delta\alpha_{\mathrm{R,3D}})^2 \right\rangle F_{3D}(R), \tag{5.31}$$

we can extract the range functions F_{2D} and F_{3D}, normed on $F(0) = 1$, and thereby calculate the correlation length, defined as

$$L^2_{2D,3D} = \int_0^\infty F_{2D,3D}(R) R \mathrm{d}R. \tag{5.32}$$

For the two types of dopings this results in

$$L^2_{2D} = \frac{40\pi}{b^2},\ L^2_{3D} = \frac{\pi}{2}\frac{D_l}{b}, \tag{5.33}$$

where D_l describes the depletion layer depth, which is the range of negatively charged p-type dopants. While L_{2D} only depends on the width of the electron density distribution $|\Psi^2|$, the electric field of the bulk donors also has a depletion layer depth dependency. The correlation length of the variations of the electric field appears to be independent from the strength of the spin-orbit coupling, as well as the dielectric constant.

5.3.3. Spin relaxation

The Rashba effect itself, described by the Hamiltonian in Equation (5.4), leads to a spin precession. This spin precession is reversible and rotates all spins in a predictable fashion. Scattering at impurities, phonons or electron-electron interaction can lead to dephasing of the spins and thus to spin relaxation. In the case of the D'yakonov-Perel' (DP) mechanism [14, 108] spin dephasing occurs between scattering events (Figure 5.7(a)). Scattering leads to a change of the momentum $\boldsymbol{k}$. As the effective magnetic field seen by the electron changes with $\boldsymbol{k}$, the spin precession rate $\Omega(\boldsymbol{k})$ depends on $\boldsymbol{k}$, too. For small momentum scattering times τ, so that $\Omega(\boldsymbol{k})\tau \ll 1$, the spin relaxation rate Γ_S is given by

$$\Gamma_S = 2\Omega(\boldsymbol{k})^2 \hbar \tau. \tag{5.34}$$

In systems with structure inversion symmetry, the Elliott-Yafet (EY) mechanism [15, 109, 108] can be present. Here, the spin is flipped during the scattering event itself. The probability of a spin-flip (Figure 5.7(b)) at a scattering event is given by the ratio of the mixing of the spin up and down state described by the matrix element L between coupling bands and their energy distance Δ. The probability $p_{\text{flip}} = (L/\Delta)^2$ of a spin-flip at a scattering event gives

$$\Gamma_S = \left(\frac{L}{\Delta}\right)^2 \frac{\hbar}{2\tau}. \tag{5.35}$$

for spin relaxation by EY. DP and EY are therefore typically distinguished by their opposite dependence on momentum scattering time τ, hence, on mobility

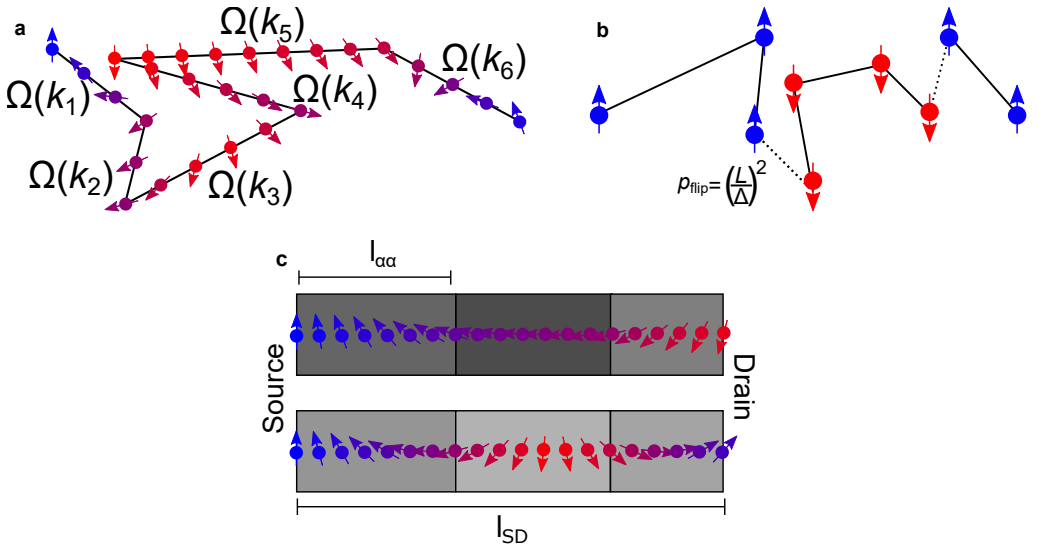

Figure 5.7.: Mechanisms of spin diffusion – (a) DP mechanism: the spin precesses around the effective magnetic field, which is due to the Rashba effect. Scattering leads to a change of $\boldsymbol{k}$ and thus a change in precession orientation, direction and speed. (b) EY mechanism: rare spin-flip events while scattering. Probability of spin-flip is proportional to the mixing of the spin up and spin down state [108]. (c) Spin dephasing by random Rashba fluctuations. Two ballistic transport paths, probing different strengths of spin-orbit coupling (Dark grey - small α_R, light grey - large α_R).

$\mu = e^2\tau/m^*$.
Both mechanisms can be avoided by realising ballistic transport, i.e. $\tau = \infty$. The EY vanishes, because no spin-flips occur. For the DP mechanism the spin precesses only at $\Omega(\boldsymbol{k})$ which results in a predictable, fixed phase relation for all electrons. Avoidance of scattering events therefore enhances the spin relaxation length.
Nevertheless, spin dephasing can also be ceased by a locally varying Rashba parameter $\alpha_R(\boldsymbol{R})$. Envision two different transport paths in a 2DES from source to drain passing a locally varying Rashba parameter (Figure 5.7(c)), while the correlation length $l_{\alpha\alpha}$ of $\alpha_R(\boldsymbol{R})$ is much shorter than the transport distance l_{SD}. Following different paths causes the precession of the spin to acquire different phases. Therefore, for a large set of transport paths an effective spin relaxation occurs, even without the presence of scatterers. The length

$$l_{\text{Spin}} = \left(\frac{\hbar^2}{2m^*\delta\alpha_R}\right)^2 \frac{1}{l_{\alpha\alpha}}. \tag{5.36}$$

is the distance that an electron travels on a random path before loosing its spin memory [110].

As mentioned in Chapter 5.3.2, local variations of $\alpha_R(\boldsymbol{R})$ occur due to the distribution of dopants and do not need any scattering events inside the transport layer. The size of the average Rashba parameter $\overline{\alpha_R}$ is also not decisive.

6. Experimental studies of spin-orbit coupling

As the Rashba effect seems to be a promising fundament for applications in spintronics [1, 5, 111, 3, 4] and quantum computing [9, 7], it has been intensively investigated, both theoretically and experimentally. Angle-resolved photo-electron spectroscopy (ARPES) in particular is used to map the dispersion relation of the Rashba-type spin splitting. Besides being utilised in experiments aimed at realising such devices [90, 11, 10, 112] in transport, STM has also been used to gain a fundamental understanding of the Rashba effect.

6.1. Spintronics using the Rashba effect

There are many proposals for a realisation of devices and applications based on the Rashba spin-orbit coupling [1, 5, 111]. The most famous of these is the Datta-Das transistor [3], which was first proposed as early as 1990. It changes the spin precession length $l_{SO} = \pi\hbar^2/m^*\overline{\alpha_R}$ by tuning the strength of the Rashba parameter along the travelling path of polarised electrons. A more recent approach for creating a spin-transistor is the so-called spin helix, which forms in a system of equally strong Rashba and Dresselhaus coupling.

6.1.1. Datta-Das transistor

The design is based on the spin-polarised transport between source and drain through a semiconductor. Engels et al. [113] and Nitta et al. [114] were the first to demonstrate the feasibility of gate controlling the spin-orbit coupling in InGaAs/InP and InGaAs/InAlAs heterostructures, respectively. The beating pattern in the Shubnikov-de Haas oscillation, as a trace of the spin-orbit coupling, is tunable by a gate (cf. Section 6.2.3). The first attempts to realise complete spin transistor devices used ferromagnetic contacts as source and drain, acting as spin filters for injection and detection of the spin current [115, 116, 117, 118]. The spin orientation itself is rotating along the transport direction due to the spin-orbit coupling. By using a Schottky gate on top of the semiconductor,

the strength of the spin-orbit coupling, and thus the spin revolution between source and drain can be adjusted. If the spin orientation of the current is parallel to the spin orientation of the drain, a higher current can be detected than in anti-parallel configuration. By changing the gate voltage, it is possible to switch between the on-state (parallel) and the off-state (anti-parallel) of the transistor.

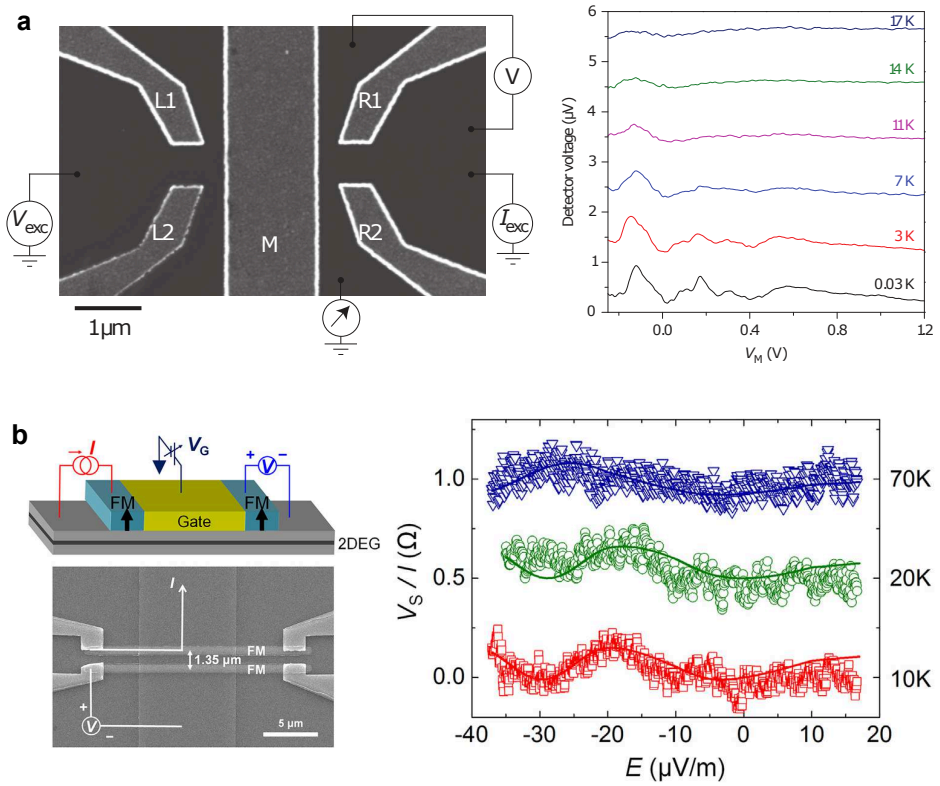

Figure 6.1.: All-electric spin transistors – (a) All-electric all-semiconductor spin transistor by Chuang et al. [11]. Left: SEM image of the spin field-effect transistor. Two pairs of split gates ($L1$-$L2$ & $R1$, $R2$) created by asymmetrically tuning an effective magnetic field for injecting and detecting spins. The gate M tunes the spin-orbit coupling of the spin transport through the device. Right: detector voltage depending on the gate voltage V_M for various temperatures and a fixed conduction value set to $G_{\mathrm{QPC}} = 0.3 \times 2e^2/h$. (b) All-electric spin transistor by Kim et al. [112] which uses the diffusive spins for detection. Left: sketch and SEM image of the experimental device incl. current path and measurement voltage. Spin detection via $Tb_{20}Fe_{62}Co_{18}/Co_{40}Fe_{40}B_{20}$ electrodes. Right: spin voltage as a function of the electric field created by the gate depending on temperature ($B = 0\,\mathrm{T}$).

Recent approaches using ferromagnetic electrodes for injection and detection [90, 112] or the spin Hall effect for detection [10], as well as an all-semiconductor approach [11], show clear signals of a tunable spin polarised current (Figure 6.1

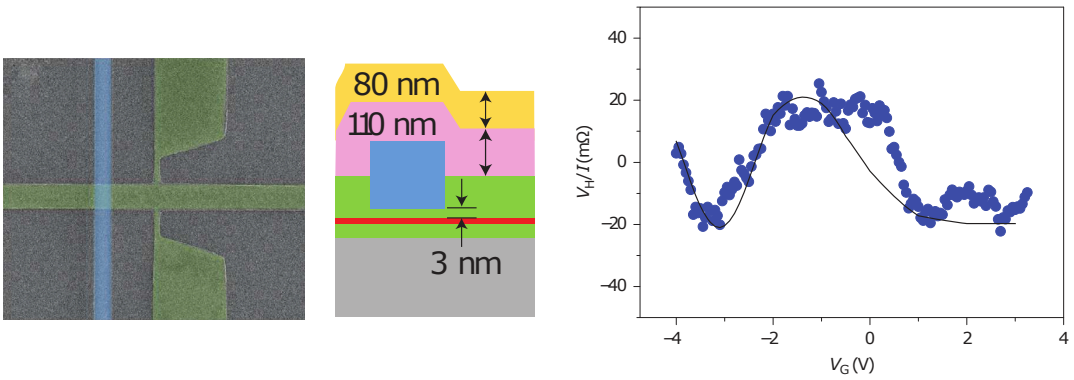

Figure 6.2.: Spin Hall detection spin transistor – Left: SEM image and cross-sectional view of the device. Ferromagnetic injection electrode (blue) on top of the InAs heterostructure with transport channel width $w = 0.75\,\mu\text{m}$ and length $L = 0.9\,\mu\text{m}$ containing the single quantum well (red) with a gate placed on top of the device (yellow). Right: spin transport signal obtained by the spin Hall voltage at the green pads ($T = 1.8\,\text{K}$) [10].

& Figure 6.2). At the same time, these experiments were performed at low temperatures ($T = 0.03\,\text{K} - 77\,\text{K}$) and are very sensitive to an increase of temperature. With the already small signal to noise ratios, no clear signal of a spin polarised current is observed at temperatures above $T = 20\,\text{K}$. Besides different approaches of spin injection and detection to obtain a larger spin polarisation, some samples exhibit ballistic transport (mean free paths up to $l_{\text{MFP}} = 2\,\mu\text{m}$) to avoid a detrimental spin dephasing. Spin dephasing by DP and EY (Equation (5.3.3)) are then avoided, but an influence of a possible variation of the spin-orbit coupling strength has not been considered so far.

6.1.2. Spin-helix

Besides the pursuit of the realisation of a robust Datta-Das transistor by ballistic transport, the spin-helix allows the avoidance of DP spin dephasing in non-ballistic samples [4]. Systems exhibiting the Dresselhaus and Rashba spin-orbit coupling can be described by the Hamiltonian $\mathcal{H} = \hbar^2 \boldsymbol{k}^2/2m + \mathcal{H}_{\text{D}} + \mathcal{H}_{\text{SO}}$, with the Dresselhaus term

$$\mathcal{H}_{\text{D}} = \beta \left(k_x \sigma_x - k_y \sigma_y \right) \tag{6.1}$$

and the Rashba term

$$\mathcal{H}_{\text{SO}} = \alpha_{\text{R}} \left(k_x \sigma_y - k_y \sigma_x \right) . \tag{6.2}$$

Here β is the strength of the Dresselhaus effect. The Dresselhaus effect also contains a cubic term which has been neglected for the sake of simplicity [119,

120]. In a 2DES the eigenstates corresponding to $\mathcal{H}$ are given by

$$\Psi_{\pm,k}(\boldsymbol{R}) = \frac{1}{\sqrt{2}} \begin{pmatrix} 1 \\ \pm e^{i\phi(\boldsymbol{k})} \end{pmatrix} \frac{e^{i\boldsymbol{k}\boldsymbol{R}}}{2\pi}, \tag{6.3}$$

with the $\boldsymbol{k}$ dependence of the spinor being exclusive to the phase factor of the wave function

$$\phi(\boldsymbol{k}) = \arg\left[-\alpha k_y + \beta k_x + i\left(\alpha k_x - \beta k_y\right)\right]. \tag{6.4}$$

and the eigenvalues

$$\varepsilon(\boldsymbol{k}) = \frac{\hbar \boldsymbol{k}^2}{2m} \pm \sqrt{\left(\alpha k_y - \beta k_x\right)^2 + \left(\alpha k_x - \beta k_y\right)^2}. \tag{6.5}$$

For the case that $\alpha = \beta$, i.e. that the Dresselhaus coupling has the same strength as the Rashba coupling, the eigenenergy follows a parabolic dispersion relation. Furthermore, $\phi(\boldsymbol{k})$ becomes constant, and the spin state becomes independent of the direction of $\boldsymbol{k}$. This is called a persistent spin helix (PSH). It is robust against non-magnetic scattering, prohibiting DP-type spin relaxation. The spin orientation precesses independent of the individual electron path, unaffected by scattering events [4, 121]. The spin can still relax due to magnetic scattering and the cubic Dresselhaus term after non-magnetic scattering. This leads to two Dresselhaus parameters β_1(linear) and β_3(cubic). A spin helix is realised for $\alpha = |\beta_1 - \beta_3|$ [92, 122].
Experimentally, the PSH could be realised [6, 122, 91, 93]. In spintronic devices the spin helix state can refer to the on-state, and a detuning of the Rashba and Dresselhaus parameter, thereby destroying the PSH, would represent the off-state. Wunderlich et al. [6] show maps of a PSH obtained by magneto optic Kerr microscopy. Electrons in a GaAs/AlGaAs quantum well are pumped by circularly polarised light into the conduction band. With the time-delayed probe pulse, the spin polarisation in z-direction is measured via the polar magneto-optical Kerr effect. Besides the direct mapping of the PSH, the Rashba parameter, the linear and the cubic Dresselhaus parameter are estimated by analysing the decay of the PSH. The spatial variation of the Rashba parameter is not taken into account. It would result in a spatial detuning of the PSH and in turn, reduce the PSH life-time.
Table 6.1 shows the deduced spin dephasing l_{Spin} length and the corresponding spin diffusion length

$$l_{\text{S}} = \sqrt{\frac{l_{\text{Spin}} l_{\text{MFP}}}{2}}, \tag{6.6}$$

based on a spin dephasing by a variating Rashba parameter given by Equation (5.36) & Equation (5.33) for a set of prospect spintronics applications [8, 10,

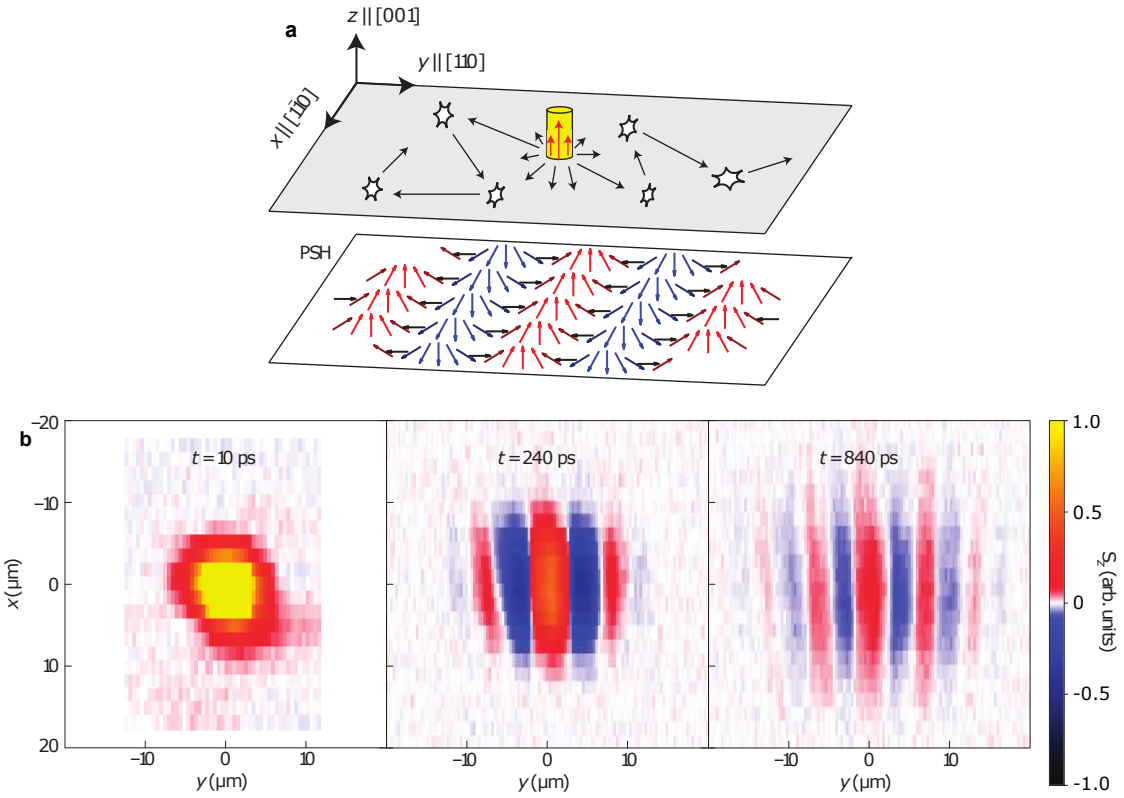

Figure 6.3.: Persistent spin helix (PSH) – (a) Top: scheme of the diffusive expansion of an excited spin. Bottom: resulting PSH. Arrows indicate direction of spin polarisation. (b) Kerr rotation microscopy maps obtained at three different times after initial excitation of spin polarised electrons at $\tau = 0$ ($T = 40\,\mathrm{K}$). Adapted from [6].

11]. The numbers are estimations, mostly since ξ is a material and structure dependent parameter [123]. The parameter ξ can easily vary up to a factor of 4. As l_{Spin} depends quadratically on ξ, the given numbers are only order of magnitude estimates. Moreover, variations of α_{R} are estimated to originate from the remote dopant layers. Additional origins of disorder in the electric field, increasing the variations on α_{R} further, are not considered. Equation (5.36) is only valid for $l_{\mathrm{SO}} \gg l_{\alpha\alpha}$, which is not correct for the device in [11]. However, the estimated spin dephasing length l_S reproduces the observed reduction length of the spin signal, which is about 2 µm in [8], quite well. In the device of Chuang et al. [11], the spin signal is reduced by 20 % after a single rotation. This suggests a spin diffusion length of about 10 µm. The remaining Rashba parameter $\alpha_{\mathrm{R}} = 0.003\,\mathrm{eV\AA}$ Faniel et al. [8] found in their device is strikingly close to the estimated $\left\langle (\delta\alpha_{R,QW}) \right\rangle^{1/2}$. This remaining Rashba parameter had been explained using higher order terms of the Dresselhaus coupling, but an explanation using

Rashba disorder is more straightforward. This indicates that the fluctuation of the Rashba parameter might already be placing limitations on the performance of actual devices.

Table 6.1.: Calculated effect of Rashba parameter fluctuations on spintronic devices - Rashba parameter fluctuations $\langle(\delta\alpha_{R,QW})\rangle^{1/2}$, correlation length of these fluctuations $L_{\alpha_R\alpha_R}$, spin dephasing length l_{Spin} and diffusion length l_S for 2DES studied in [8, 10, 11]. Input parameters taken from the references, unless marked differently. The electron mean free path l_{MFP} is deduced from the mobility.

2DES	$\overline{n}_{2D}$ [m^{-2}]	R_d [nm]	ϵ_r	m^* [m_e]	ξ [Å^2]	$\overline{\alpha_R}$ [eVÅ]	$\langle(\delta\alpha_{R,QW})\rangle^{1/2}$ [eVÅ]	$l_{\alpha\alpha}$ [nm]	l_{Spin} [µm]	l_{MFP} [µm]	l_S [µm]
InAs [10]	$2\cdot10^{16}$	15	14	0.03	125 [98]	0.09	0.01	80	23	1.3	4
InGaAs [11]	$2\cdot10^{15}$	80	14	0.04	125 [98]	0.01 – 0.08	0.001	450	(500)[1]	1.7	(20)[1]
InGaAs [8]	$2\cdot10^{16}$	10	14	0.04	30	0.015 – 0.1	0.005	60	60	0.5	4

6.2. Rashba effect in STM/STS

To get access to the band structure at the surface, one can look at the quasi particle interference pattern (QPI) which forms, for instance, around vacancies, impurities and step edges [18]. The tunnelling current in STM is proportional to the probability density wave function $|\Psi|^2$. The Bloch states probed locally by the STM lead to a uniform distribution, in addition to the atomic corrugation. If scattering occurs at defects, states of different $\boldsymbol{k}$ at the same energy mix. The result is a standing wave pattern with wave vector $\boldsymbol{q} = \boldsymbol{k_0} - \boldsymbol{k_1}$. The wavelength of the standing wave pattern $\lambda = 2\pi/q$ can be used to deduce the energy dispersion relation at the surface.
Nevertheless, Petersen and Hedegård [124] have shown that the two Rashba bands do not lead to a distinct QPI pattern, since opposite spins cannot interfere with each other. Moreover, only impurities that break the time-reversal symmetry can induce scattering between two opposite spin channels. The two intraband scattering vectors for backscattering have the same length leading to standing wave pattern with identical wavelength. The scattering vector $\boldsymbol{q}$ can only be translated directly into the wave vector $\boldsymbol{k} = \boldsymbol{q}/2$ of the dispersion relation if the band is symmetric around Γ. Any shift along $k-$space cannot be probed. Therefore, in STM the spin splitting of the Rashba bands is not directly visible via QPI.

[1] Values for l_{Spin} and l_S are only valid for $L_{\alpha_R\alpha_R} \gg l_{SO}$, but in [11] $l_{SO} \approx 700 - 2000\,\mathrm{nm}$.

6.2.1. Quasi-particle-interference pattern

However, for some systems it is still possible to extract the Rashba spin splitting using the QPI in STM if additional bands are involved in scattering [125, 126, 127]. The surface alloy $BiCu_2/Cu(111)$ exhibits two types of surface states. The first, showing a Rashba spin splitting, is of sp_z-type (Figure 6.4(g)) - red and blue) and the second, showing no breaking of spin degeneracy, is of $p_{xy}-$type (black). The QPI, obtained by STS (Figure 6.4(a)-(e)), and the related Fourier transform (FT) show wavelengths related to several scattering processes. In the radial averaged FT (Figure 6.4(f)) we can see the scattering processes q_1 - intraband scattering between the spin split parabolic sp_z Rashba bands (blue), q_2 - intraband scattering of the spin degenerate surface state exhibiting p_{xy} character (red) and q_{12} - interband scattering between the spin degenerate surface state and the spin split states (green). The absence of scattering processes between the p_{xy} band and the outer Rashba band presumably results from a reduced orbital overlap [125, 128, 129]. Forward scattering processes between p_{xy} band and Rashba band are too short in q_{12} to be distinguished from topographic features. Since q_2 describes scattering of a band symmetric around Γ, the wave vector $\boldsymbol{k}_2$ of the energy dispersion can be extracted. The spin split parabolas can also be extracted. The curvature is accessible by the scattering process q_1. The distance of the Rashba bands from the degenerate band can then be derived from the scattering processes q_2 and q_{12} (Figure 6.4(h)).
Au(111) exhibits only a single surface state, such that no additional interband scattering processes can be used to determine the Rashba spin splitting. Leicht et. al [126] added a graphene layer to the Au(111) surface to add an additional surface band, and extracted the Rashba spin splitting of the Au(111) surface state. With two different tunnelling tip configurations, scattering features from graphene and from gold can be distinguished. The QPI of the $\mathrm{d}I/\mathrm{d}V$ image in Figure 6.5(a) was obtained in a configuration only sensitive to graphene. The ring at the centre of the FFT (Γ) corresponds to the intravalley backscattering and the ring structures at the corners of the hexagonal Brillouin zone (BZ) originate from intervalley scattering $\boldsymbol{q}_{\mathrm{G,inter}} = \overline{\Gamma\mathrm{K}} - 2\boldsymbol{k}_{\mathrm{G}}$ between K and K$'$ (Figure 6.5(c)).
In a second tip configuration (Figure 6.5(b)), a larger ring at Γ becomes visible and at the edges of the BZ two additional ring structures appear. The feature in the centre reflects the backscattering within the Au(111) surface state. This tip is therefore sensitive to the underlying gold surface. Even though the Au-surface state undergoes Rashba-type spin splitting, only one ring appears with $\boldsymbol{q}_{\mathrm{Au}} = \boldsymbol{k}_{\mathrm{Au,1}} - \boldsymbol{k}_{\mathrm{Au,2}}$. The two additional features at the boundary of the BZ originate from scattering between each spin split Au parabola and the graphene

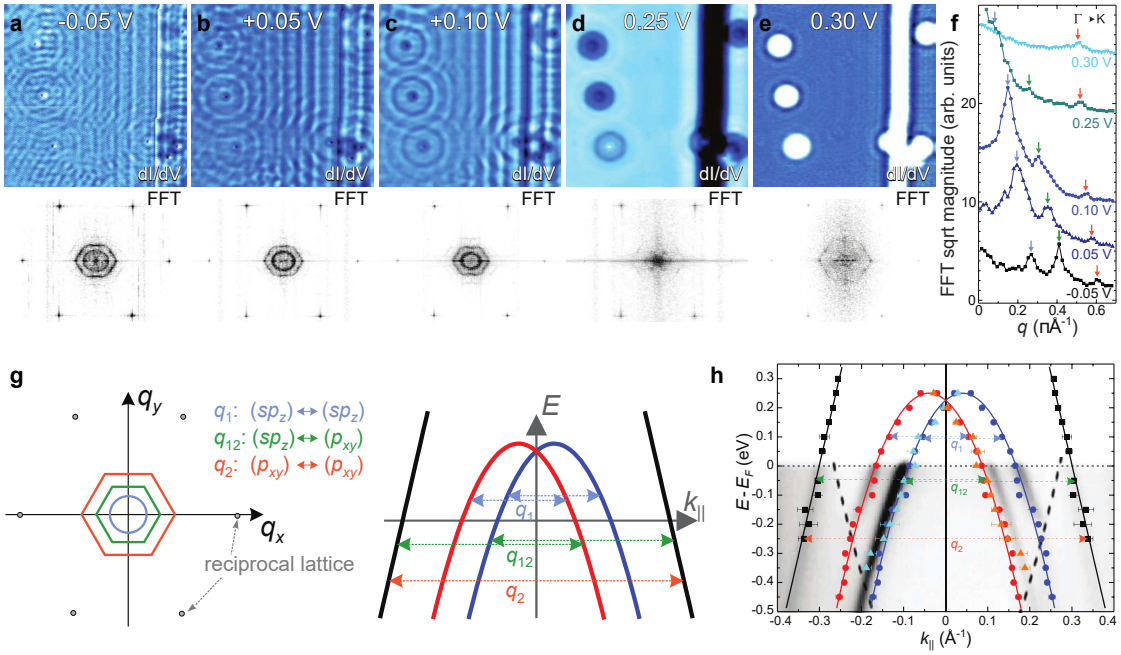

Figure 6.4.: STS of Rashba splitting in $BiCu_2$/Cu(111) – (a)-(e) Top: dI/dV images of a $BiCu_2$/Cu(111) obtained by STS, exhibiting QPI patterns around defects and at a step edge. Bottom: FFT of the dI/dV Image. Hexagonally arranged dots refer to the reciprocal lattice of $BiCu_2$. The circles and hexagon in the centre refer to scattering processes from the two surface states. (f) Radial average of the FFT-images. Arrows indicate the peaks related to scattering vectors q_1(blue), q_2 (red) and q_{12} (green). (g) Right: scheme of the degenerate surface state (black) and the spin split Rashba-type surface state (red and blue), with observable scattering processes q_1, q_2 and q_{12}, resulting in a scattering pattern shown on the left. (h) Experimentally found dispersion $E(\boldsymbol{k})$ deduced from the scattering peaks as in (f). In the background a comparison with the band structure recorded by ARPES is shown. Adapted from [125].

cone and can be described by

$$\boldsymbol{q}_{\mathrm{G-Au,1}} = \overline{\Gamma\mathrm{K}} + \boldsymbol{k}_{\mathrm{G}} - \boldsymbol{k}_{\mathrm{Au,1}} \tag{6.7}$$

$$\boldsymbol{q}_{\mathrm{G-Au,2}} = \overline{\Gamma\mathrm{K}} + \boldsymbol{k}_{\mathrm{G}} - \boldsymbol{k}_{\mathrm{Au,2}}. \tag{6.8}$$

This allows an extraction of the strength of the spin-orbit coupling (Figure 6.5(d)). In the presence of the graphene sheet, the Au surface state survived, but was shifted by 100 meV. Further effects on the band structure of Au might exist.

These techniques show that it is in general possible to probe the spin-orbit coupling with QPI using STM. Both approaches are, however, restricted to very special sample systems, either additional bands have to be present or they have

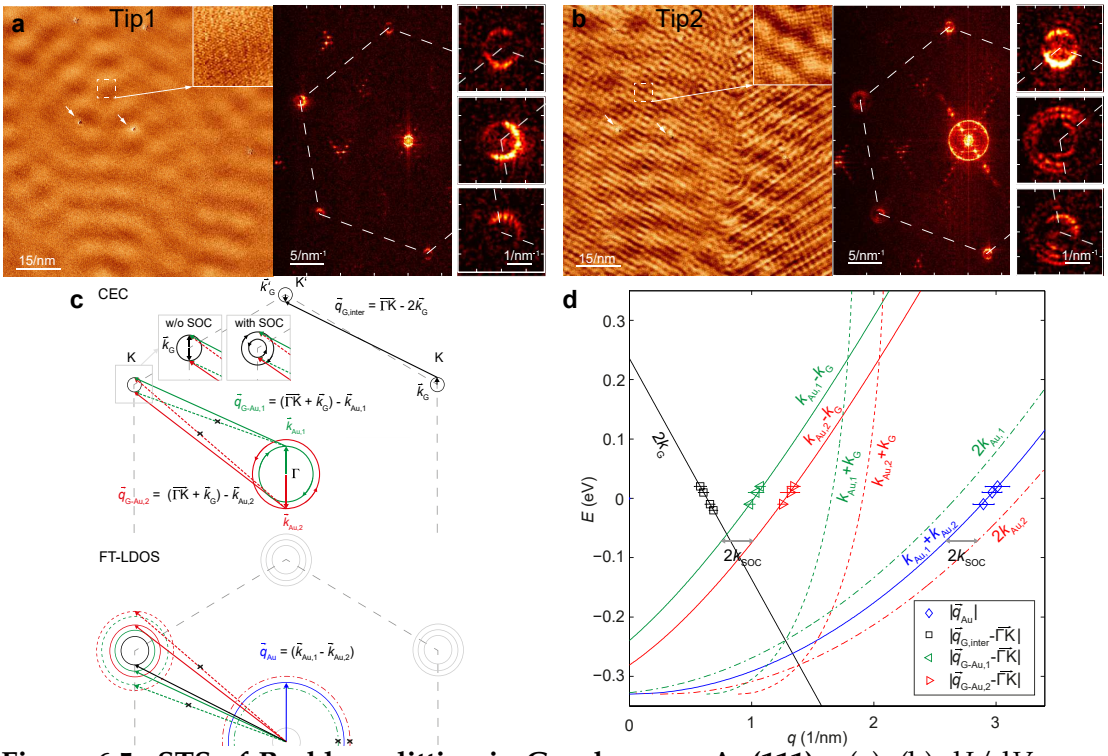

Figure 6.5.: STS of Rashba splitting in Graphene on Au(111) – (a), (b) dI/dV maps of a graphene layer on Au(111) obtained with two different tip configurations. (a) not sensitive to Au(111) states. FFT of the QPI shows intravalley and intervalley scattering of graphene (magnified on the right) for three different corners of the BZ. BZ is indicated by the dashed lines. (b) sensitive to graphene and Au(111) states. Large ring at the centre of the FFT belongs to the Au(111) surface state backscattering and two additional rings at the edges of the BZ indicate interband scattering between two Au(111) surface states and the graphene Dirac cone at K and K', respectively. (c) Top: constant energy contour (CEC) of p-doped graphene and Au(111) with possible scattering vectors (black: graphene intervalley & intravalley scattering; red/green: scattering from from Au(111) surface states to graphene states). Bottom: expected FFT with Au(111) backscattering (blue) and scattering between graphene and Au(111) (green and red). Dashed lines: scattering vectors not visible in the experiment. (d) Extracted dispersion relation of graphene and Au(111) from the experiment. Symbols are data points, solid lines result from ARPES data. Dashed and dotted lines are not observed in the experiment. Adapted from [126].

to be added using a top layer of a different material. Additionally, a scattering to the Rashba bands must be permitted. Even though the spin-orbit coupling was extracted using STM, a local investigation of the Rashba parameter on a nanometre scale has not been reported so far.

6.2.2. Band onset singularity

The spin-orbit coupling splits a 2D parabolic band radially by $k_0 = m^*\alpha_R/\hbar^2$. The zero-dimensional point-like band extremum at $k_0 = 0$ thereby turns into quasi one-dimensional extremal ring structure [130]. This leads to a singularity in the DOS. This singularity is observable in STS and is a fingerprint for the strength of the spin-orbit coupling. Figure 6.6(a)(left) shows the theoreti-

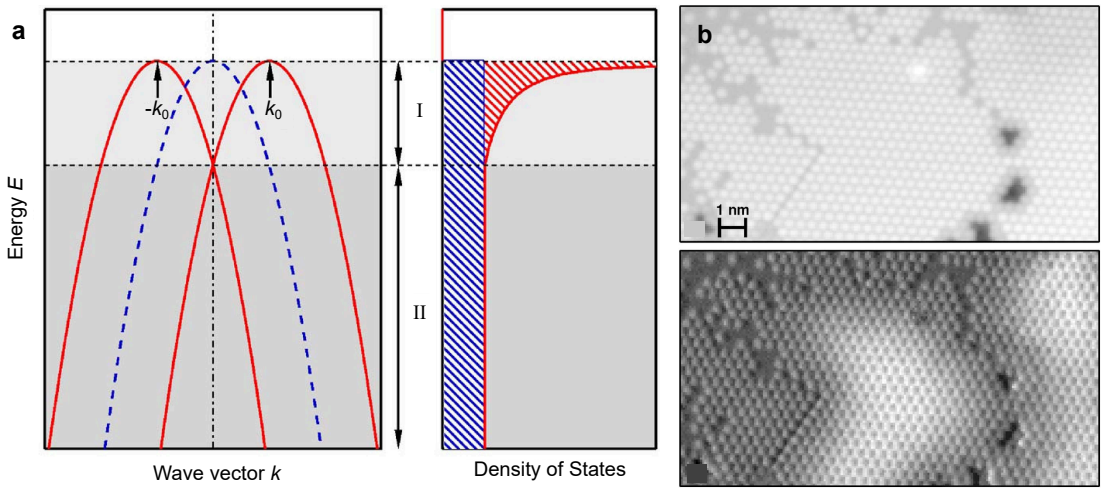

Figure 6.6.: Spin-orbit coupling on Bi/Ag(111) – (a) Left: energy dispersion calculated using a 2D nearly free electron model with (red solid lines) and without (blue dashed line) spin-orbit coupling. Right: associated DOS, indicating region I with the Van Hove singularity exhibiting $D(E) \propto 1/\sqrt{E}$ and region II with a constant DOS. (b) Top: STM-topography image obtained at $V = -137\,\mathrm{mV}$ (energy close to the Van Hove singularity). Bottom: corresponding $\mathrm{d}I/\mathrm{d}V$ measurement. Bright areas show stronger singularity peak than darker areas. Adapted from [130].

cal splitting of the Rashba parabolas. The DOS $D(E)$ differs for the two energy regions I and II and is given by

$$D(E) = \begin{cases} \frac{|m^*|}{\pi\hbar^2}\sqrt{\frac{E_R}{E-E_0}}, & E \in \text{region I}, \\ \frac{|m^*|}{\pi\hbar^2} = \text{const.}, & E \in \text{region II}. \end{cases} \tag{6.9}$$

Here, $E_R = \hbar^2 k_0^2/2m^*$ describes the energy shift of the bands, which is called the Rashba energy and E_0 is the band onset energy. This results in the DOS shown in Figure 6.6(a)(right). While region II only consists of the constant DOS as far as a 2DES without spin-orbit coupling, region I shows the singularity due to $\alpha_R \neq 0\,\mathrm{eV\AA}$. In STS, this singularity is broadened into a peak by finite lifetime and experimental broadening, e.g. by electron temperature. Ast et. al [130]

gain information about the strength of the spin-orbit coupling by fitting the DOS to their STS data. LDOS spectra for Bi/Ag(111) and Pb/Ag(111) obtained by STS and corresponding ARPES measurements are shown in Figure 6.7(a) & 6.7(b). While the effective mass was retrieved from the ARPES measurements, the life-time broadening and Rashba energy are determined by the LDOS fit. For the Bi/Ag(111)-system, both techniques result in similar Rashba energies of $E_{R,STS} = 195\,meV$ and $E_{R,ARPES} = 208\,meV$. However, for the Pb/Ag(111) system, the Rashba energies $E_{R,STS} = 67\,meV$ and $E_{R,ARPES} = 23\,meV$ differ by a factor of three. This is mainly attributed to the fact that in ARPES only occupied states can be observed. The band maxima are unoccupied and the band course has to be estimated.

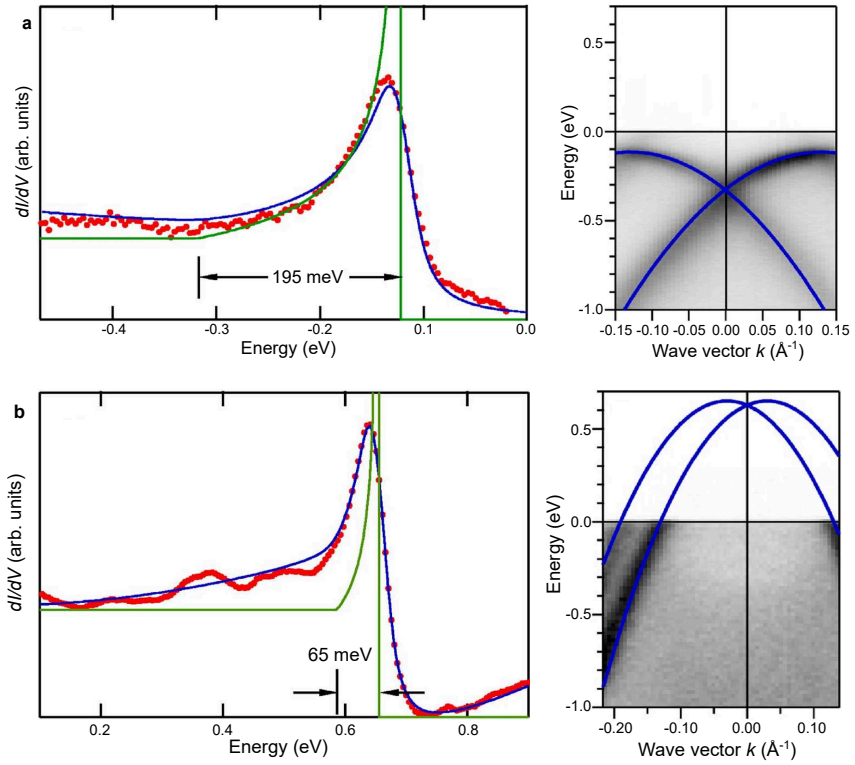

Figure 6.7.: Band structure and DOS of Bi/Ag(111) & Pb/Ag(111) by ARPES and STM – Left: STS-spectra (red dots) obtained close to the van Hove singularity for (a) Bi/Ag(111) and (b) Pb/Ag(111). Tersoff-Hamann fit [31] plotted as blue line and the green line shows the unconvoluted DOS. Right: ARPES measurements of the alloys (a) Bi/Ag(111) and (b) Pb/Ag(111). The blue guiding lines show the band maxima around the position of the peaks in the STS measurements. [130]

This singularity can be followed across a sample surface (Figure 6.6(b)), to reveal local changes of its intensity. Assuming that the experimental broadening

is constant, these changes can result from either changes in spin-orbit coupling or life-time. If the life-time broadening dominates the Rashba energy, as is the case for the Au(111) surface state ($E_R = 18\,\text{meV}$, $\Gamma_\text{L} = 18\,\text{meV}$ [131]), the singularity is no longer present in STS. The life-time broadening becomes not only detrimental for a system with small Rashba energy, but also impedes a discrimination between life-time broadening and energy splitting in the attempt to map the local spin-orbit coupling.

6.2.3. Beating pattern in the density of states

Applying a perpendicular magnetic field breaks the spin degeneracy. In a 2DES, STS can be used to observe LL splitting and, at high magnetic fields, an additional spin splitting. Becker et al. [107] used this approach to determine the Rashba spin-orbit coupling in p-InSb with Cs adsorbed on the (110)-surface, resulting in a surface 2DES accessible by STS (see Section 7.1). STS shows a beating pattern in the spatially averaged local density of states (Figure 6.8(a)) which is well known for transport experiments [114]. The beating is a result of the superposition of the LL splitting and the Rashba spin splitting leading to two bands with different LL distances. The Rashba parameter can be estimated by comparing the beating pattern, observable in STM, with a calculated density of states (Figure 6.8(b)).

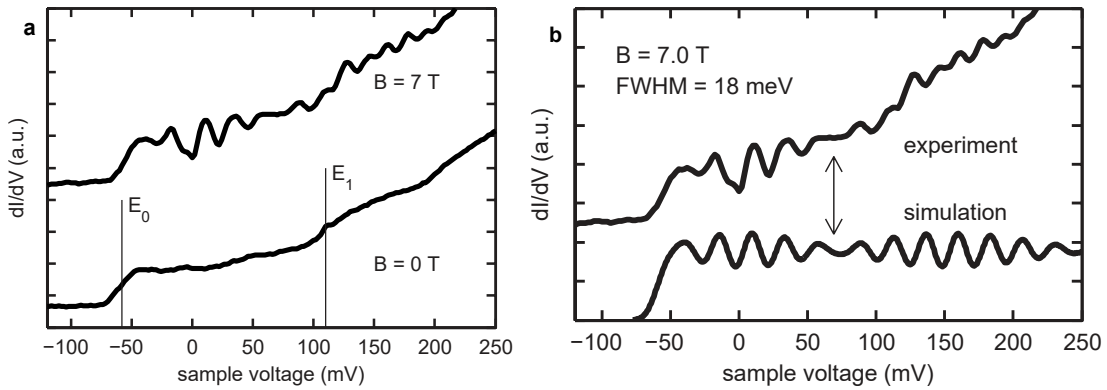

Figure 6.8.: Beating pattern by spin-orbit coupling and LL-splitting – (a) Spatially averaged density of states of the surface 2DES of Cs/p-InSb. Bottom: $B = 0\,\text{T}$, two subbands starting at $E_0 = -60\,\text{meV}$ and $E_1 = 110\,\text{meV}$ of the 2DES located at the sample surface are visible. Top: $B = 7\,\text{T}$ (perpendicular to the 2DES). A beating pattern due to LL-splitting and Rashba-splitting appears. (b) Comparison between simulated (bottom) and experimentally observed (top) beating patterns. The gradually increasing density of states observed at higher energies in the experiment originates from bulk states.

The DOS is given by

$$D(E) = \frac{1}{(2\pi)^3/2l_B^2\Gamma} \sum_{n,\sigma} e^{-\frac{(E-E_n^\sigma)^2}{2\Gamma^2}}, \tag{6.10}$$

using the exact eigenvalues for the Hamiltonian $H_0 + H_\alpha$ given by Equation (5.10) and using a broadening Γ caused mainly by potential disorder. The potential fluctuations have a direct effect on the low energy states of the 2DES. Thus, peak positions in the LDOS (Figure 6.9) can shift with the potential disorder. Consequently, one has to use the spatially averaged spectrum for comparison with the theoretical LDOS. A comparison with simulated beating patterns of the DOS reveals a spatially averaged spin-orbit coupling of $\alpha_R = 0.7\,\mathrm{eV\AA}$. Moreover, it has been found that the spin splitting ΔE_{SS} changes with position. It is $\Delta E_{SS} \approx 15\,\mathrm{meV}$ at a lower potential (Figure 6.9 circle) and $\Delta E_{SS} \approx 18\,\mathrm{meV}$ at a potential 20 meV higher (square). This can, as discussed later, be explained by a local variation of the Rashba parameter (Section 7.4). The spatial variation of the spin splitting is used in this work to probe the spin-orbit coupling on the nm scale.

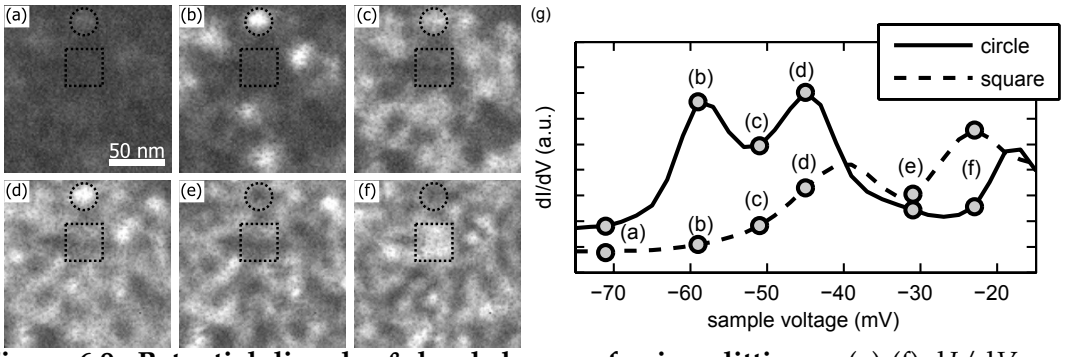

Figure 6.9.: Potential disorder & local change of spin splitting. – (a)-(f) $\mathrm{d}I/\mathrm{d}V$ maps obtained at various energies marked in (g), $B = 7\,\mathrm{T}$, $150\,\mathrm{nm} \times 150\,\mathrm{nm}$. (g) spatially averaged spectra of the areas marked on the left, referring to areas of different potential.

6.3. Observations of potential disorder and driftstates in 2DES via STS

Electron wave functions have been investigated intensively using STM on metals [18, 132], semiconductors [21, 133] and graphene [22]. For distinct quantised LL wave functions no real space observation has been reported so far [133]. Most 2DES are buried deep below the surface and are not accessible using

STM. Surface doping of semiconductors makes a 2DES available for STM experiments.
Most physical effects are highly sensitive to the electrostatic potential, leading to a trend towards using very clean samples for the most controlled experimental conditions. Alternatively, the confinement potential is scaled up, so that intrinsic potential fluctuations become negligible [18, 132]. An insight on such fluctuations is necessary to understand their detrimental effect or partly contributing effects in, for instance, the quantum Hall effect. The STM tip itself changes the local potential considerably due to tip-induced bend bending [134], which can be used to probe the electrostatic potential locally.

6.3.1. Potential disorder probed by tip-induced quantum dot

Dombrowski et al. [135, 136] demonstrated that the lowest energy state of the tip-induced quantum dot (QD) follows the electrostatic potential while scanning across the sample surface. A tungsten tip is approached to a degenerately doped n-InAs(110) sample surface and a bias voltage of $V = 100\,\mathrm{mV}$ is applied. The vacuum potentials of the tip and sample are different, leading to a downwards bending of the conduction band (Figure 6.10(a)), such that tip-induced states and the conduction band minimum E_{BCBM} lie below E_{F}. These tip-induced states are confined by the conduction band in z-direction, as well as in the lateral direction due to the finite extension of the tip charging (Figure 6.10(b)).
The lowest energy state of the tip-induced QD was used by Morgenstern et al. to map the electrostatic 2D potential of a 2DES. In their system, the conduction band of n-InAs is bent down by surface adsorption of 0.8 % of an Fe monolayer. The tip potential additonally bends the bands down resulting in an (x, y)-confinement of a scannable QD. The energy of the lowest confined state of this QD can be followed across a scanned area (Figure 6.10(c)) to create a map of the 2D potential landscape. By applying a perpendicular magnetic field, LL quantisation can be observed and so-called LL drift states are reported. These drift states follow equipotential lines of the potential disorder $V(x, y)$, if l_B is smaller than the correlation length of $V(x, y)$ [22].

6.3.2. Nodal structure

Joynt et al. modelled non-interacting electrons in a potential disorder, showing that each LL exhibits drift states following equipotential lines of $V(x, y)$ [138] (see Section 5.3.1). The drift states exhibit a width of about the cyclotron radius l_{B}. The equipotential lines around minima and maxima are closed circles. For

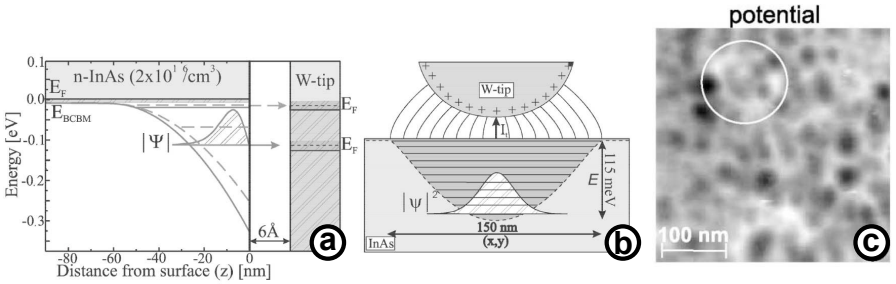

Figure 6.10.: 2D potential disorder mapped by tip-induced QD – (a) Sketch of the band diagram at the tip-induced band bending (solid line) for a tungsten tip approached to a n-InAs surface and $V = -110\,\mathrm{mV}$. Dashed lines indicate a smaller tip charging at $V \approx 0\,\mathrm{mV}$. E_{BCBM} is the bulk conduction-band minimum. The ground state wave function $|\Psi|^2$ is indicated [135]. (b) Sketch of the lateral potential for $V = -110\,\mathrm{mV}$. (+) marks the tip charges, curved lines mark the $\boldsymbol{E}$-field in the vacuum region. The gray region in the InAs sample indicates the lateral shape of the conduction band. State energies of the resulting (x, y)-confinement are marked as horizontal lines and the ground-state wave function $|\Psi|^2$ is indicated [135]. (c) Disorder potential of the 2DES induced by 0.8 % Fe on a InAs sample as determined by STS with the help of the tip-induced QD [137].

smooth potential disorder, where the correlation length of the potential is larger than the magnetic length ($l_{V2D} \gg l_{\mathrm{B}}$), the drift states of the lowest LL can be observed by STS [137, 21, 22]. The drift states of LL_0 start with a Gaussian-like distribution at low energy (Figure 6.11 (a)) and form ring structures, according to the course of the equipotential lines at higher energy (Figure 6.11 (b)). At these energies the electron states are localised. At the saddle points of the 2D potential, the equipotential lines can reach across larger surface areas and so-called extended states can be observed (Figure 6.11(c)). An extended state crossing even an infinite sample exists in the centre of the lowest LL and eventually leads to the finite resistance between the quantum Hall states [138, 139, 140, 141].

While the drift states of the LL_0 have been observed for 2D systems in semiconductors [21] and graphene [22], no traces of the nodal structures of the higher LL_n in real space have been reported. Traces of the nodal structure of LL_1 & LL_2 have only been observed in Fourier space by Hashimoto et al. [133]. The structure factor of the wave function (Equation (5.21)) and its Fourier transform

$$\tilde{F}_n(\boldsymbol{q}) = L_n\left(\frac{\boldsymbol{q}^2 l_B^2}{2}\right)\exp\left(\frac{-\boldsymbol{q}^2 l_B^2}{4}\right), \tag{6.11}$$

exhibit the same nodal structures as the LL wave function given by the Laguerre polynomial that is only smeared out by the potential disorder. These nodal

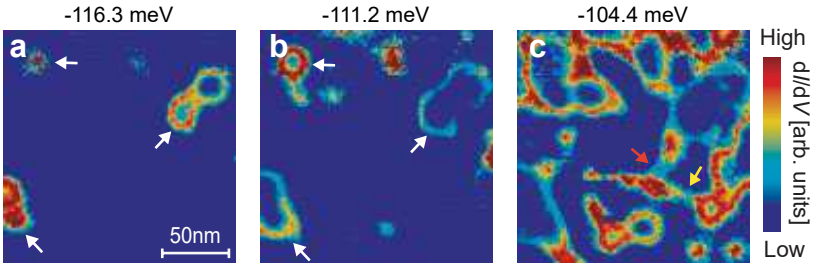

Figure 6.11.: Localised and extended drift states – $\mathrm{d}I/\mathrm{d}V$ maps obtained on Cs/n-InSb(110) at different voltages within LL_0. (a), (b) Energies lie at the beginning of the lowest spin-polarised LL. White arrows mark same region around a potential valley. (c) Energy close to the centre of the lowest spin-polarised LL. Extended states across the sample are formed. Coloured arrows indicate tunnelling connections between drift states appearing at saddle points. ($B = 12\,\mathrm{T}$, $V_{\mathrm{stab}} = 150\,\mathrm{mV}$, $I_{\mathrm{stab}} = 0.1\,\mathrm{nA}$, $V_{\mathrm{mod}} = 1\,\mathrm{mV}$, $T = 0.3\,\mathrm{K}$) Adapted from [21].

structures are following the equipotential lines of the potential. This means that for LL_1 a double ring is expected at potential extrema and double stripes are expected at extended states. Figures 6.12(a)-(d) show angularly averaged

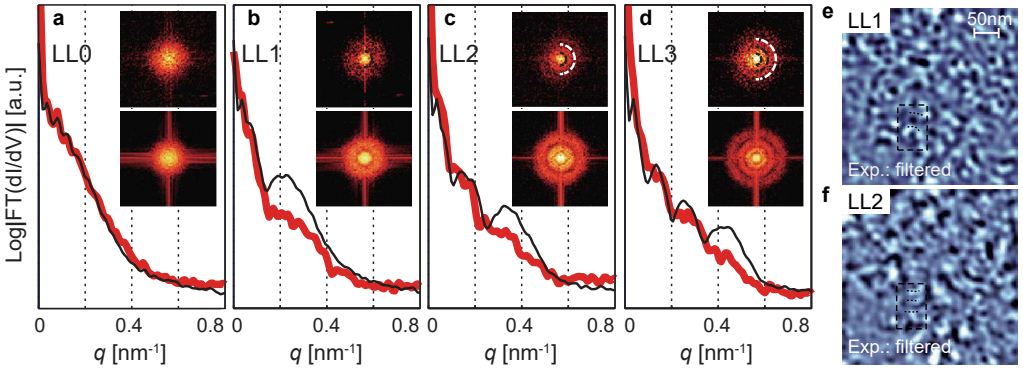

Figure 6.12.: Nodal structures of LL wave functions resolved by Fourier Transform-STM – (a)-(d) Angularly averaged FFT of $\mathrm{d}I/\mathrm{d}V$ maps obtained at the tail of LL_0, LL_1, LL_2 & LL_3 (red lines). Black line: corresponding numerical simulations. Insets: FFT of experimental data (upper) and simulation (lower). (e) & (f) Fourier band-pass filtered real space LDOS measurements with additional low-pass filter $|\boldsymbol{q}| \leq 0.52\,\mathrm{nm}^{-1}$. Dashed rectangles mark same area in (e) & (f) for comparison. Dashed curved lines highlight antinodes. ($B = 6\,\mathrm{T}$, $V_{\mathrm{stab}} = 150\,\mathrm{mV}$, $I_{\mathrm{stab}} = 0.1\,\mathrm{nA}$, $V_{\mathrm{mod}} = 1\,\mathrm{mV}$, $T = 0.3\,\mathrm{K}$). Adapted from [133].

Fourier transformations of $\mathrm{d}I/\mathrm{d}V$ maps taken at the energetic tails of different LL_n's (red lines), as well as numerical simulations (black lines). The Fourier transforms of the LDOS($\boldsymbol{r}$) show an increasing amount of modulations that correspond with the nodes of the LL wave functions. Applying a high- and a low-

pass fast Fourier filter (FFT) on experimental dI/dV maps (Figure 6.12(e)&(f)) makes traces of the n nodes of the n^{th} LL visible. At the end of this thesis, the first direct and unfiltered measurements of these nodal structures in real space are presented (Section 7.5).

7. Experiments on p-InSb(110)

The experiment was performed using the STM system described in the first part of this thesis. The STM measurements were carried out at 8 K & 400 mK and various magnetic fields up to 14 T. The following section describes the sample system and its preparation (Section 7.1), followed by the mapping of the potential disorder (Section 7.2), local probing of the Rashba parameter (Sections 7.3 & 7.4) and a real space image of the nodal structure of LL wave functions (Section 7.5).

7.1. 2DES in Cs/p-InSb(110)

InSb is a III-V semiconductor with a band gap of $E_G = 235\,\text{meV}$. Due to its high atomic mass, it exhibits a strong spin-orbit coupling. Here, a p-doped sample with a Ge doping concentration of $N_{3D} = 10^{24}\,\text{m}^{-3}$ is used. The conduction band is bent down, using surface n-doping (cf. Figure 7.1(a)). Photoelectron spectroscopy showed that the maximal band bending of $E_{BB} = 290\,\text{meV}$ is already present for a Cs surface coverage of 1 % [142], thus, for 1.8 % Cs coverage, as used in this thesis, the conduction band is bent below E_F. The corresponding parabolic band of the 2DES at 2 % Cs has been mapped using ARPES exhibiting its origin at $E - E_F = -105\,\text{meV}$ [143]. Besides the charging of the bulk acceptors close to the surface, the adsorbents donate electrons to the 2DES located up to the surface and this results in a depletion depth of $z_D \approx 30\,\text{nm}$ [107]. With such a strong band bending, subbands are expected to be below, as well as above, the Fermi energy. This relatively strong band bending leads to a strong $\boldsymbol{E}$-field in the 2DES resulting in a Rashba parameter of about $\overline{\alpha_R} = 0.7\,\text{eVÅ}$ [107]. The strength of the $\boldsymbol{E}$-field depends on the exact shape of the local band bending. This can vary, depending on the density of surface adsorbates and the distribution of the Ge acceptors (cf. Section 7.4.3). The average distance of the Ge acceptors of $d_{Ge} = 10\,\text{nm}$ is smaller than that of the surface dopants $d_{Cs} = 4\,\text{nm}$ ($N_{2D} = 6 \cdot 10^{16}\,\text{m}^{-2}$). Assuming a homogeneous Cs distribution, the conduction band minimum E_{CBM} is pinned at a fixed energy. The variations in Ge doping therefore change the shape of the band bending. Thus, a locally enhanced Ge doping leads to steeper bands and in turn higher electric fields (see Figure 7.1(b)). The rather homogeneous distribution of charge within the Cs layer can be justified by experiments which

reveal that the potential disorder within the 2DES decreases with increasing Cs coverage [143]. This is rationalised by the fact that the Cs gets only partly charged above a coverage of 1 %. Thus, the remaining electron charge in the Cs layer itself can be used to screen potential fluctuations, most effectively within the Cs layer. Moreover, $d_{Cs} = 4\,nm$ is smaller than the extension of the 2DES in the vertical direction ($\approx 10\,nm$), such that the vertical averaging additionally reduces the potential fluctuations due to the Cs layer.

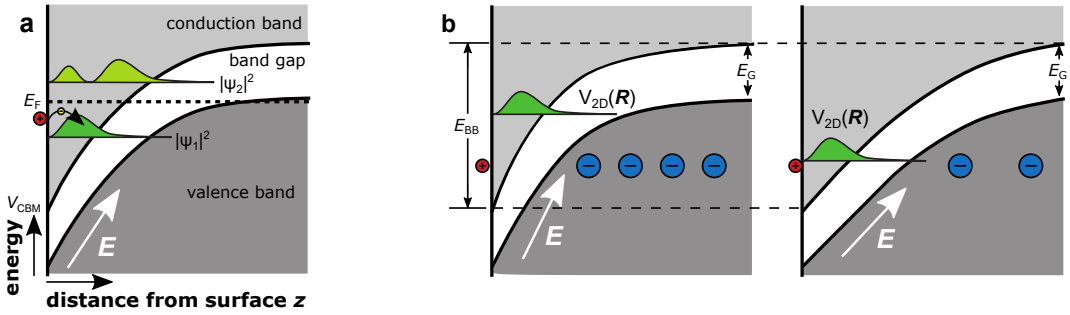

Figure 7.1.: Band structure of Cs/p-InSb (110) – (a) Band structure of the 2DES perpendicular to the surface, as the result of a Poisson calculation [67]. Confined wave functions are sketched in green. Adsorbed Cs (red) acts as a donor (b) Band structure as shown in (a) with different Ge densities close to the surface leading to shapes of band bending. The total band bending at the surface E_{BB} is pinned by the Cs atoms. A flatter band leads to a lower energy of the subbands V_{2D} and a larger electric field.

The bands of III-V semiconductors are non-parabolic and since the band bending is much larger than the band gap of InSb E_G, a description by a triangular well approximation with constant m^* [144] can be inaccurate for deducing the 2DES subband energies.

7.1.1. Preparation of p-InSb

Preparation of InSb(110)-crystal for STM and transport

An InSb crystal[1] is glued with a conductive epoxy onto a Molybdenum sample holder for the STM experiments (see Figure 7.2(a)), and onto a chip carrier for the Hall measurement. A 1 mm deep notch was cut into the crystal to allow cleaving of the (110) surface. For the UHV cleaving, necessary for the STM experiment, a small screw was glued on top of the crystal. Inside an UHV chamber, at a base pressure of 10^{-10} mbar, the crystal was cleaved at the notch

[1] CrysTec GmbH Kristalltechnologie, Berlin, Germany

by pushing the screw towards the chamber wall. After in-situ transfer into an STM within 1 hour and direct cooling to 9 K, 4 K, 1.5 K and 400 mK, respectively, atomically clean and flat terraces with a width of several µm were found. The sample for the Hall measurement is cleaved at ambient conditions and contacted with conductive epoxy, before inserting it into a 300 mK transport cryostat.

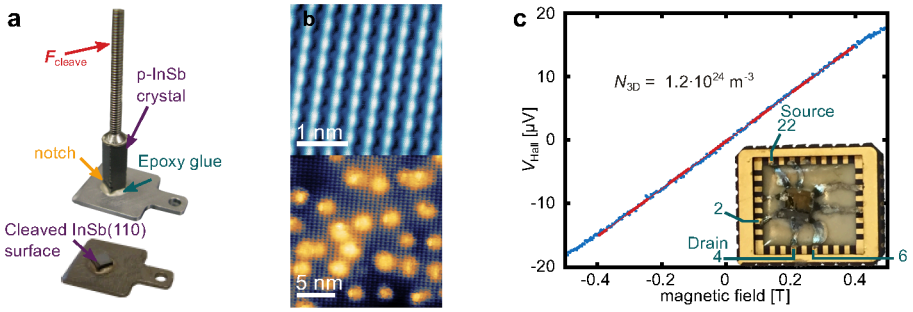

Figure 7.2.: InSb samples for STM and transport measurements – (a) Top: Molybdenum sample holder with InSb-crystal glued on top. A notch 1 mm is cut into the base of the crystal to initiate cleavage of the (110) surface. As elongation of the lever arm, a screw is attached at the top of the crystal. Bottom: same sample holder after cleavage, evaporation and STM measurements. (b) Top: STM image of a pristine InSb(110) surface with atomic resolution ($V = 350\,\mathrm{mV}$, $I = 2\,\mathrm{nA}$, $T = 8.5\,\mathrm{K}$, $3 \times 3\,\mathrm{nm}^2$). Bottom: after deposition of 1.8 % of a monolayer of Cs ($V = 300\,\mathrm{mV}$, $I = 30\,\mathrm{pA}$, $T = 8\,\mathrm{K}$, $20 \times 20\,\mathrm{nm}^2$). (c) Hall measurement (blue dots) at 2 K and corresponding linear regression (red dashed line) used for the determination of the carrier density N_{3D}. Inset: InSb crystal glued on a carrier chip for transport measurements with 8 contacts attached. Source: #22; Drain:#4 (GND); V_{Hall}: #6 & #2.

Carrier Density of the InSb-Crystal

A Hall measurement has been used as verification of the carrier density specified by the InSb crystal supplier (see Figure 7.2(c)). A constant DC current of $I = 5\,\mathrm{mA}$ is driven from source to drain (contacts #22 & #4) and the Hall voltage V_{Hall} between contacts #6 and #2 is acquired. The crystal has the thickness $d = 0.7\,\mathrm{mm}$. The Hall measurement is performed in a ^{3}He-cryostat at $T = 2\,\mathrm{K}$. $N_{3D} = I/ed \cdot B/V_{\mathrm{Hall}}$ leads to an acceptor density of $N_{3D} = 1.2 \cdot 10^{24}\,\mathrm{m}^{-3}$ in good agreement with the N_{3D} given by the supplier.

Deposition of Cs submonolayer

The cleaved surface of the p-doped InSb, with acceptor density $N_{3D} = 1.2 \cdot 10^{24}\,\mathrm{m}^{-3}$, was immediately transferred under UHV conditions into a sample

stage hold at $T = 30\,\mathrm{K}$. The sample stage is positioned inside the thermal shielding of the ^{4}He-bath. The sample surface is facing the Cs evaporator. The sample-evaporator distance is about $d = 180\,\mathrm{mm}$. In front of the evaporator a Cs dispenser[2] is mounted, which is operated at 470°C and contains caesium chromate. The manipulator is put into contact with the shield of ^{4}He-bath for the duration of the evaporation procedure to precool the plier. After three evaporation cycles of 180 s, the sample is immediately transferred into the STM and cooled down to 1.5 K. During the whole procedure of transfer and evaporation, the pressure did not exceed $p = 1.6 \cdot 10^{-9}\,\mathrm{mbar}$. It is found that the surface coverage is 1.8 % of a monolayer of Cs, defined as one Cs atom per InSb unit cell. This is determined by counting the Cs atoms and clusters in several areas.

7.2. Mapping of the Potential disorder, $m^*(E)$ and $g^*(E)$

7.2.1. Potential disorder

In a magnetic field of $B = 6\,\mathrm{T}$, spin split LLs are observed in the LDOS (Figure 7.3(a)). The two peaks belong to LL_0 and can be identified as $\varepsilon_{1,+} = -99\,\mathrm{meV}$ (blue) and $\varepsilon_{0,-} = -86\,\mathrm{meV}$. The width of the states $\sigma_{\varepsilon_{1,+}} \approx \sigma_{\varepsilon_{0,-}} = 5.5\,\mathrm{meV}$ is broader than expected from broadening by the Fermi distribution of $T = 400\,\mathrm{mK}$. They might be related to the reduced life-time of holes far below the Fermi energy. In single point STS-measurements, the peaks are fitted with a double Lorentzian curve with amplitude, width and energy as fitting parameters. The local potential is probed by tracing the mean value of the peaks of LL_0 across the sample surface in $\mathrm{d}I/\mathrm{d}V$ measurements. The mean value

$$V_{2\mathrm{D}} = \frac{1}{2}(\varepsilon_{1,+} + \varepsilon_{0,-}) \tag{7.1}$$

is defined as the 2D-potential $V_{2\mathrm{D}}$. This makes sense, since drift states are believed to cover equipotential lines, such that they show the local potential directly with a resolution of l_B. Note that l_B is nearly identical to the vertical extension of the 2DES, which means that potential fluctuations on smaller length scales than l_B barely exist. Figure 7.3(b) shows such a potential map, which is additionally smoothed with a Gaussian of width $l_B = 10.5\,\mathrm{nm}$. Higher magnetic fields would lead to a possibly finer mapping of the potential, but also makes exchange enhancement [145] more relevant. Indeed, the correlation length of

[2] SAES Getters, Milan, Italy

the potential disorder is $l_{V_{2D}V_{2D}} = 50\,\text{nm} > l_B$ as calculated according to the definition in Equation (5.32) by

$$l^2_{V_{2D}V_{2D}} = 2\pi \int_0^S f_{V_{2D}V_{2D}}(x) x dx, \tag{7.2}$$

with the dimensionless function $f_{V_{2D}V_{2D}}$ being the Gaussian fit of the angularly averaged potential auto-correlation $\langle V_{2D}|V_{2D}\rangle$ (inset Figure 7.3(c)) up to the point $S_{V_{2D}V_{2D}} = 50\,\text{nm}$ where the correlation plot crossed zero the first time. The large value of $l_{V_{2D}V_{2D}} \gg d_{Cs}$ supports the claim that the distribution of the Ge is the origin of the potential disorder, which is further discussed in Section 7.4.2.

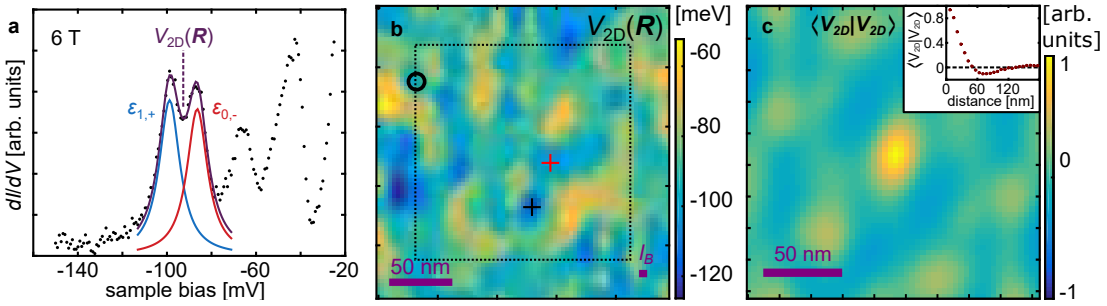

Figure 7.3.: Mapping of the 2D Potential disorder – (a) Single position $\mathrm{d}I/\mathrm{d}V$ spectrum. $V_{stab} = 50\,\text{mV}$, $V_{mod} = 1.4\,\text{mV}$, $I_{stab} = 100\,\text{pA}$, $B = 6\,\text{T}$, $T = 400\,\text{mK}$. Fit marked violet, with correspondingly labelled Lorentzian peaks marked in red and blue, respectively. $V_{2D}(\boldsymbol{R})$ is identified as the average of the two LL peak energies as marked. (b) Obtained 2D potential map extracted from 75×75 single point spectra after being smoothed with a Gaussian of width l_B. Position of spectrum shown in (a) is marked by the circle. The dotted square indicates the area of the effective potentials in Figure 7.4. The red and the black cross mark positions in which curves in Figure 7.11(b) were obtained (with corresponding colour). (c) auto-correlation of $V_{2D}(\boldsymbol{R})$. Inset: radial average of the auto-correlation $\langle V_{2D}|V_{2D}\rangle$ revealing $l_{V_{2D}V_{2D}} = 50\,\text{nm} \gg d_{Cs}$.

In the model of Hernangómez-Pérez et al. [102] (see Section 5.3), the nth LL experiences an effective potential $V_{2D,n}(\boldsymbol{R})$, which is due to the convolution of the probability density of the particular wave function and the 2D potential V_{2D}. It can be obtained by convolving the kernel functions $F_n(\boldsymbol{r} - \boldsymbol{R})$ (Equation (5.21) with $V_{2D}(\boldsymbol{R})$ according to Equation (5.19). Figure 7.4 shows the effective potentials $V_{2D,0}(\boldsymbol{R})$ & $V_{2D,1}(\boldsymbol{R})$ calculated for the centre area of the electrostatic potential map $V_{2D}(\boldsymbol{R})$ shown in Figure 7.3(b). While the 2D potential is exhibiting a variation of $\sigma_{V_{2D}} = 10\,\text{meV}$, the effective potentials are naturally smoother. At the minimum in the 2D potential marked by the black cross in Figure 7.3(b) and Figure 7.4, $V_{2D,1}$ shows a maximum. Such an effect can be explained by

the additional node of wave functions of LL_1. This also explains the smaller strength of the fluctuations present in $V_{2D,1}$ compared to $V_{2D,0}$. The scaling of the cyclotron radii $R_n = l_B\sqrt{2n+1}$ leads to a smoother effective potential $V_{2D,1}$ with respect to $V_{2D,0}$.

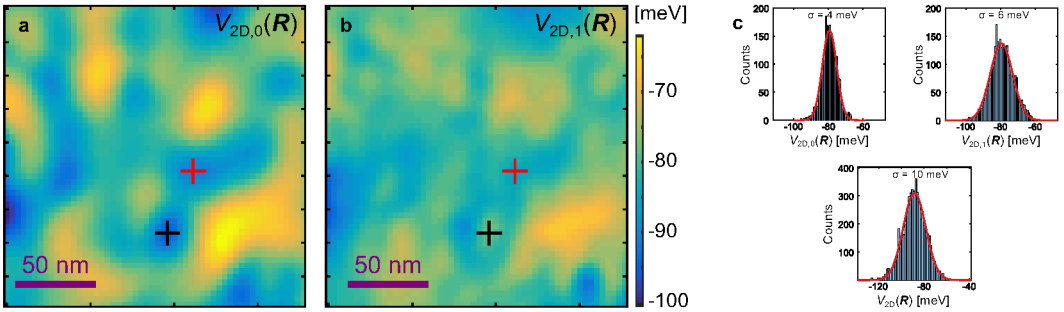

Figure 7.4.: Effective potentials $V_{2D,0}(R)$ & $V_{2D,1}(R)$ – (a) Effective potential $V_{2D,0}(R)$ calculated from $V_{2D}(R)$ showing the area of the dotted square of Figure 7.3(b). (b) Same area as (a) showing $V_{2D,1}(R)$. (c) Histograms of $V_{2D,0}(R)$, $V_{2D,1}(R)$ & $V_{2D}(R)$ with fitted Gaussians (red lines) and indicated σ-widths. The electrostatic potential varies by $\sigma_{V_{2D}} = 10\,\text{meV}$ and the effective potentials by $\sigma_{V_{2D,1}} = 6\,\text{meV}$ and $\sigma_{V_{2D,0}} = 4\,\text{meV}$.

7.2.2. $m^*(E)$ and g^* using QPI

We firstly map $E(k)$ using the QPI. Systems with a parabolic dispersion relation are described using a constant effective mass. In small band gap semiconductors, like InSb, the valence and conduction band interact strongly. This results in a non-parabolicity of the energy dispersion and the effective mass of the electrons m^* becomes energy dependent. For a full description of the system, knowledge of the effective mass is crucial. The band distribution is most directly accessible by ARPES but also by scanning probe techniques (see Section 6.2). One approach is to look at the quasi particle interference patterns, visible in $\mathrm{d}I/\mathrm{d}V$ spectroscopy [18, 107]. This technique requires sample areas of $100 \times 100\,\text{nm}$. A more local method, which is introduced in this work, uses the LL splitting $\Delta E_{LL} = \hbar eB/m^*$ of single-point spectroscopy. It can be applied down to about $l_B \approx 8\,\text{nm}$ at $10\,\text{T}$ and still provides an energy dependence, if different LL pairs are used.
The $\mathrm{d}I/\mathrm{d}V$ maps are shown in Figure 7.5 (top), all recorded at the same area but at different energies. Towards higher energy the wavelength of the observed patterns decreases. Although the dispersion relation of p-InSb exhibits a Rashba split parabola only a single parabola contributes to the pattern (cf. Section 6.2). The Fourier transform of those $\mathrm{d}I/\mathrm{d}V$ maps (Figure 7.5) therfore exhibits a single ring structure with radius q, depicting spin conserving scattering between

the two branches of the Rashba band. The scattering vector $|\boldsymbol{q}| = |\boldsymbol{k}_1 - \boldsymbol{k}_2|$ is twice as long as the wave vector of the dispersion relation $k_{||}$ due to dominant backscattering ($\boldsymbol{k}_1 = -\boldsymbol{k}_2$).

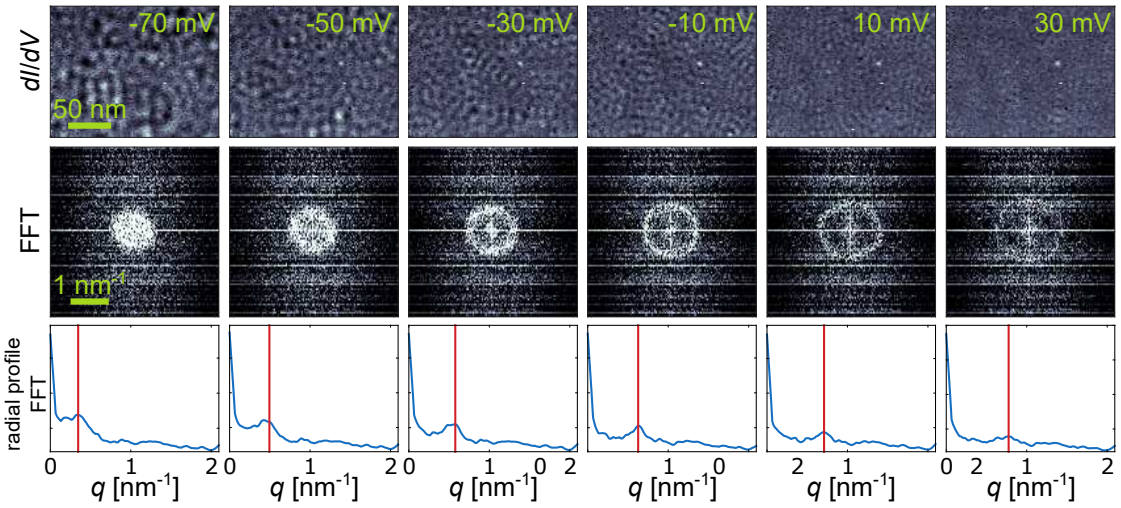

Figure 7.5.: Quasi-particle interference pattern on Cs/p-InSb(110) – Top: $\mathrm{d}I/\mathrm{d}V$ maps obtained at the same sample area for $V = -70\,\mathrm{mV}$ to $30\,\mathrm{mV}$ ($I_{\mathrm{stab}} = 200\,\mathrm{pA}$, $V_{\mathrm{stab}} = 300\,\mathrm{mV}$, $V_{\mathrm{mod}} = 3.5\,\mathrm{mV}$, $f = 645.6\,\mathrm{Hz}$, $T = 390\,\mathrm{mK}$, $B = 0\,\mathrm{T}$). Centre: corresponding FFT images. Ring structure corresponds to intraband scattering. Bottom: radial profiles of the FFT, by angularly averaging around the centre. The red line indicates the position of the ring of $q = |2k_{||}|$.

The Rashba effect only shifts the complete 1D cuts of the bands in k-direction, such that both spin branches still show the same dispersion relation, and thus, the scattering vectors $q = |2k_{||}|$ directly map the dispersion without Rashba effect (Figure 7.6). A parabolic band cannot fit the observed $E(\boldsymbol{k})$ distribution. Towards higher energies these differences become significant. Better correspondence is found using the effective mass given by the Kane model in a triangular well approximation

$$m^*(E) \cong m_0^* \left(1 + \frac{1/3 \cdot E_i + E_{||}}{E_{\mathrm{g}}}\right), \tag{7.3}$$

with m_0^* the effective bulk mass at the conduction band minimum, E_i the subband energy of the motion perpendicular to the interface and $E_{||}$ the kinetic energy of the motion parallel to it [144]. In this model, the effective mass increases with energy. In contrast with the linear approximation, the increase of the effective mass with subband energy E_i is sublinear. Even though E_i is greater than the band gap of InSb $E_g = 235\,\mathrm{meV}$, placing us beyond the validity range of the

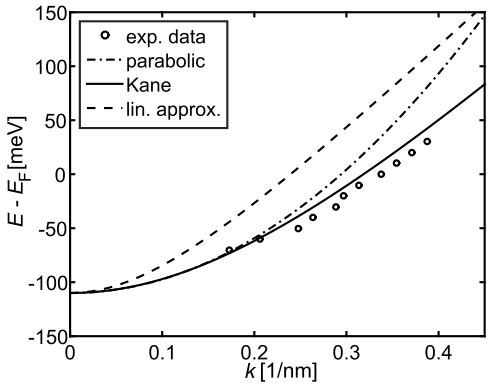

Figure 7.6.: Dispersion relation of Cs/p-InSb(111) – The dispersion relation extracted from the QPI of Figure 7.5 (circles) compared with a parabolic dispersion relation ($m^* = 0.03 \cdot m_e$, dashed-dotted line), the triangluar well approximation according to the Kane model ($E_i = 400\,\text{meV}$, $m^* = 0.03 \cdot m_e$ - solid line) and the linear approximation ($E_i = 400\,\text{meV}$, $m^* = 0.03 \cdot m_e$ - dashed line).

approximation, the deviation from the experimental data is much smaller than for a parabolic band.

7.2.3. $m^*(E)$ and $g^*(E)$ by LL splitting

The analysis of Section 7.2.2 is averaging over a sample area $(200\,\text{nm})^2$. In this study, which focusses on the local spin-orbit coupling, information about the spatial distribution of the effective mass is essential. Knowing that the triangular well approximation describes this system relatively well, we can use the relation [146]

$$\frac{g^*(E)}{g_0^*} = \frac{m_0^*}{m^*(E)} \tag{7.4}$$

to determine the effective mass and the g-factor depending on the energy, with $g_0^* = -51$ [147] and $m_0^* = 0.0135 \cdot m_e$ [148] the g-factor and effective mass at the conduction band minimum. With a disorder, the effective mass and the g-factor vary.
A determination of the effective mass and the g-factor for a single position and a selected energy range is conducted using the LL that form when a magnetic field is applied. The g-factor is not directly accessible using the spin splitting of an LL in this system, since a Zeeman and a Rashba contribution are present. The LL splitting also contains a contribution of the spin-orbit coupling. Moreover, without spin-orbit interaction (Equation (5.9)) the splitting energy of two LLs is given by

$$\Delta E_{\text{LL}} = \hbar\omega_c = \frac{\hbar e B}{m^*}, \tag{7.5}$$

with m^* being the only material-dependent parameter. In the presence of the Rashba effect, the LL splitting changes (cf. Equation (5.10)) to

$$\begin{aligned} E_{\mathrm{LL1}} - E_{\mathrm{LL0}} &= \frac{\varepsilon_{1,-} + \varepsilon_{2,+}}{2} - \frac{\varepsilon_{0,-} + \varepsilon_{1,+}}{2} \\ &= \hbar\omega_c \,(1 - \eta) \end{aligned} \tag{7.6}$$

$$\eta = \frac{1}{2}\sqrt{(1-Z)^2 + S^2} - \frac{1}{4}\sqrt{(1-Z)^2 + 2\cdot S^2} - \frac{1}{4}(1-Z) \tag{7.7}$$

The term η can be seen as a correction to the LL splitting without Rashba effect (Equation (7.5)). In our system with $0.026 \cdot \mathrm{m_e} < m^* < 0.03 \cdot \mathrm{m_e}$, $-26 < g^* < -23$ and in case of magnetic fields between 3 T and 6 T, η is smaller than 0.06, defining the error of the m^* determination.

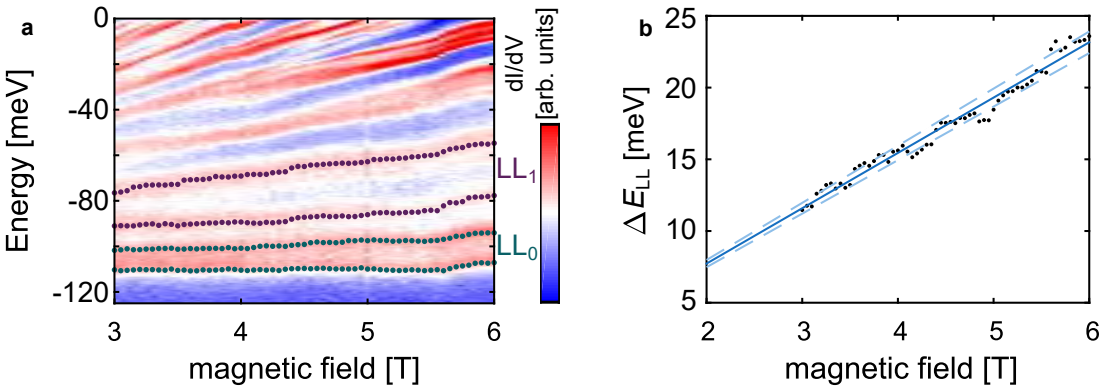

Figure 7.7.: Local determination of m^* – (a) Differential conductance $\mathrm{d}I/\mathrm{d}V$ measured at a single position ('a') for various sample biases (= energy) and magnetic fields. The two peaks of $\mathrm{LL_0}$ ($\mathrm{LL_1}$) found by a double Lorentzian fit are marked green (purple). ($V_{\mathrm{stab}} = 50\,\mathrm{mV}$, $I_{\mathrm{stab}} = 100\,\mathrm{pA}$, $V_{\mathrm{mod}} = 0.75\,\mathrm{mV}$, $T = 400\,\mathrm{mK}$). (b) LL splitting $\Delta E_{\mathrm{LL}} = \mathrm{LL_1} - \mathrm{LL_0} - \mathrm{LL_{1,offset}}$ extracted from (a). Using $\mathrm{LL_{1,offset}} = 10.8\,\mathrm{meV}$. Blue line shows a linear regression and the light blue dashed lines indicate the 65 % confidence interval, giving $m^* = (0.030 \pm 0.001)\,\mathrm{m_e}$.

Figure 7.7(a) shows a set of $\mathrm{d}I/\mathrm{d}V$ spectra for magnetic fields up to $B = 6\,\mathrm{T}$. The LL are spin split above 3 T. Apparently, $\mathrm{LL_0}$ and $\mathrm{LL_1}$ seem not to originate from the same onset energy at $B = 0\,\mathrm{T}$, but evolve from higher energy levels. This is likely caused by local confinement, since these spectra are obtained at a potential minimum (position 'a'). Nevertheless, subtracting a B-field dependent $\Delta E_{\mathrm{offset}}$ from $E_{\mathrm{LL1}} - E_{\mathrm{LL1}}$, we obtain a linear behaviour (Figure 7.7(b)), such that $m^*(\boldsymbol{R})$ can be deduced straightforwardly. The slope of the linear fit gives $m^*_{\mathrm{a}}(E_{\mathrm{LL0,a}}) = 0.03 \cdot \mathrm{m_e}$ and with Equation (7.4) $g^*_{\mathrm{a}} = -23$ at $B = 6\,\mathrm{T}$, where $E_{\mathrm{LL0,a}}(B = 0\,\mathrm{T})$ is found to be $-101\,\mathrm{meV}$. By evaluating a second sample position ('b') with a different $E_{\mathrm{LL0,b}}(B = 0\,\mathrm{T}) = -121\,\mathrm{meV}$ we find, $m^*_{\mathrm{b}} = 0.026 \cdot \mathrm{m_e}$,

i.e. $g_b^* = -26$. These two m_i^* are used to determine $m^*(\boldsymbol{R})$ within the evaluated potential map $V_{2D}(\boldsymbol{R})$ (Figure 7.3(b)) given by

$$m^*(\boldsymbol{R}) = \frac{m_a^* - m_b^*}{E_{LL0,a} - E_{LL0,b}} V_{2D}(\boldsymbol{R}) - \frac{m_a^* - m_b^*}{E_{LL0,a} - E_{LL0,b}} E_{LL0,a} + m_a^*, \tag{7.8}$$

and $g^*(\boldsymbol{R})$ determined correspondingly by Equation (7.4).

7.3. Determination of α_R - averaged and local

Breaking the spin degeneracy allows us to probe the strength of the spin-orbit coupling. For $B > 3\,\mathrm{T}$, the spin states are distinguished in STS measurements. To extract the Rashba parameter, the contribution of Zeeman and spin-orbit splitting has to be separated. This can be done by evaluating the beating pattern evolving in spatially averaged $\mathrm{d}I/\mathrm{d}V$ curves, or locally by looking at the LL development at varying magnetic fields (see Section 5.3). Differential conductance measurements at five different positions (Figure 7.8), show a shifting of LL_0 as expected from the potential disorder (see Section 7.2.1). Moreover, the splitting of LL_0 ΔE_{SS} enhances with increasing V_{2D}. A similar trend can be seen in the data of Becker et al. [107] (Figure 6.9(g)) and might be connected to local changes in the spin-orbit coupling. For higher LL the behaviour becomes more complex, as multiple peak structures appear for LL_1. The changing between two and four peaks will be discussed in Section 7.5.

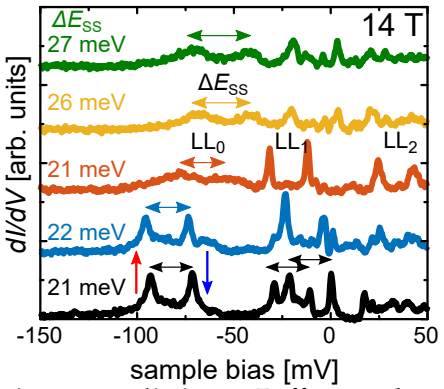

Figure 7.8.: Spatially varying LL splitting – Differential conductance recorded at five different positions each being about 5 nm apart ($V_{stab} = 300\,\mathrm{mV}$, $I_{stab} = 200\,\mathrm{pA}$, $V_{mod} = 0.7\,\mathrm{mV}$, $T = 400\,\mathrm{mK}$, $B = 14\,\mathrm{T}$). The horizontal arrows indicate the spin splitting ΔE_{SS} as labelled at the left of LL_0 and the partially four-fold splitting of LL_1. The vertical arrows mark the spin direction of the corresponding peaks of LL_0.

The clarity of the spin splitting of LL_0 also varies with position. This can be

accounted to an influence of the potential disorder as described in Section 5.3.1. Spectra around potential minima appear to show a clear spin splitting with peak widths of about 6 meV. At areas of larger gradients, the peaks are widened. Around potential maxima, the splitting is observable, but unexpectedly not as sharp as around the minima.

7.3.1. $\overline{\alpha_R}$ by beating pattern

Figure 7.9(a) shows the DOS by spatially averaging the differential conductance over a $250 \times 250\,\mathrm{nm}^2$ large area (Figure 7.9(b)) obtained at $B = 0\,\mathrm{T}$ (bottom) and for $B = 7\,\mathrm{T}$ (top). The onset of the first and second subbands can be identified at around $E_0 = -105\,\mathrm{meV}$ and $E_1 = 80\,\mathrm{meV}$, respectively. The dip around the Fermi energy arises from electron-electron interaction and can be identified as a Coulomb gap [149, 86, 150, 145], which has been studied previously on n-type InSb in detail [145]. Figure 7.9(c) shows a comparison of the found beating with three calculated densities of states using Equation (6.10) and using the mean effective mass $m^* = 0.03 \cdot m_0$ mapped in Section 7.2.3 and $g^* = -21$ correspondingly (Equation (7.4)), a Gaussian broadening $\Gamma = 20\,\mathrm{meV}$, found as the full width at half maximum of the potential disorder $V(\boldsymbol{R})$ (Section 7.2.1) and $\overline{\alpha_R} = 0.6, 0.7, 0.8\,\mathrm{eV\AA}$. Only the lowest subband was considered. The beating pattern with $\overline{\alpha_R} = 0.7\,\mathrm{eV\AA}$ shows the best agreement with the antinode of the found beating pattern around E_F, which is in agreement with previous results. The computed DOS and the experiment exhibit significant discrepancies. These are attributed to the non-parabolicity of InSb, resulting in a beating frequency that changes with energy (see Section 7.2.2).

7.3.2. LL crossing

In a small sample area, or at a single position, the LDOS does not exhibit any beating pattern since the spin contributions of the Zeeman and Rashba terms is resolved directly. In Section 5.2.1 the LL development with B is discussed when spin-orbit interaction plays a role, using the Bychkov-Rashba model (Equation (5.10)). A crossing of LLs is expected when Rashba energy and Zeeman energy get similar. In single-point STS obtained at different magnetic fields from $B = 0\,\mathrm{T}$ to $B = 14\,\mathrm{T}$, such crossings are indeed discernible as marked (Figure 7.10(a)). Moreover, the levels undulate collectively with B, which is ascribed to an undulation of the LLs with respect to the Fermi energy, to maintain a constant carrier density n. For higher magnetic fields exchange enhancement [145] also effects the LLs. At a few distinct magnetic fields the spectroscopy is reproducibly unstable. At fields close to local integer filling factors (marked

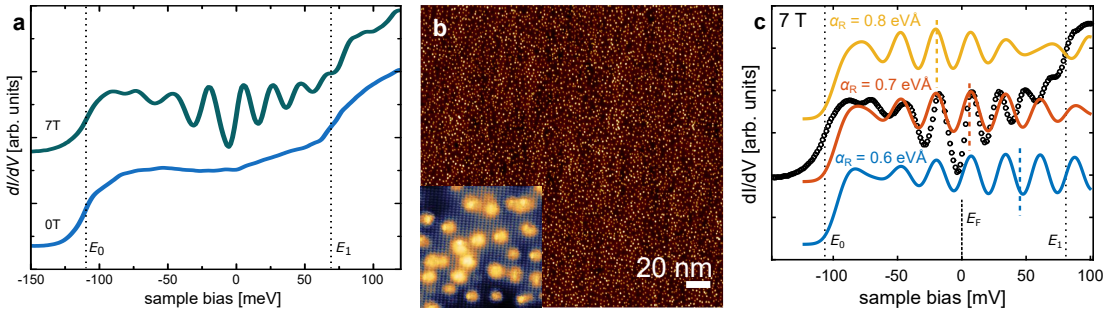

Figure 7.9.: Beating pattern of the LL and Rashba splitting – (a) Spatially averaged $\mathrm{d}I/\mathrm{d}V$ spectroscopy taken at $B = 0\,\mathrm{T}$ (bottom) & $B = 7\,\mathrm{T}$ (top) ($V_{\mathrm{stab}} = 300\,\mathrm{mV}$, $I_{\mathrm{stab}} = 0.2\,\mathrm{nA}$, $T = 400\,\mathrm{mK}$, 35×35 spectra, $250 \times 250\,\mathrm{nm}^2$). (b) Corresponding topography image ($V = 300\,\mathrm{mV}$, $I = 30\,\mathrm{pA}$, $250 \times 250\,\mathrm{nm}^2$). Inset: STM-image with atomic resolution of In-atom lines projected on the surface, with Cs on top (bright dots) ($V = 300\,\mathrm{mV}$, $I = 30\,\mathrm{pA}$, $T = 8\,\mathrm{K}$, $20 \times 20\,\mathrm{nm}^2$). (c) Observed $\mathrm{d}I/\mathrm{d}V$ curve (black circles) compared with DOS calculated using constant $m^* = 0.03 \cdot m_0$, $g^* = -21$ and different $\overline{\alpha_{\mathrm{R}}} = 0.6, 0.7, 0.8\,\mathrm{eV\AA}$ as marked. Dotted lines mark subband onset energies E_0, and E_1 as revealed from the measured curve at $B = 0\,\mathrm{T}$.

on top), the conductance at E_{F} drops down to $\approx 3\,\mathrm{pS}$ and the sample becomes insulating. The junctions inability to carry a current results in instabilities in the spectroscopy. Around E_{F} a slight suppression of LDOS is present, which is connected to the previously observed Coulomb gap [145, 151].
Multiple crossings of LLs are present, of which three are enlarged (marked I-III). The dashed lines outline the LL development and reveal a crossing away from $B = 0\,\mathrm{T}$. For LLs $\varepsilon_{1,-}$ and $\varepsilon_{3,+}$ ($\varepsilon_{2,-}$ and $\varepsilon_{4,+}$, $\varepsilon_{3,-}$ and $\varepsilon_{5,+}$), the crossing appears around $B = 4\,\mathrm{T}$ ($B = 6\,\mathrm{T}$, $B = 7\,\mathrm{T}$). The resolution prohibits a clear discrimination between crossing and anti-crossing. At lower magnetic fields and around the Fermi energy a whole set of indicated crossings is visible. Here the sharp peak structures due to the long hole life-time make it easier to distinguish between the different LLs. Nevertheless, it is not possible to clearly identify the absolute LL affiliation of those states. Those crossings can be naturally explained by the Rashba effect, even though they do not appear at the same B as in the calculations (Figure 5.2(b)). The discrepancies, in particlar, close to $B = 0\,\mathrm{T}$ most likely arise from the local confinement within the potential minimum (see Section 7.2.3), which is also visible from the set of horizontal lines in Figure 7.10(a) of $B < 2\,\mathrm{T}$. An accurate determination of $\alpha_{\mathrm{R}}(\boldsymbol{R})$ is further hampered by the non-parabolcity which is not considered in Equation (5.10) and becomes manifest, e.g. in $\Delta E_{\mathrm{LL0-LL1}} \neq \Delta E_{\mathrm{LL1-LL2}}$ towards higher B as visible by naked eye in Figure 7.10(a).

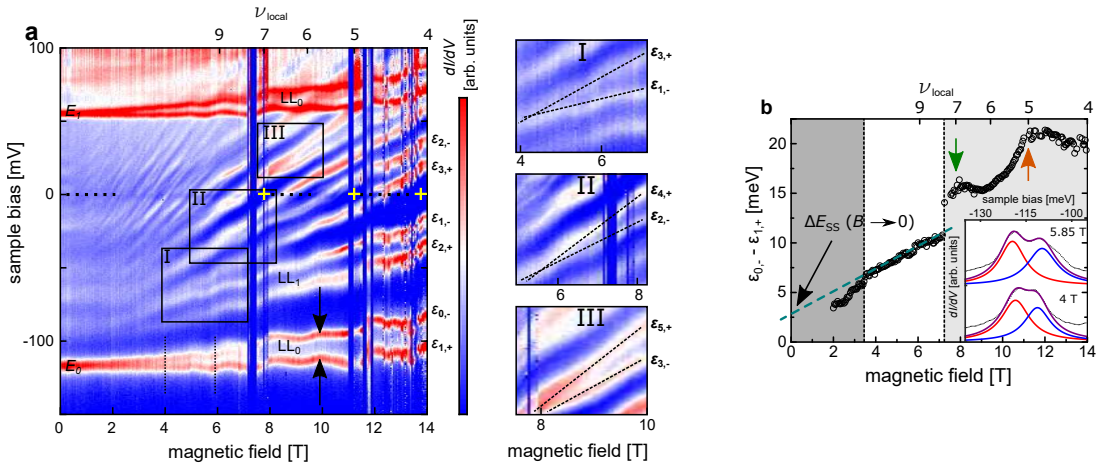

Figure 7.10.: LL development in magnetic field – (a) Measured LDOS at a single position within a potential minimum at different energies and B ($V_{stab} = 50\,\mathrm{mV}$, $I_{stab} = 100\,\mathrm{pA}$, $V_{mod} = 0.75\,\mathrm{mV}$, $T = 7.5\,\mathrm{K}$). The low-energy Landau levels of the lowest subband E_0 and the first subband E_1 are marked LL$_n$. The local filling factor ν_{local} (marked on top) is determined by counting the LL below E_F. Yellow crosses mark integer filling factors around which the spectroscopy becomes unstable due to low sample conductance. Black arrows mark the two spin levels of LL$_0$ evaluated in (b). Right hand side shows zooms into main images as marked with dashed lines (guides to the eye) highlighting the crossing away from $B = 0\,\mathrm{T}$. (b) Energy difference between the two lowest energy levels marked by black arrows in (a). The dashed line is a linear extrapolation of the slope between $B = 3.4\,\mathrm{T}$ and $B = 7.2\,\mathrm{T}$ towards $B = 0$. The green and orange arrows indicate $\nu_{local} = 5$ and $\nu_{local} = 7$, respectively. Inset: $\mathrm{d}I/\mathrm{d}V$ curves from low energy section at two fixed magnetic fields (black dots). The violet line shows a double line fit, consisting of two Lorentzians (red, blue) to extract the energy splitting.

7.3.3. $\alpha_R(R)$ by offset splitting $\Delta E_{SS}(B = 0\,\mathrm{T})$

The non-linearity of the LL$_0$ spin splitting $\Delta E_{SS}(B, \boldsymbol{R})$ appears to be more eligible for an analysis of the local spin-orbit coupling. Fitting of a double Lorentzian to LL$_0$ (Figure 7.10(b)) shows three different regions for the dependency of the LL$_0$ splitting on B. At high magnetic fields, above $B = 7\,\mathrm{T}$, ΔE_{SS} shows an oscillation. The maxima are located at odd local filling factors, as expected for exchange enhancement [152, 145]. The exchange interaction depends exponentially on the overlap of the wave functions, scaling with $l_B \propto \sqrt{1/B}$. For lower fields, it decays rapidly and is for $B < 6\,\mathrm{T}$ below 1 meV [145]. Thus, it can be neglected for $B \lesssim 6\,\mathrm{T}$, where it is smaller than the accuracy of the determination of the spin splitting in our experiment. Indeed, it is not observable for the region $B = 3 - 7\,\mathrm{T}$ and instead ΔE_{SS} depends largely linearly on B. Towards $B = 0\,\mathrm{T}$, the decay of ΔE_{SS}^0 becomes faster than linear and marks the region $B < 3\,\mathrm{T}$.

The linear segment is extrapolated towards $B = 0\,\mathrm{T}$ and reveals an offset of $\Delta E_{\mathrm{SS}}^{0} \approx 2.5\,\mathrm{meV}$. Equation (5.13) is resulting in $\alpha_{\mathrm{R}}(\boldsymbol{R}) = 0.65\,\mathrm{eV\AA}$ for $m^* = 0.03 m_{\mathrm{e}}$ and $g^* = -21$, which is very close to the laterally averaged $\overline{\alpha_{\mathrm{R}}} = 0.7\,\mathrm{eV\AA}$ extracted by the beating pattern. Using Equation (5.18), assuming a constant 2D potential $V_{\mathrm{2D}}(\boldsymbol{R})$, so that $\mathrm{V}_{\mathrm{2D},n}(\boldsymbol{R}) = \mathrm{V}_{\mathrm{2D},n-1}(\boldsymbol{R})$, gives the same result.
Following the peak widths $\sigma_{\varepsilon_{1,+}}$ and $\sigma_{\varepsilon_{0,-}}$ towards high magnetic fields shows that, while $\sigma_{\varepsilon_{1,+}}$ appears to be constantly 6 meV, $\sigma_{\varepsilon_{1,+}}$ narrows to 3 meV. As previously mentioned, the width of the peaks is not limited by the resolution of the experiment (T, V_{mod}) but by the life-time of the electron holes being approximately proportional to $(E - E_{\mathrm{F}})^{-2}$ [153]. $\varepsilon_{1,+}$ remains almost constant in energy for increasing magnetic field, while $\varepsilon_{0,-}$ shifts towards E_{F}. The distance of $\varepsilon_{1,+}$ to E_{F} is fixed due to the constant carrier density $n = 1.5 \times 10^{16}\,\mathrm{m}^{-2}$. With increasing magnetic field and degeneracy, less states are between E_{F} and $\varepsilon_{0,-}$ increasing the hole life-time and narrowing the width of $\varepsilon_{1,+}$. As a result the very sharp peaks of higher LLs around E_{F} appear with widths of V_{mod}. The presence of the Coulomb gap enhances this narrowing effect for levels directly at the Fermi level.

7.3.4. $\alpha_{\mathrm{R}}(R)$ by fitting Rashba model

An approach that allows us to take the contribution of the 2D potential on ΔE_{SS} into account is the model of Pérez et al. (Section 5.3.1). While the non-linearity, observed at $B < 3\,\mathrm{T}$, is already implied by the Bychkov-Rashba Equation (5.10), effects of the potential disorder that shift different LL wave function in energy are also included by the effective potential terms $V_{\mathrm{2D},n}$. Figure 7.11(a) shows two LL-fans for different potential minima. The spin splitting ΔE_{SS} (Figure 7.11) observed at those two positions is fitted with Equation (5.18). To fit ΔE_{SS}, the g-factor and effective mass are determined using the LL splitting between LL_0 and LL_1 extracted from the same LL-fans (see Section 7.2.3). This leaves α_{R} as the only fit parameter.
This type of fits reveals a large spatial fluctuation of the spin-orbit coupling ($\alpha_{\mathrm{R}} = 0.5\,\mathrm{eV\AA} - 1.1\,\mathrm{eV\AA}$). A spatial fluctuation of g^* can be easily ruled out as an origin for the fluctuations of the splitting. The curve probed at $V_{\mathrm{2D}}(\boldsymbol{R}) = -121\,\mathrm{meV}$ (black) should have a larger g-factor than the one probed at $V_{\mathrm{2D}}(\boldsymbol{R}) = -101\,\mathrm{meV}$ (red), which is in contradiction with the experimental observation, showing the smaller splitting for $V_{\mathrm{2D}}(\boldsymbol{R}) = -121\,\mathrm{meV}$ (black). The exchange enhancement, which is below 1 meV at $B < 6\,\mathrm{T}$, does not explain the difference either.

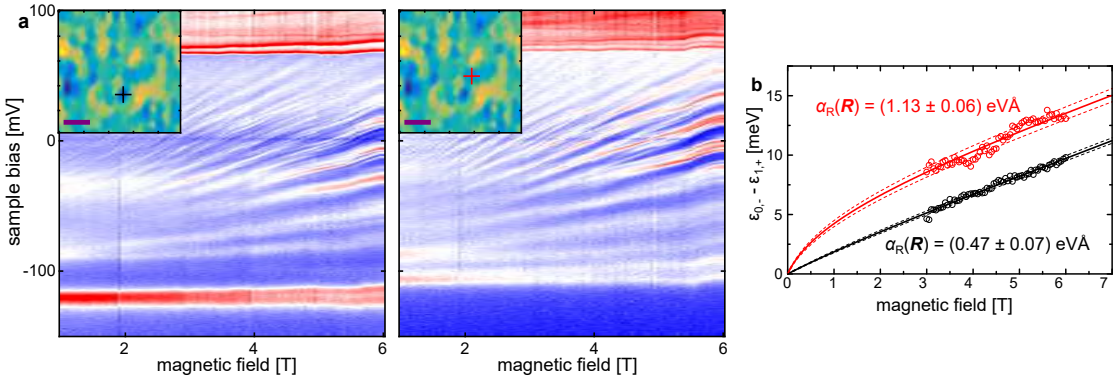

Figure 7.11.: Rashba parameter locally extracted by *B*-field dependence of LL – (a) $\mathrm{d}I/\mathrm{d}V(V,B)$ spectra measured at two potential minima. (Both: $V_{\mathrm{stab}} = 50\,\mathrm{mV}$, $I_{\mathrm{stab}} = 100\,\mathrm{pA}$, $V_{\mathrm{mod}} = 0.75\,\mathrm{mV}$, $T = 400\,\mathrm{mK}$). Inset: potential map marking the position where the spectra have been taken (cf. Figure 7.3(b)). Scale bar: 50 nm (b) Circles: LL_0 splitting determined between 3 T and 6 T at the position marked in the insets of (a) by crosses. Full lines: fit according to the Rashba model by Pérez et al. [102] (Equation (5.18)) with resulting fit parameter $\alpha_R(\boldsymbol{R})$ marked. Dashed lines: 65 % confidence interval of the fits with corresponding $\pm\Delta\alpha_R(\boldsymbol{R})$ marked.

7.4. Mapping of $\alpha_R(R)$

By having the possibility to extract $\alpha_R(\boldsymbol{R})$ from the splitting energy ΔE_{SS}, mapping of the Rashba parameter is possible. Using Equation (5.18) requires knowledge of the 2D potential (see Section 7.2.1) as well as of m^* and g^*. Figure 7.12(a) shows the LL_0 splitting ΔE_{SS} across the area of the potential map for $B = 6\,\mathrm{T}$ and Figure 7.12(b) the resulting map for $\alpha_R(\boldsymbol{R})$, using the effective potentials from Figure 7.4. Fluctuations of the Rashba parameter ($\alpha_R(\boldsymbol{R}) = 0.4 - 1.6\,\mathrm{eVÅ}$) range up to a factor of four. The mapped area exhibits on average a giant Rashba parameter of $\overline{\alpha_R}(\boldsymbol{R}) = 1.2\,\mathrm{eVÅ}$, with a root mean square variation of $\delta\overline{\alpha_R}(\boldsymbol{R}) = 0.15\,\mathrm{eVÅ}$. Naturally, the variations in $\alpha_R(\boldsymbol{R})$ are mainly reflected in the map of the spin splitting, but the contributions of extended wave functions obviously have to be taken into account. A spatial variation of the Rashba parameter is expected due to changes in the electric field. In Equation (5.18), the spin splitting also exhibits a direct contribution of the 2D potential, resulting from the different contributing LL wave functions. Thus, a strong correlation between $\alpha_R(\boldsymbol{R})$ and V_{2D} is to be expected. While strong features of the potential disorder, e.g. the potential valley around the black cross, can be found in ΔE_{SS} and $\alpha_R(\boldsymbol{R})$ as well (cf. Figures 7.12(a) & 7.12(b)), there are also obvious deviations.
While the *E*-field, causing α_R, is not accessible using STS, the electrostatic po-

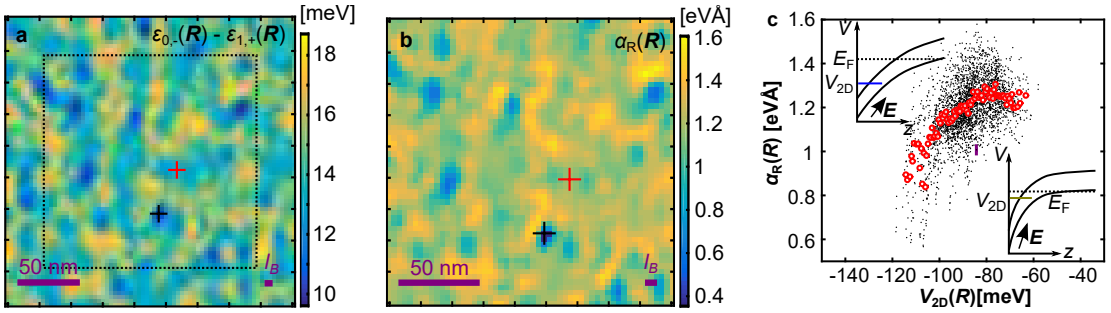

Figure 7.12.: Spatially resolved $\alpha_R(R)$ – (a) LL_0 splitting (ΔE_{SS}) map at $B = 6\,T$. Smoothed with a Gaussian of width l_B. Black dotted square indicates area shown in b. Red and blue crosses refer to curves in Figure 7.11(b), using same colour. (b) Spatially resolved Rashba parameter $\alpha_R(R)$, using Equation (5.18), ΔE_{SS} shown in (a), the 2D potential (Figure 7.3(b)) and $m^*(R)$ & $g^*(R)$ (Equation (7.8)). (c) Black dots: $\alpha_R(R)$ from (a) plotted as a function of $V_{2D}(R)$ from Figure 7.3(b). Red circles: Rashba parameter averaged across a V_{2D} interval of 0.5 meV. Purple error bar indicates a typical error bar of $\alpha_R(R)$ and $V_{2D}(R)$, showing that the scatter of α_R is significantly larger than the error bars. Insets: sketch of band bending at lateral position (x, y) low (top left) and high (bottom right) local acceptor density. The coloured lines mark $V_{2D}(x, y)$.

tential can be probed. Comparing the measured $\alpha_R(R)$ with the corresponding $V_{2D}(R)$ (Figure 7.12(c)) reveals a weak monotonic relation. By averaging $\alpha_R(R)$ that correspond with the same V_{2D} (red circles), the correlation becomes nearly linear. The relation becomes understandable by the insets in Figure 7.12(c). While the potential is fixed at the surface by the large Cs density, different E-fields are related to different local potentials $V_{2D}(x, y) \approx \int V_{3D}(x, y, z) \cdot |\Psi_0(z)|^2 dz$, using $|\Psi_0(z)|^2$ of Equation (5.27). A large (small) E implies a large (small) potential rise within length b, leading to large (small) V_{2D}.

The scattering in Figure 7.12(c) cannot be explained by the accuracy of the determination of $\alpha_R(R)$ within this method, since the error bar (purple) is much smaller. This error on $\alpha_R(R)$ is determined by Gaussian error propagation containing the statistical errors on the peak fittings of $\varepsilon_{n,\pm}$ leading to errors of g^*, m^*, V_{2D} and ΔE_{SS}. The discrepancies will be explained in Section 7.4.2. A discussion of the statistical and systematic errors on $\alpha_R(R)$ is done in Section 7.4.5. Notably, the correlation length $l_{\alpha_R\alpha_R} = 31\,nm$, extracted from $\langle \alpha_R | \alpha_R \rangle$ (Figure 7.13), is larger than l_B, thus, the resolution of the variations is not limited by the applied magnetic field. At the same time $l_{\alpha_R\alpha_R}$ is shorter than the correlation length of the potential $l_{V_{2D}V_{2D}} = 49\,nm$. The cross-correlation of $\alpha_R(R)$ and $V_{2D}(R)$ (Figure 7.13(b)) also shows 60 % correlation, leaving the question of the origin of the $\alpha_R(R)$ variations open. A fit-free model, introduced in Sec-

tion 5.3.2, suggests for this system a spin-orbit fluctuation of $\delta\alpha_R \approx 0.25\,\text{eVÅ}$ for both types of dopants, the Cs adatoms and the Ge bulk dopants, which agrees very well with the observed variations. The variations in the electric field, on which $\alpha_R(\boldsymbol{R})$ relies, lead to correlation lengths of the α_R fluctuation of $L_{\alpha_R\alpha_R,2D} = 28\,\text{nm}$ and $L_{\alpha_R\alpha_R,3D} = 11\,\text{nm}$. Additionally smeared out with the magnetic length l_B, this represents the measured $l_{\alpha\alpha}$ roughly. To exclude other possible origins of the $\alpha_R(\boldsymbol{R})$ fluctuations, contributions of lateral $\boldsymbol{E}$-field and curvature of the potential are investigated next.

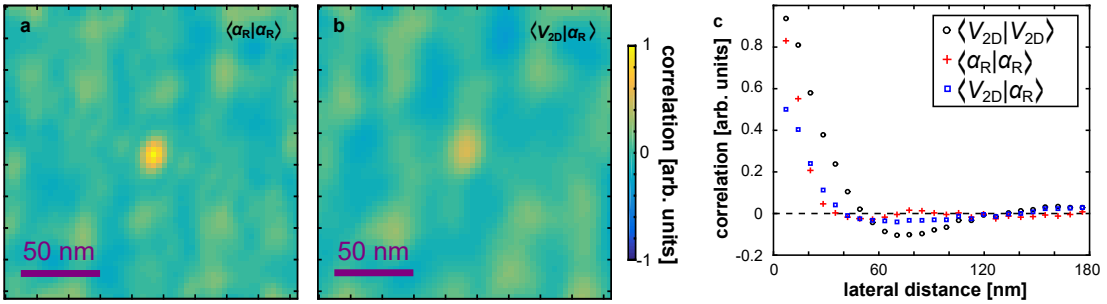

Figure 7.13.: Correlation and correlation length of $\alpha_R(\boldsymbol{R})$ and $V_{2D}(\boldsymbol{R})$ – (a) Autocorrelation of the $\alpha_R(\boldsymbol{R})$-map shown in Figure 7.12(b). (b) Cross-correlation between the $\alpha_R(\boldsymbol{R})$-map and $V_{2D}(\boldsymbol{R})$-map (centre of Figure 7.3(b)). The cross-correlation is normed, so that a perfect cross-correlation would yield a value of 1, corresponding to an autocorrelation. (c) Angular average of panels (a) (red crosses), (b) (blue squares) and Figure 7.3(c) (black circles). The zero-crossings give: $S_{V_{2D}V_{2D}} = 50\,\text{nm}$, $S_{\alpha_R\alpha_R} = 40\,\text{nm}$ and $S_{V_{2D}\alpha_R} = 40\,\text{nm}$. Fitting of a Gaussian curve $f_{AB}(x)$, with $f_{AB}(0) = 1$, with the Gaussian width σ_{AB} as the only free parameter results in $\sigma_{V_{2D}V_{2D}} = (20.1 \pm 0.7)\,\text{nm}$, $\sigma_{\alpha_R\alpha_R} = (12.2 \pm 0.2)\,\text{nm}$, $\sigma_{V_{2D}\alpha_R} = (16.0 \pm 0.5)\,\text{nm}$, and correlation lengths $l_{V_{2D}V_{2D}} = 49\,\text{nm}$ and $l_{\alpha_R\alpha_R} = 31\,\text{nm}$ according to Equation (5.32).

7.4.1. Correlation of $\alpha_R(\boldsymbol{R})$ with lateral gradient and curvature of the electrostatic potential $V_{2D}(\boldsymbol{R})$

Besides the electrostatic potential, which leads to a monotonous increase of $\alpha_R(\boldsymbol{R})$, as explained by the relation between potential and vertical electric field, the lateral electric field $\boldsymbol{E}_{xy}$ could also affect the spin-orbit coupling. This electric field $\boldsymbol{E}_{xy}$, present due to the potential disorder, is the lateral gradient of the local potential $\nabla V_{2D}(\boldsymbol{R})$.
Figure 7.14(a) shows the absence of a correlation between $\alpha_R(\boldsymbol{R})$ and $|\boldsymbol{E}_{xy}|$. The lateral electric field therefore has negligible influence on the Rashba parameter, which is reasonable, since $|\boldsymbol{E}_{xy}| \approx 0 - 3\,\text{mV/nm}$ is about an order of magnitude smaller than the vertical electric fields $|\boldsymbol{E}_z| \approx 30\,\text{mV/nm}$. In contrast, the

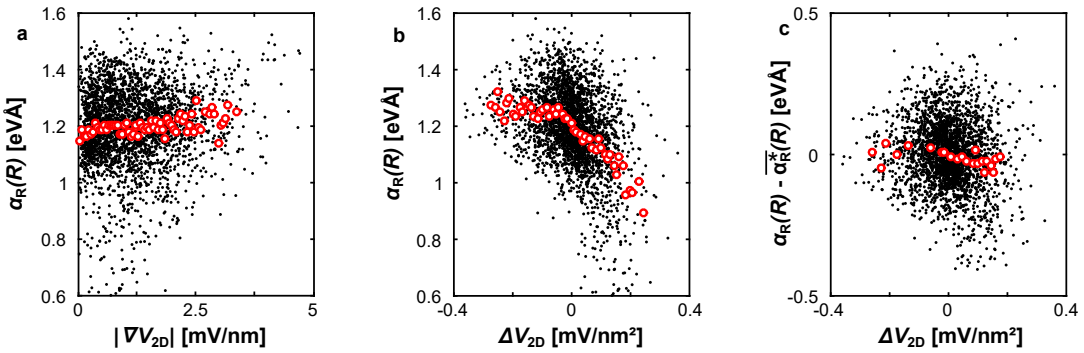

Figure 7.14.: Correlation of lateral gradient and curvature of the electrostatic potential with the Rashba parameter – (a) Correlation between the lateral electric field $|\boldsymbol{E}_{xy}|$ and $\alpha_R(\boldsymbol{R})$. (b) Correlation between the curvature of the 2D potential ΔV_{2D} and $\alpha_R(\boldsymbol{R})$. (c) Correlation between lateral curvature and local Rashba parameter after subtracting the potential contribution (see text).

curvature of the potential appears to anti-correlate with the Rashba parameter (Figure 7.14(b)). This can be explained by the fact that the curvature itself shows some correlation with the potential. Potential minima (maxima) show large positive (negative) curvature. In order to disentangle this indirect effect between curvature and $\alpha_R(\boldsymbol{R})$ from the direct influence of the curvature, the average value of α_R, $\overline{\alpha_R^*}$ found for the particular $V_{2D}(\boldsymbol{R})$ (red dots in Figure 7.12(c)) is subtracted from the measured $\alpha_R(\boldsymbol{R})$. The resulting scatter plot is shown in Figure 7.14(c). The previous anti-correlation obviously disappears.

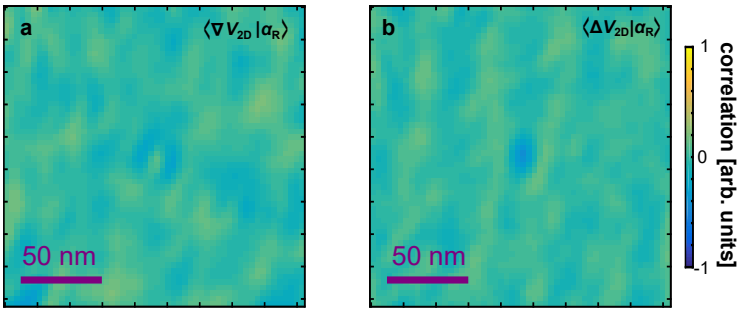

Figure 7.15.: 2D correlation of $\alpha_R(\boldsymbol{R})$, $|\nabla V_{2D}|$ and ΔV_{2D} – (a) Cross-correlation between the $\alpha_R(\boldsymbol{R})$-map (Figure 7.12(b)) and the lateral gradient of $V_{2D}(\boldsymbol{R})$ (Figure 7.3(b) - same area). (b) Cross-correlation between the $\alpha_R(\boldsymbol{R})$-map and the curvature of $V_{2D}(\boldsymbol{R})$ (same area). The lateral electric field does not show significant correlation. An anti-correlation is observed between $\alpha_R(\boldsymbol{R})$ and the curvature of V_{2D}, which can be attributed to $\langle \alpha_R | V_{2D} \rangle$ (see Figure 7.14(c)).

The cross-correlations of $|\boldsymbol{E}_{xy}(\boldsymbol{R})|$ and $\Delta V_{2D}(\boldsymbol{R})$ with $\alpha_R(\boldsymbol{R})$ in Figure 7.15 ex-

hibit rather weak features, showing negligible contribution to variations of the spin-orbit coupling. Therefore, as expected, neither the small lateral electric field nor the lateral potential curvature influence the Rashba effect significantly. This leaves the spatially fluctuating $\boldsymbol{E}$-field perpendicular to the surface as the central influence on the variable Rashba parameter $\alpha_R(\boldsymbol{R})$.

7.4.2. Origin of potential fluctuations

The sample exhibits two types of doping. Positively charged Cs atoms are positioned at the surface with an average distance of about 4 nm. They are screened by negatively charged Ge acceptors with density $n_{Ge} = 10^{24}\,\mathrm{m}^{-3}$, i.e. relative distance of 10 nm, randomly distributed within the bulk of the InSb sample.
In order to discriminate between the influence of the two different dopants on the potential disorder $V_{2D}(\boldsymbol{R})$ within the 2DES, a simple numerical model is applied. It uses only two directions, one perpendicular and one parallel to the surface. Positively charged Cs atoms, which are distributed on the surface, are compensated by randomly distributed negatively charged acceptors within the bulk. The surface dopants are placed in a fixed distance of 4 nm as shown in Figure 7.16(a). The regular distance reflects the fact that only about 50 % of the dopants are charged, such that the charge has an additional degree of freedom to arrange regularly on the surface. Moreover, the distance between Cs atoms is smaller than the effective Bohr-Radius $a_B \approx 14\,\mathrm{nm}$ for the dielectric constant $\epsilon_r = 0.5 \cdot \epsilon_{r,InSb} = 8.4$ of the surface [106] and $m^* \approx 0.03 \cdot m_e$ of the InSb conduction band, such that neighbouring band electrons strongly overlap and can hop easily in order to screen charges effectively. Consequently, the remaining electrons within the Cs layer form a rather homogeneous band, which screens the positive Cs charges and reduces irregularities additionally. Experimentally, no influences of the spatial distribution of the Cs atoms on the measured potential $V_{2D}(\boldsymbol{R})$ can be found [143]. Figure 7.16(b) shows the random distribution of negatively charged acceptors (red dots) within the bulk with a density of $10^{24}\,\mathrm{m}^{-3}$, which corresponds to the experimental acceptor density.
The Coulomb potentials of the positive and negative charges within a plane, which is offset by 5 nm from the plane where the acceptors and surface donors are placed, are simply added up. This approximates the average situation of potential fluctuations within a 3D material by distancing the measurement plane by about half the inter-acceptor distance from the acceptor plane. As dielectric constants, we use $\epsilon_r = \epsilon_{r,InSb} = 16.8$ for the negative charges [106], and $\epsilon_r = 0.5 \cdot \epsilon_{r,InSb}$ for the positive charges. The latter choice reflects that the Cs atoms are surrounded by vacuum in the upper half-space. Screening by conduction band or valence band electrons is ignored for the sake of simplicity.

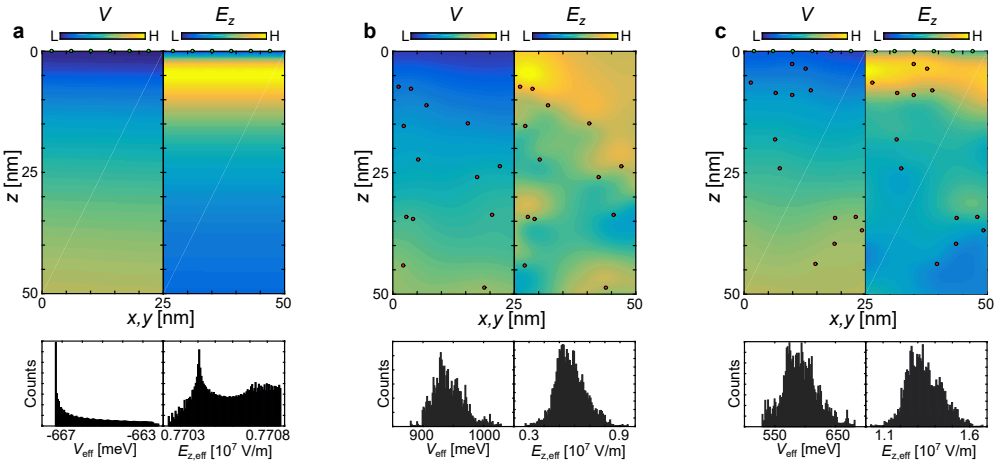

Figure 7.16.: Influence of different doping on V_{eff} and $E_{z,\mathrm{eff}}$ – Top: electrostatic potential $V(\boldsymbol{R})$ (left) and electric field in z-direction $E_z(\boldsymbol{R})$ (right) for three different doping distributions shown in (a), (b) and (c). Simulated area is larger than the displayed area ($x = 150\,\mathrm{nm}$, $z = 100\,\mathrm{nm}$). Bottom: corresponding histograms from 20 simulation runs of the potential $V_{\mathrm{eff}}(\boldsymbol{R})$ and electric field $E_{z,\mathrm{eff}}(\boldsymbol{R})$ after weighting the simulated $V(\boldsymbol{R})$ and $E_z(\boldsymbol{R})$ with the wave function of the 2DES in z direction. (a) Resulting from positively charged surface donors with density $n_{\mathrm{Cs}} = 0.25\,\mathrm{nm}^{-1}$ (green dots) (b) Randomly distributed negatively charged bulk acceptors (red dots) with density $n_{Ge} = \left(10^{24}\,\mathrm{m}^{-3}\right)^{2/3}$. (c) Combination of both dopants in (a) and (b), representing the experimental setup. The variations of V_{eff} and $E_{z,\mathrm{eff}}$ are obviously mostly caused by the bulk acceptors and barely by the Cs donors at the surface.

The total simulated area has a size of $150 \times 100\,\mathrm{nm}$. To avoid boundary effects, only the central area of the simulation is evaluated. The resulting electrostatic potential $V(\boldsymbol{R})$ and the corresponding electric field in z-direction $E_z(\boldsymbol{R})$ of the inner part of the simulation grid are shown for a single simulation run in Figure 7.16(c). Both electric field and potential have been convolved with the electron probability density of the lowest subband of a triangular potential well [154] adapted to the result of the Poisson calculation [107] leading to a maximum of $|\Psi_0(z)|^2$ located at $z_0 = 5\,\mathrm{nm}$. The convolution leads to an effective electric field $E_{z,\mathrm{eff}}(\boldsymbol{R})$ seen by the 2DES and an effective 2DES potential $V_{\mathrm{eff}}(\boldsymbol{R})$. This potential can be identified with the V_{2D} found in the experiment. The fluctuations of $E_{z,\mathrm{eff}}$ with respect to its average barely depend on the spatial details of the dielectric constant and, thus, the dielectric constant has been considered as constant in the simulation.
In each simulation run, five equidistant positions $\boldsymbol{R}$ within the inner 50 nm of the measurement plane are used for the statistical evaluation. Potential and electric field are calculated for three different cases, i.e. pure Cs doping at the

surface without Ge acceptors (Figure 7.16(a)), pure bulk doping by Ge acceptors without surface doping by Cs (Figure 7.16(b)), and the presence of both types of dopants (Figure 7.16(c)). For all three cases, 20 simulations with different dopant positions are run. In the case of pure Cs doping, the 2DES potential V_{eff} fluctuates with a standard deviation of $\sigma_{V_{\text{eff}}} = 1.5\,\text{meV}$ (Figure 7.16(a) bottom). In contrast, the bulk dopants lead to a fluctuation with standard deviation of $\sigma_{V_{\text{eff}}} = 26\,\text{meV}$ (Figure 7.16(b) bottom). Combining both dopants reveals a fluctuation of $\sigma_{V_{\text{eff}}} = 29\,\text{meV}$ (Figure 7.16(c) bottom). The fluctuation is obviously dominated by the bulk dopants and not by the Cs atoms. The potential fluctuations in the experiment with standard deviation $\sigma_{V_{2D}(\boldsymbol{R})} = 11\,\text{meV}$ are smaller probably due to the fact that, firstly, the probability of bulk acceptor charging is correlated with the Cs potential on top and, secondly, the 2DES screens the potential fluctuations additionally.
The much smaller contribution of the Cs atoms can be explained, firstly, by the smaller mean distance of 4 nm between neighbouring Cs atoms compared to a mean distance of 10 nm between adjacent bulk dopants, and secondly, by the fact that all Cs atoms are 5 nm away from the centre of the wave function of the 2DES, while the Ge atoms can be directly at the wave function centre. Finally, the reduced dimensionality of the Cs layer (2D) with respect to the bulk acceptors (3D) reduces the potential fluctuations by the Cs atoms additionally, as cross-checked by corresponding simulations. This justifies the assumption of a spatially constant surface potential depicted in the insets of Figure 7.12(c). The 2D potential should therefore be an indicator for the strength of the $\boldsymbol{E}$-field in z direction as observed in Figure 7.12(c). This, however, still leaves the question for the origin of the relatively strong scatter between $V_{2D}(\boldsymbol{R})$ and $\alpha_R(\boldsymbol{R})$.

7.4.3. Relation between $V_{2D}(R)$ and $E_z(R)$

The monotonous increase in the averaged $\alpha_R(\boldsymbol{R})$ with $V_{2D}(\boldsymbol{R})$, exhibiting a scattering larger than the error bar of $\alpha_R(\boldsymbol{R})$, is related to the fact that the electric field $|\boldsymbol{E}(\boldsymbol{R})|$ is only indirectly represented by the measurable $V_{2D}(\boldsymbol{R})$. In order to estimate the correlation between electric field and potential, we use the simulation introduced in Section 7.4.2 (Figure 7.17(a)).
Figure 7.17(b) shows the scatter plot of $E_{z,\text{eff}}(\boldsymbol{R})$ and $V_{\text{eff}}(\boldsymbol{R})$ for 5 randomly chosen $\boldsymbol{R}$ positions within 500 simulation runs, each with different bulk dopant positions. According to the 2900 data point in the experiment shown in Figure 7.12(c), 2500 different $\boldsymbol{R}$ are evaluated. The expected linear dependency between averaged electric field and 2DES potential (red dots) is well represented in the simulation. $V_{2D}(\boldsymbol{R})$ depends on the local distribution of bulk acceptors being low at low local acceptor density and high at high local acceptor density

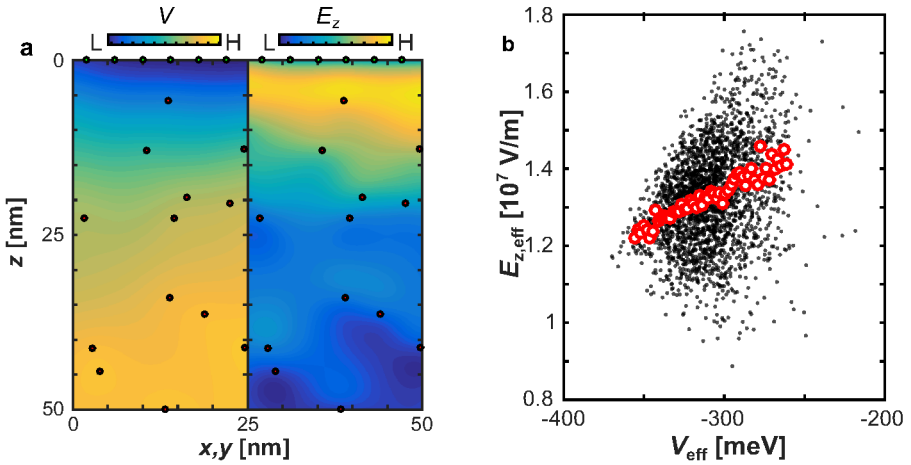

Figure 7.17.: Interplay between V_{2D} and $E_{z,\mathrm{eff}}$ – (a) Electrostatic potential $V(\boldsymbol{r})$ (left) and electric field in z-direction $E_z(\boldsymbol{r})$ (right) resulting from positively charged surface donors with density $n_{\mathrm{Cs}} = 0.25\,\mathrm{nm}^{-1}$ (green dots) and randomly distributed negatively charged bulk acceptors (red dots) with density $n_{Ge} = \left(10^{24}\,\mathrm{m}^{-3}\right)^{2/3}$. Simulated area is larger than the displayed one ($x = 150\,\mathrm{nm}, z = 100\,\mathrm{nm}$). Same simulation as in Figure 7.16(c). (b) Correlation between V_{eff} and $E_{z,\mathrm{eff}}$ for 2500 simulated different $\boldsymbol{R}$-positions (black dots) resulting from 500 simulations as displayed in (a). Red dots mark the average electric field $\overline{E}_{z,\mathrm{eff}}$ for a given V_{eff} within a 0.25 meV interval.

as expected. This explains the positive correlation between $V_{2D}(\boldsymbol{R})$ and $\alpha_R(\boldsymbol{R})$ found experimentally (Figure 7.12(c)). At the same time, a significant scattering of the data points is present as well in the simulation. The standard deviation of the found $E_{z,\mathrm{eff}}$ at a given V_{eff} is about 10 %, which nicely matches the standard deviation of the α_R values at a given V_{2D}. We therefore tentatively assign the observed large scatter of α_R (V_{2D}) to the unavoidable scatter of $E_{z,\mathrm{eff}}$ (V_{eff}) within a random potential. The absolute value of the effective electric field in our simplified 2D simulation ($\overline{E_{z,\mathrm{eff}}} = 1.3 \cdot 10^7\,\mathrm{V/m}$) is smaller than the electric field in z direction $E_z = 3.1 \cdot 10^7\,\mathrm{V/m}$ resulting from the Poisson-Schrödinger equation [107], which is probably due to the simplified 2D model, but that does not affect the general conclusion of the unavoidable scatter of $E_{z,\mathrm{eff}}$ (V_{eff}).

7.4.4. Relation between deduced ($V_{2D}(R)$, $\alpha_R(R)$) and measured quantities (($\varepsilon_{0,-} + \varepsilon_{1,+}$)/2, $\varepsilon_{0,-} - \varepsilon_{1,+}$)

The potential map $V_{2D}(\boldsymbol{R})$ and the map of the Rashba parameter $\alpha_R(\boldsymbol{R})$ are deduced from the energy values of the peaks attributed to the levels $\varepsilon_{0,-}$ and $\varepsilon_{1,+}$, according to Equation (5.18). The potentials $V_{2D,n}(\boldsymbol{R})$ ($V_{2D}(\boldsymbol{R})$ folded with the Landau level kernels) contribute as a difference inside the square root, as well

as an additive linear term, the average of the two contributing Landau levels. Calculating the average of $\varepsilon_{0,-}$ and $\varepsilon_{1,+}$, the square root term largely cancels out (error < 1 meV), such that one gets the average of the contributing $V_{2D,n}(\boldsymbol{R})$ (75 % $V_{2D,0}$, 25 % $V_{2D,1}$), which basically represent the original 2DES potential $V_{2D}(\boldsymbol{R})$ after spatially averaging by about the magnetic length l_B. In order to obtain the $\alpha_R(\boldsymbol{R})$ map, the equation of the difference $\varepsilon_{0,-} - \varepsilon_{1,+}$ is analytically solved for $\alpha_R(\boldsymbol{R})$.
In order to corroborate the assignments and to answer the question why the $\alpha_R(\boldsymbol{R})$ map shows more spatial details than the $V_{2D}(\boldsymbol{R})$ map, we use the simulation described in Section 7.4.2 to generate potentials $V_{eff}(\boldsymbol{R})$ (Figure 7.18(a)(i)) and electric fields $E_{z,eff}(\boldsymbol{R})$ (Figure 7.18(a)(ii)), as seen by the 2DES. $E_{z,eff}(\boldsymbol{R})$ is then transferred into a spatially varying Rashba parameter using $\alpha_R(\boldsymbol{R}) \propto E_{z,eff}(\boldsymbol{R})$ with $\alpha_R(\boldsymbol{R}) = 1.2\,\text{eVÅ}$ and $\delta\alpha_R(\boldsymbol{R}) = 0.15\,\text{eVÅ}$ as found in the experiment. With the help of $\alpha_R(\boldsymbol{R})$ and $V_{eff}(\boldsymbol{R})$, $\varepsilon_{0,-}(\boldsymbol{R})$ and $\varepsilon_{1,+}(\boldsymbol{R})$ are calculated according to Equation (5.18) using $B = 6\,\text{T}$, $m^* = 0.026 \cdot m_e$ and $g^* = -21$. The mean value of $\varepsilon_{0,-}(\boldsymbol{R})$ and $\varepsilon_{1,+}(\boldsymbol{R})$ plotted in Figure 7.18(a)(iv) indeed represents the slightly smoothed $V_{eff}(\boldsymbol{R})$, while the difference of $\varepsilon_{0,-}(\boldsymbol{R})$ and $\varepsilon_{1,+}(\boldsymbol{R})$ plotted in Figure 7.18(a)(v) mimics the course of $E_{z,eff}(\boldsymbol{R})$. With Figure 7.18(a)(iv) instead of the real potential of Figure 7.18(a)(i), we obtain the reconstructed $\alpha_R(\boldsymbol{R})$ map, which nearly perfectly matches the input $\alpha_R(\boldsymbol{R})$ map (Figure 7.18(a)(iii) & (vi)) (average deviation 1 %, maximum deviation 3 %). The auto-correlations averaged over 100 simulation cycles (Figure 7.18(b)) result in the following correlation lengths:

$$l_{V_{2D}V_{2D}} = 43\,\text{nm},\ l_{\alpha_R\alpha_R} = 32\,\text{nm},\ l_{\varepsilon_+\varepsilon_+} = 48\,\text{nm},\ l_{\varepsilon_-\varepsilon_-} = 30\,\text{nm}. \tag{7.9}$$

These are in excellent agreement with the experimentally found correlation lengths $l_{V_{2D}V_{2D}} = 49\,\text{nm}$ and $l_{\alpha_R\alpha_R} = 31\,\text{nm}$. However, it shall be noted that the absolute values of correlation lengths depend on the size of the simulated system as expected in a 1D simulation, but the relation between correlation length of electric field and potential remains the same.
Thus, the anticipated mapping of the average of the two peak energies to $V_{2D}(\boldsymbol{R})$, and the difference to $E_{z,eff}(\boldsymbol{R})$ and $\alpha_R(\boldsymbol{R})$, respectively, works almost perfectly within the limits of Equation (5.18) (average error: 1.5 %). The simulation also reproduces the smaller correlation length of $\alpha_R(\boldsymbol{R})$ with respect to $V_{2D}(\boldsymbol{R})$. Thus, the finer details of the $\alpha_R(\boldsymbol{R})$ map with respect to the $V_{2D}(\boldsymbol{R})$ map in Figure 7.12 can be attributed to the stronger relative gradient of an electric field of a Coulomb potential $\frac{\nabla \boldsymbol{E}}{\boldsymbol{E}} = \frac{2}{|\boldsymbol{R}|}$ with respect to the relative gradient of the electrostatic potential $\frac{\nabla V}{V} = \frac{1}{|\boldsymbol{R}|}$. In other words, randomly distributed Coulomb impurities within a semiconductor exhibit shorter-scale fluctuations in the electric field than in the electrostatic potential. The Rashba parameter,

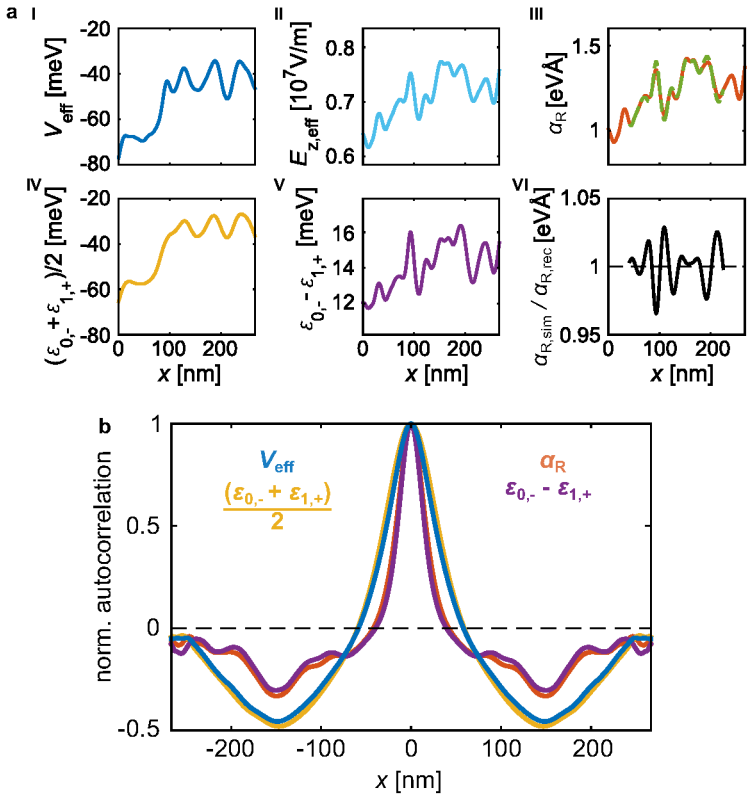

Figure 7.18.: Simulations for confirmation of the reliability of the determination of V_{2D} and α_R – (a) (i) & (ii) 2D potential and effective electric field simulated as in Section 7.4.2. (iii) Rashba parameter taken as directly proportional to (ii) (orange solid line) and reconstructed from the energy mean (iv) and splitting (v) using Equation (5.18) (green dashed line). (vi) Ratio between initial Rashba parameter $\alpha_{R,sim}$ (orange solid line in (iii)) and reconstructed Rashba parameter $\alpha_{R,rec}$ (green dashed line in (iii)). (b) Auto-correlation of the V_{eff}, $\alpha_{R,rec}$, $(\varepsilon_{0,-}+\varepsilon_{1,+})/2$ and $\varepsilon_{0,-}-\varepsilon_{1,+}$ as shown in (a), but 100 cycles of simulations are used for the correlation functions.

as a consequence of the electric field, therefore exhibits the shorter length scale fluctuations. The electrostatic potential on the other hand, only roughly approximates the local change of the electric field and, thus, of the spin-orbit coupling.

7.4.5. Determination accuracy of $\Delta E_{SS}(R)$ and $\alpha_R(R)$

This section discusses the systematic and statistical error on the evaluation, in order to estimate the reliability of determination of the $\alpha_R(R)$ maps. The statistical errors on the determination of the local spin splitting ($\sigma_{\Delta E_{SS}}$) and the local potential ($\sigma_{V_{2D}}$) result directly from the peak fitting of the double Lorentzians and are both 0.5 meV (65 % percentile) (Figure 7.19(a)). In order to evaluate

$\alpha_R(\boldsymbol{R})$, the potential map and the spin splitting map are Gaussian filtered (3×3 pixel, width 10 nm). This reduces the error of $\alpha_R(\boldsymbol{R})$ to $\sigma_{\alpha_R} = 0.02\,\text{eVÅ}$ (65 % percentile). The corresponding distribution is shown in Figure 7.19(b).

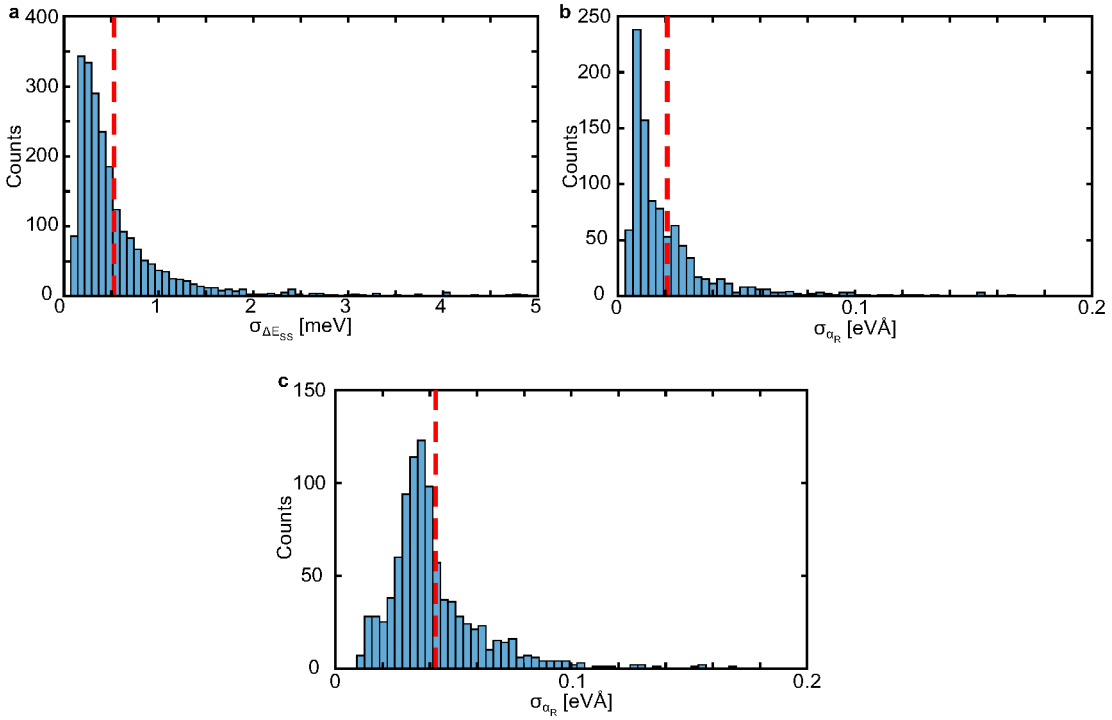

Figure 7.19.: Error histograms of $\Delta E_{SS}(\boldsymbol{R})$, relative $\alpha_R(\boldsymbol{R})$ and absolute $\alpha_R(\boldsymbol{R})$ – (a) Error histogram of the spin splitting determination by the fits shown in Figure 7.3(a) leading to the spin splitting map (Figure 7.12(a)). 65 % of the errors are smaller than $\sigma_{\Delta E_{SS}} = 0.5\,\text{meV}$ (dashed red line). (b) Error histogram of the resulting local Rashba parameters. 65 % of the errors are smaller than $\sigma_{\alpha_R} = 0.02\,\text{eVÅ}$. The error on the determination of m^* (5 %) is not included, since this error results in an uncertainty of $\overline{\alpha_R}$, but not in uncertainties of the relative α_R–values at different positions, since the same relation between V_{2D} and m^* is used for the whole image. (c). Error on the absolute value of α_R with included error on the absolute value of m^*. The 65 % percentile is $\sigma_{\alpha_R} = 0.04\,\text{eVÅ}$.

Due to the non-parabolicity of the dispersion relation, we have to make assumptions for m^*, which influence the accuracy of the determination of the absolute value of $\alpha_R(\boldsymbol{R})$. In first order, m^* is linear in the energy distance between conduction and valence band (cf. Section 7.2.3). Thus, we assume that m^* is linear in the measured energy E of a particular peak (Equation (7.4)). This is a simplification, since the evaluated energies with respect to the conduction band minimum are partly larger than the band gap [98]. The used $m^*(E)$ linear-

ity is fixed by the two m^* values resulting from Figure 7.11(a). Here, we use $\Delta E_{\mathrm{LL}} = \hbar eB/m^*$ neglecting the contribution η (Equation (7.7) of the Rashba effect ($\alpha_{\mathrm{R}} = 1\,\mathrm{eV\AA}$), which results in an m^* error of 5 %. This error is a factor of two larger than the m^* error resulting from the fitting accuracy of the LL splitting. However, with the inaccuracy of the linear model in mind, we refrain from a recursive more accurate determination of m^*. As described in Section 7.2.3, the local Landé-factor $g^*(E)$ is determined according to Equation (7.4). Neglecting the non-parabolicities completely barely changes the spatially averaged $\overline{\alpha_{\mathrm{R}}}$ (1 % increase), but leads to a reduction of the FWHM of the distribution of $\alpha_{\mathrm{R}}(\boldsymbol{R})$ by 14 %, and a local change of $\alpha_{\mathrm{R}}(\boldsymbol{R})$ by up to 20 %.
Figure 7.19(c) shows the distribution of errors on the absolute value of $\alpha_{\mathrm{R}}(\boldsymbol{R})$, taking the uncertainty of $m^*(V_{\mathrm{2D}})$ and $g^*(V_{\mathrm{2D}})$ into account. Thus, the error on the absolute value of $\alpha_{\mathrm{R}}(\boldsymbol{R})$ is estimated to be on average $\sigma_{\alpha_{\mathrm{R}}} = 0.02\,\mathrm{eV\AA}$ (4 %), while the relative error at different spatial positions is only ~2 %.
An additional systematic error results from the description of the spin splitting $\varepsilon_{0,-} - \varepsilon_{1,+}$ by Equation (5.18), which is derived by gradient expansion of the disorder potential and only takes linear terms into account [102]. Naturally, neglecting higher-order terms, which are related to the curvature of the potential, leads to an additional error. While the peak position by the potential curvature exhibits a non-negligible shift, those contributions are largely cancelled out in the spin splitting and thus, in the determination of $\alpha_{\mathrm{R}}(\boldsymbol{R})$. Nevertheless, it remains the largest error in the $\alpha_{\mathrm{R}}(\boldsymbol{R})$ determination. Calculations by Jascha Ulrich of the higher order terms for the derived 2D potential Figure 7.3(b) show that the average error turns out to be 5 %, but rises for single values up to ~30 % in regions of large curvature [17].
Finally, let us discuss the influence of the $V_{\mathrm{2D,n}}$ terms within Equation (5.18) on the determination of $\alpha_{\mathrm{R}}(\boldsymbol{R})$. Neglecting these terms, for instance, result in $\alpha_{\mathrm{R}}(\boldsymbol{R})$ values $\alpha_{\mathrm{R}}(\boldsymbol{R}) = 1.04\,\mathrm{eV\AA}$ (black) and $0.37\,\mathrm{eV\AA}$ (red) for the curves shown in Figure 7.11(b). This is a reduction by $10 - 20$ %. Thus, taking the potential map into account for the determination of $\alpha_{\mathrm{R}}(\boldsymbol{R})$ increases the accuracy significantly regarding the other intrinsic errors.

7.5. Nodal structure

This section covers the real-space observation of nodal structure corresponding to the fundamental LL wave functions as published in [155]. For high magnetic fields, a complicated peak structure is partly observed for higher LLs (Figure 7.8). For LL_1 the peak structure switches between two and four peaks, depending on the lateral position. At first, for $B = 14\,\mathrm{T}$ two peaks related to the two spin directions are to be expected. Figure 7.20 shows an LDOS measure-

ment where LL_0, LL_1 and LL_2 are spin split and can clearly be identified. Peaks at $V > 50\,\text{meV}$ are not assignable to higher LLs, since LLs of the first subband are overlapping with the LLs of the second subband. The LL splitting between LL_1 and LL_2 is slightly smaller than between LL_0, LL_1 due to the larger effective mass. Additionally, a substructure is present for LL_1 and LL_2 but not for LL_0. This apparent lifting of the degeneracy of the two spin polarised LLs in the LDOS is a fingerprint of the nodal structure of the LL wave functions (cf. Equation (5.21)). Each peak corresponds to one antinode of the fundamental wave function. Without potential disorder the LL wave functions are highly degenerate and cannot be probed separately by STS [156], but the potential disorder allows us to probe the nodal structure in real space.

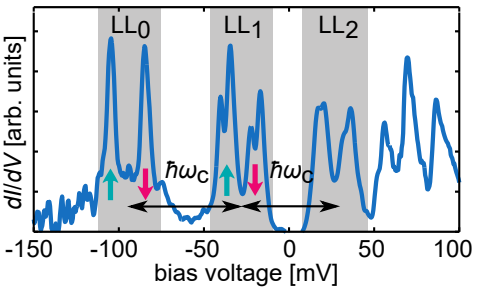

Figure 7.20.: LL and spin assignment in $\mathrm{d}I/\mathrm{d}V$ spectra – Single $\mathrm{d}I/\mathrm{d}V$ curve recorded within a potential valley area. Assignment to LL_n, $\hbar\omega_c$ and opposite spin levels are highlighted. Differences between the two $\hbar\omega_c$ relate to the non-parabolicity of the InSb conduction band (cf. Section 7.2.2). LL_1 and, to a weaker extent, LL_2 exhibit double peak structures. ($B = 14\,\text{T}$, $V_{\text{stab}} = 50\,\text{mV}$, $I_{\text{stab}} = 150\,\text{pA}$, $V_{\text{mod}} = 0.75\,\text{mV}$).

7.5.1. Mapping of the LL wave function

Concentrating on $\mathrm{d}I/\mathrm{d}V$ maps around a potential valley (Figure 7.21(a) & (b)) reveals the nodal structure in real-space. The potential landscape has firstly been determined by the position of LL_0, according to Section 7.2.1. The LDOS at the centre of the valley (Figure 7.21(c)) shows four peaks, corresponding to the spin-polarised LL_0 and LL_1, not exhibiting any substructure. Due to the potential disorder the LLs in the valley lie below the mean LLs $\overline{E}_{\text{LL},n,\uparrow}$, averaged across the sample. Figures 7.21(d)-(k) present $\mathrm{d}I/\mathrm{d}V$ images at energies around LL_0 and LL_1. All energy slides are obtained below $\overline{E}_{\text{LL},n,\uparrow}$, such that wave functions are confined by the potential valley. The $\mathrm{d}I/\mathrm{d}V$ images shown in Figures 7.21(d)-(g) show a development of a Gaussian-like distribution into a ring structure increasing in diameter with increasing voltage. The FWHM of the ring is about 8 nm, i.e. close to l_B, matching the expectation for drift

states of LL_0. These drift states map the equipotential lines at a resolution of l_B [157, 21, 22, 138, 139]. For the dI/dV images corresponding to LL_1 (Figures 7.21(h)-(k)) a development starting with a small ring structure into a double ring structure growing in size with increasing voltage is observable. The average distance between the inner and the outer ring in Figure 7.21(k) amounts to $11.6\,\text{nm} \pm 0.3\,\text{nm}$. This is close to the distance of parallel stripes of the LL wave function $\Delta_{LL_1} = 1.8 \cdot l_B = 12.2\,\text{nm}$ [156]. The fact that for LL_1 the ring development starts with an open ring and not with a Gaussian-like distribution is also in agreement with the drift states of LL_1. This is reasonable, since a Gaussian for LL_1 could not be orthogonal to the observed Gaussian of LL_0 (Figure 7.21(d)).
Recursive Green's function algorithm calculations of the LDOS conducted by Jascha Ulrich [155, 158, 159, 160] (Figure 7.21(c) right and Figures 7.21(l)-(s)) reproduced the experimental results. The calculations use a constant $m^* = 0.0275 m_e$ and $g^* = -21$ and a Rashba spin-orbit coupling of $\alpha_R = 0.5\,\text{eVÅ}$, according to the experimental results presented in Section 7.4. The experimental potential valley is used for the calculations. While the symmetries in the experiment and in the calculation correspond, the structures in the simulation grow faster in size with increasing energy and appear larger. This could be explained by the fact that the probing of the potential landscape is limited to l_B. The real potential can be steeper, leading to more compressed wave functions than considered in the calculation. Additionally, the calculations do not consider the increase of $m^*(E)$ with increasing energy. The ratio of confinement energy $\hbar\omega_0$ and LL energy $\hbar\omega_c$ increases with the effective mass [155]:

$$\frac{\omega_0}{\omega_c} \propto \sqrt{m^*}. \tag{7.10}$$

Thus, a varying effective mass would compress the wave function further.
To show that the generic nodal structures of LL wave functions are mapped, different calculations are compared in Figure 7.22. The first line originates from the calculations shown in Figures 7.21(l)-(s). In the second line, analytic calculations of the LDOS$(\boldsymbol{r})$, using Equation (5.24) with Rashba spin-orbit coupling are plotted. The third line is the same as the second, but without Rashba spin-orbit coupling. The generic features are identical for all three calculations. LL_0 shows a growing ring with increasing energy and LL_1 a double strip/ring structure. Setting $\alpha_R = 0$ does not change the basic structure, showing that the generic LL wave functions are observed. For $\alpha_R = 1\,\text{eVÅ}$, the structures appear blurrier than without spin-orbit coupling due to the mixture of LL by the spin-orbit coupling (cf. Section 5.2). In the numerics, the ring and double ring structure are slightly more pronounced. Here, an additional mixing of the wave function is allowed, resulting in a renormalisation of the effective magnetic length by ω_0 towards lower values for LL_1.

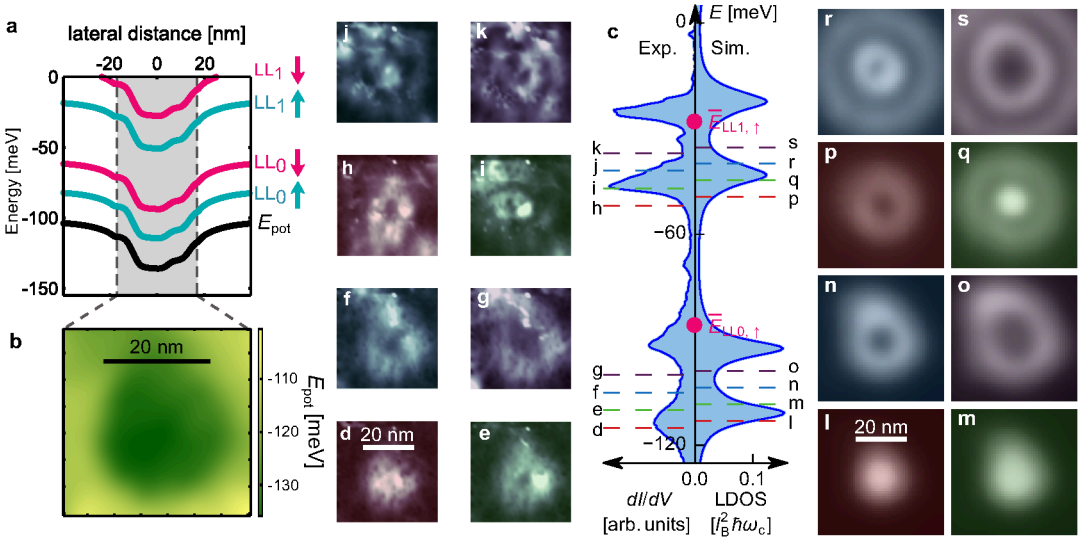

Figure 7.21.: Spatially resolved LL wave functions at a potential valley – (a) Cross section through the potential minimum of (b) (black) with additional shifted energy cuts by the kinetic LL energy and the Zeeman energy as indicated by LL_n and spin arrows. (b) 2D representation of potential minimum probed by the average LL_0 (Section 7.2.1) and subsequently shifted down by $\hbar\omega_c/2$. (c) left: dI/dV spectrum recorded in the minimum of the potential valley in (b). ($B = 14\,\mathrm{T}$, $V_{\mathrm{stab}} = 50\,\mathrm{mV}$, $I_{\mathrm{stab}} = 150\,\mathrm{pA}$, $V_{\mathrm{mod}} = 0.75\,\mathrm{mV}$). Dashed lines highlight the energies used for the LDOS images in (d)-(k). (c) right: calculated LDOS(E) in the potential minimum of (a) by the recursive Green's function approach performed by Jascha Ulrich, using $m^* = 0.0275 m_e$, $g^* = -21$ and $\alpha_R = 0.5\,\mathrm{eVÅ}$. The LDOS is broadened by a Lorentzian width of $0.05\hbar\omega_c$ in order to mimic the smallest peak width found within the experiment. Dashed lines highlight the energies used for the LDOS images in (l)-(s). Pink dots labeled $E_{\mathrm{LL}n,\uparrow}$ mark the corresponding LL energy obtained by spatially averaging the LDOS peak energy over a larger sample area. (d)-(k) dI/dV images recorded at the voltages marked in (c). LDOS images caclulated by the recursive Green's function approach at the energies marked in (c). Image sizes of (b), (d)-(k) are identical. Constant scale in (d)-(k) as well as (l)-(s) is identical.

7.5.2. Multiple probing of one LL at a fixed position

The structural differences of the LDOS($\boldsymbol{r}$) between LL_0 (ring) and LL_1 (double ring) lead to the appearance of double peaks in the spin-polarised LL_1 and single peaks in the spin-polarised LL_0 in the dI/dV curves shown in Figure 7.8 & Figure 7.20. The underlying effect is illustrated in Figure 7.23(a), which shows the idealised wave functions $|\Psi|^2$ of LL_0 & LL_1 within the potential disorder. LL_0 exhibits no node along the drift path and LL_1 a single node. Shifting these structures laterally within the potential disorder $E_{\mathrm{pot}}(x, y)$ changes their energy

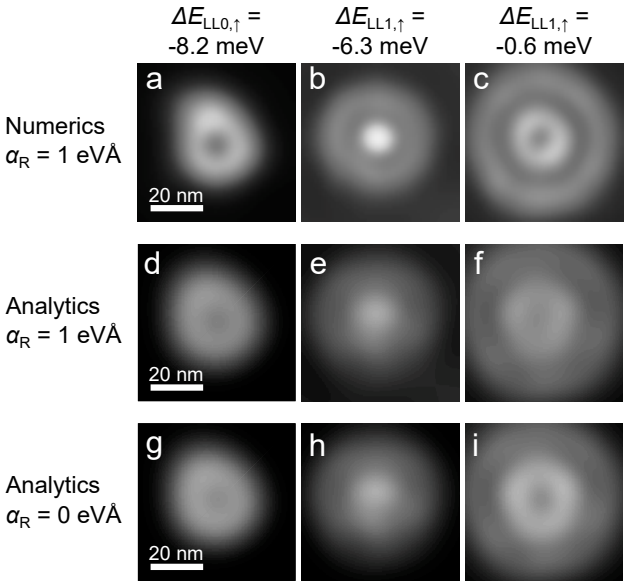

Figure 7.22.: Generality of observed nodal structures – (a)-(c) LDOS images at the energies marked on top as calculated by the recursive Green's function approach. ($m^* = 0.0275 m_e$, $g^* = -21$ and $\alpha_R = 0.5\,\mathrm{eVÅ}$) (d)-(f) LDOS images calculated using Equation (5.24). ($m^* = 0.0275 m_e$, $g^* = -21$ and $\alpha_R = 0.5\,\mathrm{eVÅ}$). (g)-(i) same as (d)-(f) but without spin-orbit coupling ($\alpha_R = 0$).

approximately according to $\langle \Psi | E_{\mathrm{pot}} | \Psi \rangle$, i.e. smoothly along the potential valley. For LL_0 the spin-polarised peak is broadened by the slope of the potential disorder. For LL_1 the situation is different. The tip can tunnel either in the inner or the outer antinode of the corresponding wave functions. Tunnelling into the inner antinode occurs at higher energies due to the potential disorder, resulting in two peaks in the $\mathrm{d}I/\mathrm{d}V$ measurement for LL_1 for each spin direction. In the flat potential valley centre the inner and outer antinode cannot be observed at the same position, thus only one peak per spin direction appears for LL_1 (cf. Figure 7.21(c)). Inner and outer antinode appear only at the same position at the slope inside the potential valley. Figures 7.23(b) & (c) show $\mathrm{d}I/\mathrm{d}V$ spectra obtained at the slope. Both spectra exhibit four peaks for LL_1. The LDOS images corresponding to the four peaks of spectra (c) are displayed in Figure 7.23(d)-(g) indicating the positions where the spectras (b) and (c) were obtained. The LL pattern in the LDOS($\boldsymbol{r}$) appears to be nearly identical for next-nearest neighbour peaks. The peaks exhibit nearly identical shapes and the energy separation between (d) & (f) as well as (e) & (g) is in both cases 20 meV, suggesting that it can be attributed to the same Zeeman term. Thus, the next-nearest neighbour peaks belong to the same wave function $|\Psi(x,y)|^2$ exhibiting two spin channels. The LDOS($\boldsymbol{r}$) shows, moreover, that the doublet of nearest neighbour peaks appears

because the inner or the outer ring is located below the tip (blue crosses). The peaks of the $\mathrm{d}I/\mathrm{d}V$ curve in Figure 7.23(b) at the energies of (e) & (g) belong to the inner ring of the LL wave function, while the outer ring is crossing this position at lower energies, resulting in its absence in Figures 7.23(d) & (f) at the position of (b).

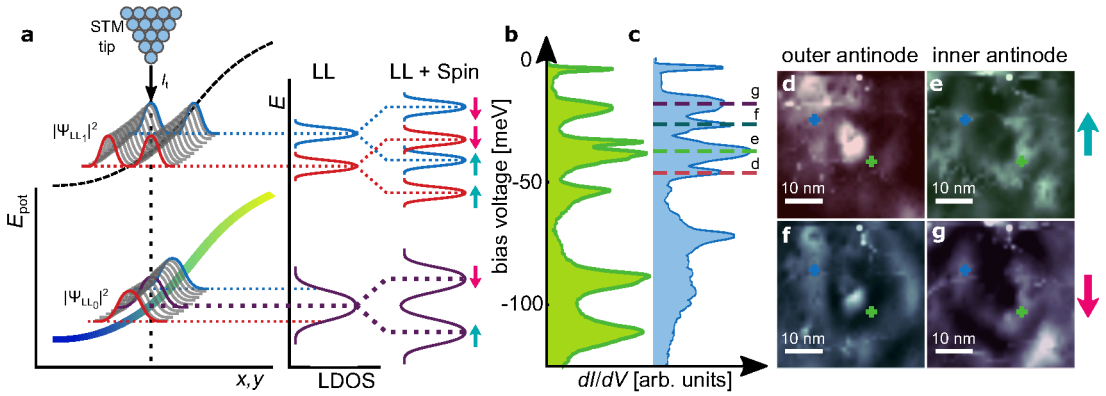

Figure 7.23.: Multi-peak structure in higher LLs – (a) Sketch of the squared wave functions $|\Psi_{\mathrm{LL}_n}(x,y)|^2$ of LL_0 and LL_1 (grey, blue, red, and violet full lines) as indicated within the potential disorder (blue-green-yellow full and black dashed lines energetically shifted by $\hbar\omega_c$). Resulting energies of the LL wave functions are indicated by the equally coloured, horizontal, dotted lines cutting the energy axis of the centre plot. The STM tip tunnels exclusively into the $|\Psi_{\mathrm{LL}_n}(x,y)|^2$ at the position marked by a vertical, black dashed line resulting in the spectrum sketched in the middle without spin polarisation (marked 'LL') and on the right with spin polarisation (marked 'LL + Spin'). Additional Zeeman splitting leads to doubling of the spectral features as sketched in the right plot. (b), (c) $\mathrm{d}I/\mathrm{d}V$ spectra recorded at the positions marked by the equally coloured crosses in (d)-(g). Dashed lines mark the voltages of the $\mathrm{d}I/\mathrm{d}V$ images in (d)-(g). ($B = 14\,\mathrm{T}$, $V_{\mathrm{stab}} = 50\,\mathrm{mV}$, $I_{\mathrm{stab}} = 150\,\mathrm{pA}$, $V_{\mathrm{mod}} = 0.75\,\mathrm{mV}$). (d)-(g) $\mathrm{d}I/\mathrm{d}V$ images at the voltages marked in (c) with crosses indicating the positions where the $\mathrm{d}I/\mathrm{d}V$ curves in (b) & (c) are recorded.

8. Summary

The first part of this thesis described the design and the characterisation of a newly home-built LT-UHV-STM system with $B = 14\,\mathrm{T}$ perpendicular to the sample surface. The cryostat is fully operational under UHV conditions and, due to the absence of mechanical pumps, it represents the most stable STM system of its kind. The system exhibits a mechanical z-stability of $\delta_z = 0.7\,\mathrm{pm}$ at a bandwidth of 700 Hz, while comparable systems report displacements of $\delta_z \approx 2\,\mathrm{pm}$ at similar bandwidths. As a result of this stability, stabilisation currents down to $I = 0.5\,\mathrm{pA}$ can be realised with atomic resolution on InAs(110). The long-term stability of $v_{d_{xy,\mathrm{long}}} = 0.09\,\text{Å/h}$ and $v_{d_{z,\mathrm{long}}} = 0.05\,\text{Å/h}$ allows a fixed positioning of several hours to days on the atomic scale. Enabled by a maximal operation time $t_{\mathrm{hold}} = 10.5\,\mathrm{days}$ at $T = 400\,\mathrm{mK}$ and virtually infinite time at $T = 9\,\mathrm{K}$, it is possible to conduct high-resolution spectroscopy mapping with atomic resolution. The operation temperature reaches down $T = 390\,\mathrm{mK}$, with an electron temperature $T_{\mathrm{el}} = 430\,\mathrm{mK}$ at the xy-stage and 520 mK at the scanner stage, determined by STS on superconductors and observation of SdH-oscillations in transport measurements. Investigation of the Josephson peak in an SS-junction was used to determine an upper boundary of the bias noise in the junction resulting in $\Delta V_{\mathrm{bias}} = 16\,\mu\mathrm{V}$ at a bandwidth of 700 Hz. Beneficial for future experiments, the spacious optical access to the microscope head inside the cryostat allows to keep the STM at $T = 25\,\mathrm{K}$ while transferring tips and samples, evaporating directly into the microscope, or positioning the tip with µm-accuracy. As it is supported with a preparation and an analysis chamber as well as a load lock, investigations of a large variety of samples are possible.

In the second part of this work, experiments on the spatial variations of the Rashba spin-orbit coupling were presented. With STM, it was possible to map the Rashba parameter down to the nm scale, limited in resolution by the magnetic length $l_B \approx 10\,\mathrm{nm}$. In the surface 2DES of Cs/p-InSb a giant Rashba parameter of $\overline{\alpha_{\mathrm{R}}}(\boldsymbol{R}) = 1.2\,\mathrm{eV\text{Å}}$, with a root mean square variation of $\delta\overline{\alpha_{\mathrm{R}}}(\boldsymbol{R}) = 0.15\,\mathrm{eV\text{Å}}$ and total variations up to a factor of four have been found. A simple analytic model allowed us to connect those variations in the spin-orbit coupling to local changes in electric field, which could be correlated using the

experimentally found correlation between Rashba parameter and local potential. With this novel technique to locally probe the Rashba parameter, the spin dephasing length resulting from those variations can be straightforwardly determined to be $l_{\mathrm{Spin}} \approx 250\,\mathrm{nm}$. Most importantly, the observed fluctuations of the Rashba parameter most likely rule the spin dephasing in the most advanced spin transistor devices [10, 11, 8]. This suggests that in order to progress in developing more feasible spintronic devices, it is necessary to understand the local variations of the Rashba spin-orbit coupling.
Furthermore, on this sample system it was possible to map the nodal structure of the zeroth and first LL wave function pinned to a potential valley. In addition to the previously observed drift states of LL_0, the development of double ring structure corresponding to the single antinode of LL_1 was resolved and could be used to explain the multiple peak structure in LDOS measurements.

Bibliography

[1] I. Žutić, J. Fabian, and S. Das Sarma. "Spintronics: Fundamentals and applications". *Rev. Mod. Phys.* 76.2 (2004), pp. 323–410.

[2] E. I. Rashba. "Spintronics: Sources and Challenge. Personal Perspective". *JSup.* 15.1 (2002), pp. 13–17.

[3] S. Datta and B. Das. "Electronic analog of the electro-optic modulator". *Appl. Phys. Lett.* 56.7 (1990), pp. 665–667.

[4] J. Schliemann, J. C. Egues, and D. Loss. "Nonballistic Spin-Field-Effect Transistor". *Phys. Rev. Lett.* 90.14 (2003), p. 146801.

[5] T. Koga et al. "Rashba spin-orbit coupling probed by the weak antilocalization analysis in InAlAs/InGaAs/InAlAs quantum wells as a function of quantum well asymmetry." *Phys. Rev. Lett.* 89.4 (2002), p. 046801.

[6] J. Wunderlich et al. "Spin Hall effect transistor." *Science* 330.6012 (2010), pp. 1801–4.

[7] S. Nadj-Perge et al. "Observation of Majorana fermions in ferromagnetic atomic chains on a superconductor". *Science* 346.6209 (2014), pp. 602–607.

[8] S. Faniel et al. "Determination of spin-orbit coefficients in semiconductor quantum wells". *Phys. Rev. B* 83.11 (2011), p. 115309.

[9] V. Mourik et al. "Signatures of Majorana Fermions in Hybrid Superconductor-Semiconductor Nanowire Devices". *Science* 336 (2012), p. 1003.

[10] W. Y. Choi et al. "Electrical detection of coherent spin precession using the ballistic intrinsic spin Hall effect". *Nat. Nanotech.* 10.8 (2015), pp. 666–670.

[11] P. Chuang et al. "All-electric all-semiconductor spin field-effect transistors". *Nat. Nanotech.* 10.1 (2015), 35–39.

[12] Junsaku Nitta. "Spin-orbit coupling: Ready for a close-up". *Nat. Phys.* advance online publication (2016). News and Views.

[13] A. Manchon et al. "New perspectives for Rashba spin-orbit coupling". *Nat. Mater.* 14.9 (2015), pp. 871–882.

[14] M. I. D'yakonov and V. I. Perel'. "Spin Relaxation of conduction electrons in noncentrosymmetric semiconductors". *SvPSS, USSR* 13.12 (1972), 3023–3026.

[15] R. J. Elliott. "Theory of the Effect of Spin-Orbit Coupling on Magnetic Resonance in Some Semiconductors". *Phys. Rev.* 96.2 (1954), pp. 266–279.

[16] M. M. Glazov, E. Y. Sherman, and V. K. Dugaev. "Two-dimensional electron gas with spinorbit coupling disorder". *Physica E: Low Dimens. Syst. Nanostruct.* 42.9 (2010), pp. 2157–2177.

[17] J. R. Bindel et al. "Probing variations of the Rashba spin–orbit coupling at the nanometre scale". *Nat. Phys.* 12 (2016), pp. 920–925.

[18] M. F. Crommie, C. P. Lutz, and D. M. Eigler. "Confinement of Electrons to Quantum Corrals on a Metal Surface". *Science* 262.5131 (1993), pp. 218–220.

[19] M. C. M. M. van der Wielen, A. J. A. van Roij, and H. van Kempen. "Direct Observation of Friedel Oscillations around Incorporated Si_{Ga} Dopants in GaAs by Low-Temperature Scanning Tunneling Microscopy". *Phys. Rev. Lett.* 76.7 (1996), pp. 1075–1078.

[20] G. M. Rutter et al. "Scattering and interference in epitaxial graphene." *Science* 317.5835 (2007), pp. 219–222.

[21] K. Hashimoto et al. "Quantum hall transition in real space: From localized to extended states". *Phys. Rev. Lett.* 101.25 (2008), pp. 18–21.

[22] D. L. Miller et al. "Real-space mapping of magnetically quantized graphene states". *Nat. Phys.* 6.10 (2010), 811–817.

[23] E. Wigner. "On the Interaction of Electrons in Metals". *Phys. Rev.* 46.11 (1934), pp. 1002–1011.

[24] G. Binnig et al. "Surface studies by scanning tunneling microscopy". *Phys. Rev. Lett.* 49.1 (1982), pp. 57–61.

[25] G. Binnig and C. F. Quate. "Atomic Force Microscope". *Phys. Rev. Lett.* 56.9 (1986), pp. 930–933.

[26] Roland Wiesendanger. *Scanning probe microscopy and spectroscopy - Methods and applications*. Cambridge University Press, 1998.

[27] André Wachowiak. "Aufbau einer 300mK-Ultrahochvakuum-Rastertunnelmikroskopie-Anlage mit 14 Tesla Magnet und spinpolarisierte Rastertunnelmikroskopie an ferromagnetischen Fe-Inseln". PhD thesis. Universität Hamburg, 2003.

[28] R. J. Hamers. "Atomic-Resolution Surface Spectroscopy with the Scanning Tunneling Microscope". *Annu. Rev. Phys. Chem.* 40.1 (1989), pp. 531–559.

[29] J. Bardeen. "Tunnelling from a many-particle point of view". *Phys. Rev. Lett.* 6.2 (1961), pp. 57–59.

[30] J. Tersoff and D. R. Hamann. "Theory and application for the scanning tunneling microscope". *Phys. Rev. Lett.* 50.25 (1983), pp. 1998–2001.

[31] J. Tersoff and D. R. Hamann. "Theory of the scanning tunneling microscope". *Phys. Rev. B* 31.2 (1985), pp. 805–813.

[32] C. J. Chen. "Theory of scanning tunneling spectroscopy". *J. Vac. Sci. Technol. A* 6.2 (1988), pp. 319–322.

[33] C. J. Chen. "Tunneling matrix elements in three-dimensional space: The derivative rule and the sum rule". *Phys. Rev. B* 42.14 (1990), pp. 8841–8857.

[34] C. J. Chen. "Origin of atomic resolution on metal surfaces in scanning tunneling microscopy". *Phys. Rev. Lett.* 65.4 (1990), pp. 448–451.

[35] M. Morgenstern. "Probing the local density of states of dilute electron systems in different dimensions". *Surf. Rev. Lett.* 10.06 (2003), pp. 933–962.

[36] J. Wiebe et al. "A 300 mK ultra-high vacuum scanning tunneling microscope for spin-resolved spectroscopy at high energy resolution". *Rev. Sci. Instrum.* 75.11 (2004), pp. 4871–4879.

[37] M. Assig et al. "A 10 mK scanning tunneling microscope operating in ultra high vacuum and high magnetic fields". *Rev. Sci. Instrum.* 84.3, 033903 (2013).

[38] I. Giaever. "Energy Gap in Superconductors Measured by Electron Tunneling". *Phys. Rev. Lett.* 5.4 (1960), pp. 147–148.

[39] I. Giaever and K. Megerle. "Study of Superconductors by Electron Tunneling". *Phys. Rev.* 122.4 (1961), pp. 1101–1111.

[40] S. H. Pan, E. W. Hudson, and J. C. Davis. "Vacuum tunneling of superconducting quasiparticles from atomically sharp scanning tunneling microscope tips". *Appl. Phys. Lett.* 73.20 (1998), pp. 2992–2994.

[41] S. Guéron et al. "Superconducting Proximity Effect Probed on a Mesoscopic Length Scale". *Phys. Rev. Lett.* 77.14 (1996), pp. 3025–3028.

[42] E. N. Bratus, V. S. Shumeiko, and G. Wendin. "Theory of Subharmonic Gap Structure in Superconducting Mesoscopic Tunnel Contacts". *Phys. Rev. Lett.* 74.11 (1995), pp. 2110–2113.

[43] J. C. Cuevas, A. Martin-Rodero, and A. Levy Yeyati. "Hamiltonian approach to the transport properties of superconducting quantum point contacts". *Phys. Rev. B* 54.10 (1996), pp. 7366–7379.

[44] B. D. Josephson. "Possible new effects in superconductive tunnelling". *Phys. Lett.* 1.7 (1962), pp. 251–253.

[45] J. C. Cuevas and W. Belzig. "Full Counting Statistics of Multiple Andreev Reflections". *Phys. Rev. Lett.* 91.18 (2003), p. 187001.

[46] M. Ternes et al. "Subgap structure in asymmetric superconducting tunnel junctions". *Phys. Rev. B* 74.13 (2006), p. 132501.

[47] Y. M. Ivanchenko and L. A. Zilberman. "The Josephson effect in small tunnel contacts." *Sov. Phys. JETP* 28(6) (1969), pp. 1272–1276.

[48] O. Naaman, W. Teizer, and R. C. Dynes. "Fluctuation Dominated Josephson Tunneling with a Scanning Tunneling Microscope". *Phys. Rev. Lett.* 87.9 (2001), p. 097004.

[49] B. Jäck et al. "A nanoscale gigahertz source realized with Josephson scanning tunneling microscopy". *Appl. Phys. Lett.* 106.1, 013109 (2015).

[50] Berthold Jäck. "Josephson tunneling at the atomic scale: The Josephson effect as local probe". PhD thesis. École Polytechnique Fédérale de Lausanne, 2015.

[51] P. Joyez et al. "The Josephson Effect in Nanoscale Tunnel Junctions". *JSup.* 12.6 (1999), pp. 757–766.

[52] H. Kambara et al. "Construction of a versatile ultralow temperature scanning tunneling microscope". *Rev. Sci. Instrum.* 78.7 (2007), pp. 1–5.

[53] Young Jae Song et al. "Invited Review Article: A 10 mK scanning probe microscopy facility". *Rev. Sci. Instrum.* 81.12, 121101 (2010).

[54] H. Suderow, I. Guillamon, and S. Vieira. "Compact very low temperature scanning tunneling microscope with mechanically driven horizontal linear positioning stage". *Rev. Sci. Instrum.* 82.3, 033711 (2011).

[55] S. Misra et al. "Design and performance of an ultra-high vacuum scanning tunneling microscope operating at dilution refrigerator temperatures and high magnetic fields". *Rev. Sci. Instrum.* 84.10, 103903 (2013).

[56] U. R. Singh et al. "Construction and performance of a dilution-refrigerator based spectroscopic-imaging scanning tunneling microscope". *Rev. Sci. Instrum.* 84.1, 013708 (2013).

[57] A. Roychowdhury et al. "A 30 mK, 13.5 T scanning tunneling microscope with two independent tips". *Rev. Sci. Instrum.* 85.4, 043706 (2014).

[58] J. A. Galvis et al. "Three axis vector magnet set-up for cryogenic scanning probe microscopy". *Rev. Sci. Instrum.* 86.1, 013706 (2015).

[59] M. Pelliccione et al. "Design of a scanning gate microscope for mesoscopic electron systems in a cryogen-free dilution refrigerator". *Rev. Sci. Instrum.* 84.3, 033703 (2013).

[60] A. M. J. den Haan et al. "Atomic resolution scanning tunneling microscopy in a cryogen free dilution refrigerator at 15 mK". *Rev. Sci. Instrum.* 85.3, 035112 (2014).

[61] L. Zhang et al. "A compact sub-Kelvin ultrahigh vacuum scanning tunneling microscope with high energy resolution and high stability". *Rev. Sci. Instrum.* 82.10, 103702 (2011).

[62] J. Jandke et al. "Scanning tunneling spectroscopy on $SrFe_2(As_{1-x}P_x)_2$". *Phys. Rev. B* 93.10 (2016), p. 104528.

[63] S. H. Pan, E. W. Hudson, and J. C. Davis. "3He refrigerator based very low temperature scanning tunneling microscope". *Rev. Sci. Instrum.* 70.2 (1999), pp. 1459–1463.

[64] M. Kugler et al. "A 3He refrigerated scanning tunneling microscope in high magnetic fields and ultrahigh vacuum". *Rev. Sci. Instrum.* 71.3 (2000), pp. 1475–1478.

[65] A. Kamlapure et al. "A 350 mK, 9 T scanning tunneling microscope for the study of superconducting thin films on insulating substrates and single crystals". *Rev. Sci. Instrum.* 84.12, 123905 (2013).

[66] H. von Allwörden et al. "Set-up of a high-resolution 300 mK atomic force microscope in an ultra-high vacuum compatible 3He/10 T cryostat". *Rev. Sci. Instrum.* 87.7, 073702 (2016).

[67] Stefan Becker. "Design of a 300 mK-14 T scanning tunneling microscopy system and characterization of quantum Hall systems with respect to Rashba spin splitting, exchange enhancement and Coulomb gap". PhD thesis. RWTH Aachen - II. Institute of Physics B, 2011.

[68] M. C. Steele and R. A. Hein. "Superconductivity of Titanium". *Phys. Rev.* 92.2 (1953), pp. 243–247.

[69] A. Peruzzi et al. "Investigation of the titanium superconducting transition as a temperature reference point below 0.65 K". *Metrologia* 37.3 (2000), p. 229.

[70] R. L. Rusby and C. A. Swenson. "A new determination of the Helium vapor-pressure scales using a CMN magnetic thermometer and the NPL-75 gas thermometer scale". *Metrologia* 16.2 (1980), 73–87.

[71] Jan Raphael Bindel. "Aufbau eines kombinierten Rasterkraft-/Rastertunnelmikroskops für Messungen unter Transportbedingungen". Diplomarbeit. RWTH Aachen - II. Institute of Physics B, 2009.

[72] Alexander Georgi. "Investigation of strain physics in graphene by scanning tunneling microscopy". PhD thesis. RWTH Aachen - II. Institute of Physics B, 2016.

[73] Florian Muckel. "Optimierung eines kombinierten Rastertunnel- und Rasterkraftmikroskops". Diplomarbeit. RWTH Aachen - II. Institute of Physics B, 2013.

[74] F. J. Giessibl. "High-speed force sensor for force microscopy and profilometry utilizing a quartz tuning fork". *Appl. Phys. Lett.* 73.26 (1998), pp. 3956–3958.

[75] F. J. Giessibl et al. "Comparison of force sensors for atomic force microscopy based on quartz tuning forks and length-extensional resonators". *Phys. Rev. B* 84.12 (2011), p. 125409.

[76] B. J. Albers et al. "Combined low-temperature scanning tunneling/atomic force microscope for atomic resolution imaging and site-specific force spectroscopy". *Rev. Sci. Instrum.* 79.3, 033704 (2008).

[77] E. Wutscher and F. J. Giessibl. "Atomic force microscopy at ambient and liquid conditions with stiff sensors and small amplitudes". *Rev. Sci. Instrum.* 82.9, 093703 (2011).

[78] T. Fukuma et al. "True atomic resolution in liquid by frequency-modulation atomic force microscopy". *Appl. Phys. Lett.* 87.3, 034101 (2005).

[79] A. V. Kretinin et al. "Electronic Properties of Graphene Encapsulated with Different Two-Dimensional Atomic Crystals". *Nano Lett.* 14.6 (2014), pp. 3270–3276.

[80] K. S. Novoselov et al. "Two-dimensional gas of massless Dirac fermions in graphene." *Nature* 438.7065 (2005), pp. 197–200.

[81] Y. Zhang et al. "Experimental observation of the quantum Hall effect and Berry's phase in graphene". *Nature* 438 (2005), pp. 201–204.

[82] K. I. Bolotin et al. "Observation of the fractional quantum Hall effect in graphene". *Nature* 462 (2009), pp. 196–199.

[83] Michael Tinkham. *Introduction to Superconductivity*. Dover Publications, 2004.

[84] P. Townsend and J. Sutton. "Investigation by Electron Tunneling of the Superconducting Energy Gaps in Nb, Ta, Sn, and Pb". *Phys. Rev.* 128.2 (1962), pp. 591–595.

[85] J. Matthews and M. E. Cage. "Temperature dependence of the Hall and longintudinal resistances in a quantum Hall resistance standard". *J. Res. Natl. Inst. Stand. Technol.* 110.5 (2005), 497–510.

[86] A. L. Efros and B. I. Shklovskii. "Coulomb gap and low temperature conductivity of disordered systems". *J. Phys. C: Solid State* 8.4 (1975), p. L49.

[87] B. I. Shklovskii and A. L. Efros. *Electronic Properties of Doped Semiconductors*. Springer-Verlag, Berlin, 1984.

[88] S. Qin et al. "Superconductivity at the Two-Dimensional Limit". *Science* 324.5932 (2009), pp. 1314–1317.

[89] J. Kim et al. "Universal quenching of the superconducting state of two-dimensional nanosize Pb-island structures". *Phys. Rev. B* 84.1 (2011), p. 014517.

[90] H. C. Koo et al. "Control of spin precession in a spin-injected field effect transistor." *Science* 325.5947 (2009), pp. 1515–1518.

[91] C Betthausen et al. "Spin-Transistor Action via Tunable Landau-Zener Transitions". *Science* 337.6092 (2012), pp. 324–327.

[92] J. D. Koralek et al. "Emergence of the persistent spin helix in semiconductor quantum wells". *Nature* 458.7238 (2009), 610–U73.

[93] A. Sasaki et al. "Direct determination of spin-orbit interaction coefficients and realization of the persistent spin helix symmetry". *Nat. Nanotech.* 9.9 (2014), 703–709.

[94] R. H. Parmenter. "Symmetry Properties of the Energy Bands of the Zinc Blende Structure". *Phys. Rev.* 100.2 (1955), pp. 573–579.

[95] M. S. Dresselhaus and G. Dresselhaus. "Intercalation compounds of graphite". *Adv. Phys.* 30.2 (1981), pp. 139–326.

[96] Y. A. Bychkov and E. I. Rashba. "Properties of a 2D electron gas with lifted spectral degeneracy". *JETP Lett.* 39 (1984), pp. 78–81.

[97] F. J. Ohkawa and Y. Uemura. "Quantized Surface States of a Narrow-Gap Semiconductor". *J. Phys. Soc. Jpn.* 37.5 (1974), pp. 1325–1333.

[98] Roland Winkler. *Spin-Orbit Coupling Effects in Two-Dimensional Electron and Hole System*. Springer Berlin, Heidelberg, 2003.

[99] Thomas Schäpers. "Spintronics and Emergent Qubits". *IFF Spring School 2013 - Quantum Information Processing*. Peter Grünberg Institut, Forschungszentrum Jülich GmbH. 2013.

[100] S. M. Girvin and T. Jach. "Formalism for the quantum Hall effect: Hilbert space of analytic functions". *Phys. Rev. B* 29.10 (1984), pp. 5617–5625.

[101] T. Champel and S. Florens. "Quantum transport properties of two-dimensional electron gases under high magnetic fields". *Phys. Rev. B* 75.24 (2007), p. 245326.

[102] D. Hernangómez-Pérez et al. "Spectral properties and local density of states of disordered quantum Hall systems with Rashba spin-orbit coupling". *Phys. Rev. B* 88.24 (2013), p. 245433.

[103] Daniel Hernangómez-Pérez. "Spin-Orbit Coupling and Strong Interactions in the Quantum Hall Regime". PhD thesis. Université de Grenoble - Physique de la matière condensée et du rayonnement, 2014.

[104] T. Champel and S. Florens. "Local density of states in disordered two-dimensional electron gases at high magnetic field". *Phys. Rev. B* 80.16 (2009), p. 161311.

[105] T. Champel and S. Florens. "High magnetic field theory for the local density of states in graphene with smooth arbitrary potential landscapes". *Phys. Rev. B* 82.4 (2010), p. 045421.

[106] J. R. Dixon and J. K. Furdyna. "Measurement of the static dielectric constant of the InSb lattice via gyrotropic sphere resonances". *Solid State Commun.* 35.2 (1980), 195–198.

[107] S. Becker et al. "Scanning tunneling spectroscopy of a dilute two-dimensional electron system exhibiting Rashba spin splitting". *Phys. Rev. B* 81.15 (2010), pp. 1–9.

[108] P. Boross et al. "A unified theory of spin-relaxation due to spin-orbit coupling in metals and semiconductors". *Sci. Rep.* 3 (2013).

[109] Y. Yafet. "Conduction electron spin relaxation in the superconducting state". *Phys. Lett. A* 98.5 (1983), pp. 287–290.

[110] Tsuneya Ando. "Electronic properties of two-dimensional systems". *Reviews of Modern Physics* 54.2 (1982), pp. 437–672.

[111] D. D. Awschalom and M. E. Flatté. "Challenges for semiconductor spintronics". *Nat. Phys.* 3.3 (2007), pp. 153–159.

[112] J. H. Kim et al. "All-electric spin transistor using perpendicular spins". *J. Magn. Magn. Mater.* 403 (2016), pp. 77–80.

[113] G. Engels et al. "Experimental and theoretical approach to spin splitting in modulation-doped $In_xGa_{1-x}As/InP$ quantum wells for B→0". *Phys. Rev. B* 55.4 (1997), pp. 1958–1961.

[114] J. Nitta et al. "Gate Control of Spin-Orbit Interaction in an Inverted In0.53Ga0.47As/In0.52Al0.48As Heterostructure". *Phys. Rev. Lett.* 78.7 (1997), pp. 1335–1338.

[115] H. J. Zhu et al. "Room-Temperature Spin Injection from Fe into GaAs". *Phys. Rev. Lett.* 87.1 (2001), p. 016601.

[116] C.-M. Hu et al. "Spin-polarized transport in a two-dimensional electron gas with interdigital-ferromagnetic contacts". *Phys. Rev. B* 63.12 (2001), p. 125333.

[117] H. B. Heersche et al. "Enhancement of spin injection from ferromagnetic metal into a two-dimensional electron gas using a tunnel barrier". *Phys. Rev. B* 64.16 (2001), p. 161307.

[118] M. Johnson and R. H. Silsbee. "Coupling of electronic charge and spin at a ferromagnetic-paramagnetic metal interface". *Phys. Rev. B* 37.10 (1988), pp. 5312–5325.

[119] G. Dresselhaus. "Spin-Orbit Coupling Effects in Zinc Blende Structures". *Phys. Rev.* 100.2 (1955), pp. 580–586.

[120] T. D. Stanescu and V. Galitski. "Spin relaxation in a generic two-dimensional spin-orbit coupled system". *Phys. Rev. B* 75.12 (2007), p. 125307.

[121] B. A. Bernevig, J. Orenstein, and S.-C. Zhang. "Exact SU(2) Symmetry and Persistent Spin Helix in a Spin-Orbit Coupled System". *Phys. Rev. Lett.* 97.23 (2006), p. 236601.

[122] M. P. Walser et al. "Direct mapping of the formation of a persistent spin helix". *Nat. Phys.* 8.10 (2012), 757–762.

[123] D Grundler. "Large Rashba splitting in InAs quantum wells due to electron wave function penetration into the barrier layers." *Phys. Rev. Lett.* 84.26 Pt 1 (2000), pp. 6074–6077.

[124] L. Petersen and P. Hedegaard. "A simple tight-binding model of spin-orbit splitting of sp-derived surface states". *Surface Science* 459.12 (2000), pp. 49–56.

[125] M. Steinbrecher et al. "Rashba-type spin splitting from interband scattering in quasiparticle interference maps". *Phys. Rev. B* 87.24 (2013), pp. 1–5.

[126] P. Leicht et al. "Rashba splitting of graphene-covered Au(111) revealed by quasiparticle interference mapping". *Phys. Rev. B* 90.24 (2014), p. 241406.

[127] L. El-Kareh et al. "A combined experimental and theoretical study of Rashba-split surface states on the $(\sqrt{3} \times \sqrt{3})$ Pb/Ag(111) $R30°$ surface". *New J. Phys.* 16.4 (2014), p. 045017.

[128] H. Bentmann et al. "Origin and manipulation of the Rashba splitting in surface alloys". *EPL* 87.3 (2009), p. 37003.

[129] L. Moreschini et al. "Influence of the substrate on the spin-orbit splitting in surface alloys on (111) noble-metal surfaces". *Phys. Rev. B* 80.3 (2009), p. 035438.

[130] C. R. Ast et al. "Local detection of spin-orbit splitting by scanning tunneling spectroscopy". *Phys. Rev. B* 75.20 (2007), pp. 3–6.

[131] J. Kliewer et al. "Dimensionality Effects in the Lifetime of Surface States". *Science* 288.5470 (2000), pp. 1399–1402.

[132] C. R. Moon, C. P. Lutz, and Hari C. Manoharan. "Single-atom gating of quantum-state superpositions". *Nat. Phys.* 4.6 (2008), pp. 454–458.

[133] K. Hashimoto et al. "Robust nodal structure of landau level wave functions revealed by fourier transform scanning tunneling spectroscopy". *Phys. Rev. Lett.* 109.11 (2012), pp. 1–5.

[134] R. M. Feenstra and J. A. Stroscio. "Tunneling Spectroscopy of the GaAs(110) surface". *J. Vac. Sci. Technol. B* 5.4 (1987), 923–929.

[135] R. Dombrowski et al. "Tip-induced band bending by scanning tunneling spectroscopy of the states of the tip-induced quantum dot on InAs(110)". *Phys. Rev. B* 59.12 (1999), pp. 8043–8048.

[136] M. Morgenstern et al. "Low temperature scanning tunneling spectroscopy on InAs(110)". *J. Electron. Spectrosc. Relat. Phenom.* 109.12 (2000), pp. 127–145.

[137] M. Morgenstern et al. "Direct Comparison between Potential Landscape and Local Density of States in a Disordered Two-Dimensional Electron System". *Phys. Rev. Lett.* 89.13 (2002), p. 136806.

[138] R. Joynt and R. E. Prange. "Conditions for the quantum Hall effect". *Phys. Rev. B* 29.6 (1984), pp. 3303–3317.

[139] T. Ando. "Electron Localization in a Two-Dimensional System in Strong Magnetic Fields. II. Long-Range Scatterers and Response Functions". *J. Phys. Soc. Jpn.* 53.9 (1984), pp. 3101–3111.

[140] B. Kramer, T. Ohtsuki, and S. Kettemann. "Random network models and quantum phase transitions in two dimensions". *Phys. Rep.* 417.56 (2005), pp. 211–342.

[141] F. Evers and A. D. Mirlin. "Anderson transitions". *Rev. Mod. Phys.* 80.4 (2008), pp. 1355–1417.

[142] M. G. Betti et al. "Density of states of a two-dimensional electron gas at semiconductor surfaces". *Phys. Rev. B* 63.15 (2001), p. 155315.

[143] M. Morgenstern et al. "Scanning tunneling microscopy of two-dimensional semiconductors: Spin properties and disorder". *Physica E: Low Dimens. Syst. Nanostruct.* 44.9 (2012), pp. 1795–1814.

[144] U. Merkt and S. Oelting. "Simple description of nonparabolic two-dimensional subbands". *Phys. Rev. B* 35.5 (1987), pp. 2460–2462.

[145] S. Becker et al. "Probing Electron-Electron Interaction in Quantum Hall Systems with Scanning Tunneling Spectroscopy". *Phys. Rev. Lett.* 106 (15 2011), p. 156805.

[146] L. M. Kanskaya et al. "Direct Determination of Antimonide Energy Band Parameters from Diamagnetic Exciton Spectra". *Phys. Status Solidi B* 118.1 (1983), p. 447.

[147] O. Madelung, U. Rössler, and M. Schulz. *Landolt-Börnstein - Group III Condensed Matter*. Springer Verlag, 2002.

[148] I. Vurgaftman, J. R. Meyer, and L. R. Ram-Mohan. "Band parameters for III-V compound semiconductors and their alloys". *Journal of Applied Physics* 89.11 I (2001), pp. 5815–5875.

[149] M. Pollak. "Effect of carrier-carrier interactions on some transport properties in disordered semiconductors". *Discuss. Faraday Soc.* 50 (1970), pp. 13–19.

[150] F. G. Pikus and A. L. Efros. "Coulomb gap in a two-dimensional electron gas with a close metallic electrode". *Phys. Rev. B* 51.23 (1995), pp. 16871–16877.

[151] R. Masutomi and T. Okamoto. "Adsorbate-induced quantum Hall system probed by scanning tunneling spectroscopy combined with transport measurements". *Appl. Phys. Lett.* 106.25 (2015), p. 251602.

[152] T. Ando and Y. Uemura. "Theory of oscillatory g factor in an MOS inversion layer under strong magnetic fields". *J. Phys. Soc. Jpn.* 37.4 (1974), pp. 1044–1052.

[153] L. Bürgi et al. "Probing Hot-Electron Dynamics at Surfaces with a Cold Scanning Tunneling Microscope". *Phys. Rev. Lett.* 82.22 (1999), pp. 4516–4519.

[154] T. Champel and S. Florens. "Electron quantum dynamics in closed and open potentials at high magnetic fields: Quantization and lifetime effects unified by semicoherent states". *Phys. Rev. B* 80.12 (2009), p. 125322.

[155] J. R. Bindel et al. "Probing the Nodal Structure of Landau Level Wave Functions in Real Space". *Phys. Rev. Lett.* 118.1 (2017), p. 016803.

[156] L. D. Landau and E. M. Lifschitz. *Quantum Mechanics: Non-relativistic Theory. Course of Theoretical Physics. Vol. 3 3rd ed.* Pergamon Press, London, 1977.

[157] M. Morgenstern et al. "Real-space observation of drift States in a two-dimensional electron system at high magnetic fields." *Phys. Rev. Lett.* 90.5 (2003), p. 056804.

[158] P. A. Lee and D. S. Fisher. "Anderson Localization in Two Dimensions". *Phys. Rev. Lett.* 47.12 (1981), pp. 882–885.

[159] D. J. Thouless and S. Kirkpatrick. "Conductivity of the disordered linear chain". *J. Phys. C: Solid State* 14.3 (1981), p. 235.

[160] A. MacKinnon. "The calculation of transport properties and density of states of disordered solids". *Z. Phys. B Con. Mat.* 59.4 (1985), pp. 385–390.

Publications

Publications described within this thesis

1. J. R. Bindel, M. Pezzotta, J. Ulrich, M. Liebmann, E. Ya. Sherman, and M. Morgenstern. Probing variations of the Rashba spin–orbit coupling at the nanometre scale. *Nat. Phys.* 12 (2016), pp. 920-925, doi: 10.1038/nphys3774.

2. J. R. Bindel, J. Ulrich, M. Liebmann, and M. Morgenstern. Probing the nodal structure of Landau level wave functions in real space. *Phys. Rev. Lett.* 118.1 (2017), p. 016803, doi: 10.1103/PhysRevLett.118.016803.

Further publications

1. C. Saunus, J. R. Bindel, M. Pratzer, and M. Morgenstern. Versatile scanning tunneling microscopy with 120 ps time resolution. *Appl. Phys. Lett.*, 102 051601, 2013. doi: 10.1063/1.4790180.

Presentations

1. J. R. Bindel, M. Liebmann, and M. Morgenstern. Combined scanning tunnelling / atomic force microscope for applications at 300 mK and 14 T. In *DPG Frühjahrstagung der Sektion Kondensierte Materie*, Dresden, Germany, 2009. (Poster)

2. J. R. Bindel, T. Matsui, K. Nakayama and H. Fukuyama. Towards the Band Gap Opening in Graphene. In *The 63rd Research Forum Cryogenic Research Center*, Tokyo, Japan, 2011. (Poster)

3. J. R. Bindel, T. Matsui, and H. Fukuyama. Krypton adsorbed on Graphite. In *DPG Frühjahrstagung der Sektion Kondensierte Materie*, Regensburg, Germany, 2013. (Vortrag)

4. J. R. Bindel, M. Pezzotta, S. Becker, M. Liebmann, and M. Morgenstern. Versatile and compact UHV -System for Scanning Tunneling, Scanning Force and Transport Measurements exhibiting an operation time of 10 days below T = 400mK and at B = 14T. In *DPG Frühjahrstagung der Sektion Kondensierte Materie*, Regensburg, Germany, 2014. (Poster)

5. J. R. Bindel, M. Liebmann, J. Ulrich, E. Sherman and M. Morgenstern. Spatial fluctuations of the Rashba parameter. In *DPG Frühjahrstagung der Sektion Kondensierte Materie*, Berlin, Germany, 2015. (Vortrag)

6. J. R. Bindel, M. Liebmann, E. Sherman and M. Morgenstern. Probing Variations of the Rashba Spin-Orbit Coupling at the Nanometer Scale. In *The 8th Frontier Scientists Workshop*, Stuttgart, Germany, 2016. (Vortrag)

Acknowledgments

At this point I would like to thank those people who supported me over the course of the last couple of years. First of all, I would like to thank *Prof. Dr. Markus Morgenstern*, for giving me the chance to perform my doctoral studies under his supervision at the II. Institute of Physics B, RWTH Aachen. I am very grateful for the time, help and advice he offered me during my time both as a PhD student and prior to that as a Diploma student. I experienced his demanding and yet supportive approach, and his willingness to always be available when needed. I also would like to thank him for giving me the opportunity to undertake a year of my doctoral studies at the University of Tokyo.
I would also like to express my gratitude to *Prof. Dr. Hiroshi Fukuyama* from Fukyama Laboratory, The University of Tokyo, for hosting me at his institute, and *Dr. Tomohiro Matsui* for his assistance and mentoring. I am also grateful to the DAAD for the financial support via doctoral studies fellowship.
Thanks also to *Dr. Markus Liebmann* for his advice and support, especially for his support with my work in the laboratory and the many helpful discussions. Many thanks also go to *Mike Pezzotta* for a great time and making the working life in the laboratory joyful. We designed and built the cryostat-system together and spent a countless amount of time discussing, designing, and optimising. Regarding the UHV-system, I would like to thank *Dr. Stefan Becker* for the initial design of the system, support frame, and laboratory, which was the basis for the successful realisation.
The whole project would not have been possible without the high quality and precise work of the workshop under the supervision of *Peter Kordt* and *Wolfgang Retetzki*. I would also like to thank the whole workshop team for their multitudinous work hours, with special thanks to *Frank Neubauer*, *Robert Feron*, *Frank Salz* and *Raoul Sous*.
Thanks also to the members of the electronics workshop *Guido Geulen*, *Uwe Wichmann* and *Lars van Hove* for the support, despite my often short-termed and urgent requests.
The measurements were only possible due to the commitment of the Helium and Nitrogen liquefiers *Jörg Schirra* and *Sascha Mohr*, who ensured with their supply of cryogenic liquids that the experiments could run continuously, even during the Christmas holidays.

For the theoretical calculations, simulations, discussions and contributions to the publications concerning the Rashba spin-orbit coupling I have to thank *Prof. Dr. Eugene Sherman* from Ikerbasque, Basque Foundation of Science and *Jascha Ulrich* from the Institute for Quantum Information, RWTH Aachen.
Next thanks go to my colleagues *Nils Freitag*, *Dr. Alexander Georgi*, *Christian Holl* and *Dr. Kilian Flöhr* for many fruitful discussions and teaming up with me to solve physical problems, as well as a great time beyond the laboratory.
Many thanks to the whole all other members and former members research group of the II. Institute of Physics B, *Dr. Martin Grob*, *Dr. Christian Pauly*, *Dr. Peter Nemes-Incze*, *Dr. Marco Pratzer*, *Dr. Dinesh Subramaniam*, *Dr. Torge Mashoff*, *Florian Muckel*, *Jens Kellner*, *Silke Rose*, *Daniel Montag*, *Tjorven Johnsen*, *Felix Jekat* and *Priyamvada Bhaskar*.
I am also grateful to *Prof. Dr. Thomas Schäpers* for agreeing to co-evaluate my dissertation.
I also want to acknowledge the administrative staff of the of the II. Institute B, *Beate Nagel*, *Margarete Betger* and *Beatrix Dangela* for making life easier by taking care of the bureaucracy.
Thanks also to *Daniel Piel* for giving the thesis a final check.
Finally, I would like to thank my parents *Martina Kaiser-Bindel* and *Joachim Bindel* for their abiding support throughout my whole life, as well as my two brothers *Florian Bindel* and *Fabian Bindel*, and *Helen Kenyon* who has been ineffably helpful and patiently put up with me in the sometimes very stressful time during my PhD.